Phenomenology and Constraints in Singlet Extensions of Two Higgs Doublet Models

Dissertation
zur Erlangung des Doktorgades
an der Fakultät für Mathematik, Informatik und Naturwissenschaften
im Fachbereich Physik
der Universität Hamburg

vorgelegt von

Steven Paasch

Hamburg

2023

Gutachter/innen der Dissertation:	Prof. Dr. Gudrid Moortgat-Pick Dr. Jürgen Reuter
Zusammensetzung der Prüfungskommission:	Prof. Dr. Gudrid Moortgat-Pick Dr. Jürgen Reuter Prof. Dr. Georg Weiglein Prof. Dr. Michael Potthoff Prof. Dr. Johannes Haller
Vorsitzender der Prüfungskommission	Prof. Dr. Michael Potthoff
Datum der Disputation:	30.06.2023
Vorsitzender des Fach-Promotionsausschusses PHYSIK:	Prof. Dr. Günter H. W. Sigl
Leiter des Fachbereichs PHYSIK:	Prof. Dr. Wolfgang J. Parak
Dekan der Fakultät MIN:	Prof. Dr.-Ing. Norbert Ritter

Abstract

In the first part of this thesis we introduce the Two Higgs Doublet Model (2HDM) with a complex singlet and a $\mathbb{Z}_3$ Symmetry (2HDMS). We derive a physical input basis and discuss theoretical constraints. These include unitarity constraints, boundedness from below and the stability of the electroweak vacuum. Furthermore we use experimental constraints from flavor physics, Higgs boson searches and measurements of the Standard Model Higgs boson to constrain the parameter space in this model. In this model we discuss a 3σ signal reported by CMS and LEP and interpret it as a light Higgs boson with a mass of 95 GeV. For this singlet-like state we evaluate the experimental coupling uncertainties at a future linear collider. Following that, we compare this to the similar N2HDM which is the extension of the 2HDM with a real singlet. We make first efforts to exploit experimental methods for distinguishing both models. We find that the 2HDMS and the N2HDM can both accomodate the excesses at LEP and CMS simultaneously and are difficult to distinguish using the evaluation of coupling uncertainties at a linear collider. Further possibilities to distinguish both models using the properties of the $\mathcal{CP}$-odd Higgs bosons are discussed.

In the second part of the thesis I explore the impact of a recent analysis published by CMS with searches for heavy Higgs bosons in final states with up to four top quarks. The original Beyond the Standard Model interpretation of the analysis is limited to strictly aligned $\mathcal{CP}$-even and $\mathcal{CP}$-odd Higgs bosons and to masses between 350 and 650 GeV. Furthermore it places strong constraints on the important quantity tanβ. In the 2HDM low values of this quantity are often needed to describe scenarios with baryogensis. We perform a recasting of this analysis with the Monte-Carlo-Event generator `Madgraph5` and the code `Madanalysis` to extend the analysis for more general types of models, such as models with $\mathcal{CP}$-violation and higher masses of up to 1 TeV. We obtain efficiencies in the most sensitive signal region and derive fit functions as a function of the mass. These fit functions are used to derive the efficiency as a function of the $\mathcal{CP}$-even, $\mathcal{CP}$-off top Yukawa and gauge-boson couplings. We implement our results in the code `Higgsbounds`, which can test models with multiple scalars against a large number of Higgs boson searches from LEP, CMS and Atlas. We then use this implementation to study the impact of the four-top analysis on the low tanβ region in the 2HDM, its singlet extensions and the complex 2HDM (C2HDM).

Zusammenfassung

In dem ersten Teil dieser Arbeit behandeln wir die erste Beschreibung des Two Higgs Doublet Models (2HDM) mit einem komplexen Singlet und einer $\mathbb{Z}_3$ Symmetrie. Wir leiten eine Basis mit physikalischen Massen her und diskutieren theoretische Einschränkungen. Diese beinhalten Unitarität, Boundedness-from-Below und die Stabilität des elektroschwachen Vakuums. Anschließend diskutieren wir experimentelle Einschränkungen, gegeben durch Suchen nach zusätzlichen Higgs Bosonen und Messungen der Eigenschaften des Standard Model Higgs Bosons. Wir nutzen dieses Model um ein 3σ Signal, welches von CMS und LEP beobachtet wurde, als ein leichtes Higgs Boson mit einer Masse von 95 GeV zu beschreiben. Wir evaluieren die Genauigkeit der Bestimmung der Kopplungen dieses leichten Higgs Bosons im Kontext eines zukünftigen linear Colliders. Wir vergleichen unsere Ergebnisse mit dem verwandten N2HDM, welches die Erweiterung des 2HDM mit einem reellen Singlet ist. Wir beobachten, dass beide Modelle den Excess beschreiben können und nur schwer durch die Messung der Genauigkeit der Kopplungen zu unterscheiden sind. Wir beschreiben weitere Möglichkeiten mit Hilfe der Eigenschaften der $\mathcal{CP}$-ungeraden Higgs Bosonen zur Unterscheidung beider Modelle.

In dem zweiten Teil dieser Arbeit diskutieren wir die Auswirkungen einer kürzlich veröffentlichten Analyse von CMS, die die Suche nach schweren Higgs Bosonen mit Endzuständen bis zu vier top quarks behandelt. Die originale Analyse beschränkt sich auf die Suche nach reinen $\mathcal{CP}$-geraden und $\mathcal{CP}$-ungeraden Higgs Bosonen ohne die Möglichkeit von gemischten Zuständen. Sie setzt weiterhin starke Einschränkungen im Bereich niedriger tanβ Werte, einer physikalischen Größe, die eine wichtige Rolle, bei der Beschreibung von Szenarien von Baryogenesis in 2HDMs spielt. Wir generieren Monte-Carlo-Events mit dem Code `Madgraph5` und führen ein Recasting mit dem Code `Madanalysis` durch. Dabei erweitern wir die Analyse bezüglich der Einbindung von $\mathcal{CP}$-gemischten Zuständen. Wir erhalten die Effizienzen in der sensitivsten Signal Region und leiten Funktionen in Abhängigkeit von der Masse her. Diese nutzen wir, um die Effizienzen als Funktion der $\mathcal{CP}$-geraden, $\mathcal{CP}$-ungeraden Top Yukawa and Gauge Boson Kopplung herzuleiten. Wir implementieren dies in dem Code `Higgsbounds`, der Modelle mit zusätzlichen Higgs Bosonen bezüglich der Kompatibilität mit einer großen Anzahl an Suchen nach Higgs Bosonen durch LEP, CMS und Atlas prüft. Wir nutzen diese Implementierung um die Auswirkung der vier Top Analyse auf den Bereich kleiner (< 2) tanβ Werte in dem 2HDM, seinen Singlet Erweiterungen und dem komplexen 2HDM (C2HDM) zu studieren.

List of Publications

Journal articles:

S. Heinemeyer, C. Li, F. Lika, G. Moortgat-Pick, and S. Paasch. A 96 gev higgs boson in the 2hdm plus singlet, 2021.

Wolfgang Gregor Hollik, Cheng Li, Gudrid Moortgat-Pick, and Steven Paasch. Phenomenology of a supersymmetric model inspired by inflation. The European Physical Journal C, 81(2), feb 2021.

Preprint:

Henning Bahl, Thomas Biekötter, Sven Heinemeyer, Cheng Li, Steven Paasch, Georg Weiglein, and Jonas Wittbrodt. Higgstools: Bsm scalar phenomenology with new versions of higgsbounds and higgssignals, 2022.

Acknowledgements

I want to express my gratitude to the many individuals who supported me on my PhD Journey. First of all, I am truly grateful for the guidance, support and many discussions inside and outside of physics with my supervisor Gudrid Moortat-Pick. I also want to thank Sven Heinemeyer for a long collaboration, spanning many projects. Many interesting topics emerged from this and were key to the direction of my Thesis.

I thank all members of the HiggsTools collaboration. The guidance and many discussions with Georg Weiglein, Thomas Biekötter, Sven Heinemeyer and Jonas Wittbrodt were essential for the success of my PhD projects. Here, I want to especially express my gratitude to Henning Bahl, who helped and guided me along every step of my project in the HiggsTools collaboration. I also want to thank every member of the THDM working group meeting, which was a great opportunity to present my work and discuss problems.

Thank you Juergen Reuter for ageeing to co-supervise my thesis and Michael Potthoff, Johannes Haller and Georg Weiglein for agreeing to be on the commitee of my disputation.

Thanks a lot to for everything Cheng Li. Our Journey in physics started with our master thesis and still continues. I will always remember the many discussions and problems we had to solve together.

I am thankful for the support of my family and friends. Their support made it possible for me to overcome challenging times. I especially thank my fiancee Jacky. In particular, for taking care of me when I was stressed and had to overcome difficult challenges, inside and outside of physics.

Contents

1 Introduction **1**

I The Standard Model **5**

2 The Standard Model of Particle Physics **7**

2.1 SM Higgs boson production and decay at the LHC 10

2.1.1 SM Higgs Pair Production and Self Coupling 11

2.2 Open Problems in the Standard Model 11

2.2.1 Dark Matter 12

2.2.2 Baryogenesis 14

II Extensions of the Standard Model **17**

3 Models with extended Higgs-sectors **19**

3.1 Two Higgs Doublet models 19

3.2 Singlet Extensions of Two Higgs Doublet models 21

3.2.1 N2HDM 23

3.2.2 2HDMS 26

3.2.3 Type II SM-like Higgs boson 30

3.2.4 Differences between the 2HDMS and the N2HDM 31

3.3 The Complex Two Higgs Doublet Model 32

4 Constraints on models with extended Higgs-sectors **35**

4.1 Theoretical Constraints 35

4.1.1 Tree-Level perturbative unitarity 35

4.1.2 Boundedness from below 38

4.1.3 Vacuum stability 39

4.2 Experimental Constraints 41

4.2.1 Measurement of Observed Higgs Bosons 41

4.2.2 Searches for Additional Higgs Bosons 44

4.2.3 Constraints from Flavor Physics 46

4.2.4 Electroweak Precision Observables 46

III A light Higgs Boson in Singlet Extensions of the Two

Higgs Doublet Model **51**

5 A light Higgs Boson in Singlet Extensions of the 2HDM **53**
5.1 The Experimental Excesses . . . 55
5.2 The Parameter Scan . . . 57
5.3 Preferred Parameter Spaces . . . 59
5.3.1 2HDMS . . . 59
5.3.2 N2HDM . . . 62
5.4 Prospects for e^+e^- colliders . . . 63
5.4.1 Precision on coupling measurements . . . 63
5.4.2 Measurements of the h2 couplings . . . 65

IV Four top final states as a probe of Two Higgs Doublet Models and its Extensions **69**

6 Four top final states as a probe of Two Higgs Doublet Models **71**
6.1 Higgs-top quark interaction at hadron colliders for $m_H > 2m_{top}$ . . . 72
6.1.1 Effective model description . . . 74
6.1.2 Cross section comparison of ttH, tWH and tH at the LHC . . . 74
6.2 Recasting process . . . 75
6.2.1 Cross-section fit formulas . . . 76
6.2.2 Cross-section and tanβ limits . . . 82
6.3 Impact on the low tanβ region in the 2HDM and its singlet extensions 87

7 Summary and Conclusion **92**

A Evaluation of experimental coupling uncertainties for a light Higgs boson **94**
A.1 SM Higgs-boson results . . . 94
A.2 Basic signal-background statistics . . . 95
A.3 Evaluation of uncertainties in the Higgs couplings . . . 96
A.3.1 Cross section evaluation . . . 96
A.3.2 Signal over background for the new Higgs boson . . . 97
A.3.3 Relating signal events to Higgs couplings . . . 98
A.3.4 Uncertainty in the Higgs couplings . . . 99

B Four-top analysis: details on implementation into `HiggsBounds` **102**

B.1 Monte-Carlo and detector-simulation 102
B.2 Cross-section coefficient fit functions 104
B.2.1 ttH-production 104
B.2.2 tWH-production 106
B.2.3 tH-production 109
B.3 Implementation in `HiggsBounds` 110

1 Introduction

The discovery of a Higgs boson at the Large Hadron Collider (LHC) marked a landmark for particle physics. Ten years after its discovery the Higgs program follows two main avenues: the precise determination of the properties of the discovered Higgs boson and the search for additional Higgs bosons. So far, neither significant deviations of the Standard Model (SM) predictions for the discovered Higgs boson nor evidence for other Higgs bosons has been found.

In recent years, the number of searches and precision measurements has steadily increased and an even larger amount of experimental results is expected with the upcoming LHC Run-III and the high-luminosity phase of the LHC (HL-LHC). Correspondingly, it will be an important task to correlate the various results and to investigate their implications for various models of Beyond-the-SM (BSM) physics.

In this work we will focus on one type of BSM models called Two Higgs Doublet models (2HDMs). We will study extensions of these types of models with real and complex singlets. These extensions are the N2HDM (real singlet), which was already studied in detail in [1], and the 2HDMS (complex singlet), which was introduced and studied in its most general case in [2]. However, we introduce an additional $\mathbb{Z}_3$-Symmetry to reduce the parameter space and get a Higgs sector similar to the Next-to-Minimal Supersymmetric Standard Model (NMSSM) (see [3]). This work is the first time where this model is studied in a broader phenomenological context, including theoretical constraints, constraints from experiments and the possibility to embed a light Higgs boson around ~ 96 GeV, which was reported as a $\sim 3\sigma$ local signal in the diphoton decay mode by CMS in [4] and with a $\sim 2\sigma$ local excess at the Large Electron-Positron Collider (LEP) in [5].

We will discuss these two excesses by accomodating them simultaneously in the N2HDM and the 2HDMS. We study the suitable parameter space in both models for describing the excesses and investigate possibilities to experimentally distinguish both models. Furthermore, we analyse the distinction of Higgs sectors of the N2HDM and 2HDMS at future colliders. We show what can be learned from the measurements of the couplings at a future e^+e^- colliders, where we focus on the International Linear Collider (ILC) with a center of mass energy of $\sqrt{s} = 250$ GeV (ILC250). In this analysis we show for the first time a phenomenological analysis of this light Higgs state at ~ 96 GeV including a calculation of the coupling measurement precision at the ILC250, which was described for the first time in [6]. We also present further approaches in distinguishing both model realizations.

Another part of this thesis arises as part of the work on the public code `HiggsTools` which incorporates the well known codes `HiggsBounds` and `HiggsSignals`. `HiggsSignals` calculates a χ^2 value which quantifies the agreement between the model prediction and the experimental data, which includes Higgs boson signal rates and masses at Tevatron and LHC results from ATLAS and CMS experiments. `HiggsBounds` checks whether a considered parameter point in a model is in agreement with Higgs boson searches, by comparing the theory predictions for all Higgs production processes and decay rates to existing searches. The search for contributions of a heavy BSM scalars to four-top final states have been studied by CMS in [7]. Higgs–top-quark interactions are an especially important part of BSM Higgs physics. For the discovered Higgs boson, the top-Yukawa coupling is the largest Yukawa coupling and plays a crucial role in various production and decay modes (see Sect. 6). While showing no significant over- or under-fluctuation, the upper limits on cross-section times branching-ratio place a strong lower limit on the important quantity $\tan\beta$ in 2HDMs. The analysis excludes $\tan\beta$ of up to 1.65 for a 2HDM with a mass degenerate scalar and pseudoscalar Higgs boson. This low $\tan\beta$ region is especially interesting for Baryogenesis scenarios in 2HDMs.

We reinterpret this analysis by generating Monte-Carlo Events in the most important sub- channels that can contribute to the four top cross-section, which are ttH, tWH and tH production, with `Madgraph5` and recast the Events using `Madanalysis`. We do this using the Higgs-characterization framework for an arbitrary scalar with CP-odd and CP-even couplings to top quarks and coupling to vector bosons. We implement this analysis in `HiggsBounds` which makes it accessible for a variety of models, including models with CP-violation and models with deviations from the alignment limit. We also expand the original mass range of $350 - 650$ GeV up to 1 TeV. Using this analysis we study the impact on the low $\tan\beta$ region in a number of models, including the 2HDM, the N2HDM and the complex 2HDM (C2HDM [8].)

Structure of the Thesis

This thesis is structured as follows. In Sect. 2 we give a short overview on the Standard Model (SM), which represents the best tested theory of particle physics and is the base for all BSM models. The need for BSM models arises from open questions that the SM can't describe. We discuss EW symmetry breaking, the particle content and a selected number of open questions.

In Sect. 3 we introduce the theoretical context of the 2HDM and its singlet extensions, the N2HDM and 2HDMS, which this work is focused on. The 2HDMS will be discussed in greater detail, as this is the first time that this model is described to an extent suitable for broad parameter scans and phenomenological analyses. We derive the $\mathbb{Z}_3$-symmetric 2HDMS from the work on the most general complex singlet extension of the 2HDM in [2]. We calculate the mass matrices and a physical input base. Further, we discuss the properties of the SM like Higgs boson and derive the alignment limit in the 2HDMS. In the end we discuss differences and similarities of the 2HDMS and the N2HDM.

In Sect. 4 we discuss the various theoretical and experimental constraints, where the parameter space of these models has to pass in order to describe scenarios that could be realized in nature. The theoretical constraints ensure that the potential parameters fulfill tree-level perturbative unitarity, i.e. controlled growth of scattering amplitudes with growing energy scale, boundedness from below of the potential and vacuum stability. Experimental constraints ensure that the properties of the predicted particles agree with measurements of the observed SM like Higgs boson, searches for BSM scalars and limits from flavor constraints as well as EW precision observables.

In Sect. 5 we describe the technical details of the above mentioned excess at 96 GeV reported by CMS and LEP. We study the parameter space which is suitable to accommodate both eccesses simultaneously in the N2HDM and 2HDMS. We follow up with an analysis of the coupling measurement precision at the ILC250. Furthermore, we discuss possibilities to distinguish both model realizations in experiments. In Sect. 6 we discuss the importance of studying the top-Yukawa interactions in the SM and the BSM models. We then describe the recasting process we carried out for the CMS four-top analysis and model applications in the low tanβ region and give more technical details of our implementation of the four-top analysis in appendix B.

Part I

The Standard Model

2 The Standard Model of Particle Physics

The Standard Model (SM) of Particle Physics is a quantum field theory (QFT) describing the elementary particles in nature and their interactions mediated by the electroweak force [9–13] and the strong force [14–18]. The SM does not contain a description of gravitational interactions. In this section an overview of the SM will be given based on [19–21].

The SM is the most general renormalizable QFT describing the known particle content and is invariant under the gauge symmetry

$$\mathrm{SU}(3)_c \otimes \mathrm{SU}(2)_L \otimes \mathrm{U}(1)_Y. \tag{2.1}$$

$\mathrm{SU}(2)_L \otimes \mathrm{U}(1)_Y$ is the gauge group of electroweak interactions operating on left-handed fermions (subscript L) and fields carrying the hypercharge Y. $\mathrm{SU}(3)_c$ is the gauge group of strong interactions operating on fields with color charge c. The fields of the SM are fermions (spin $\frac{1}{2}$), gauge bosons (spin 1) and a scalar boson (spin 0).

We will first have a look on the consequences of electroweak symmetry breaking on the bosonic sector of the SM, which is given by the Lagrangian

$$\begin{aligned} \mathcal{L}_{EW} &= -\frac{1}{4}B_{\mu\nu}B^{\mu\nu} - \frac{1}{4}W^a_{\mu\nu}W_a^{\mu\nu} + |D_\mu\Phi|^2 - V(\Phi), && (2.2)\\ V(\Phi) &= \mu^2|\Phi|^2 + \lambda|\Phi|^4. && (2.3) \end{aligned}$$

Φ is a complex scalar doublet with Hypercharge Y = 1 under $\mathrm{SU}(2)_L$ and $V(\Phi)$ is the most general, renormalisable Potential. The covariant derivative D_μ and field tensors $B_{\mu\nu}$ and $W^a_{\mu\nu}$ are given by

$$\begin{aligned} D_\mu &= \partial_\mu + ig\frac{\tau^a}{2}W_{\mu a} + ig'\frac{Y}{2}B_\mu, && (2.4)\\ B_{\mu\nu} &= \partial_\mu B_\nu - \partial_\nu B_\mu, && (2.5)\\ W^a_{\mu\nu} &= \partial_\mu W^a_\nu - \partial_\nu W^a_\nu - gf^{abc}W_{\mu b}W_{\nu c}. && (2.6)\\ & && (2.7) \end{aligned}$$

$W_{\mu\nu}^a$ and $B_{\mu\nu}$ are the gauge fields of the symmetry groups $\mathrm{SU}(2)_L$ and $\mathrm{U}(1)_Y$, respectively. The τ^a are the Pauli matrices, i.e. the generators of the SU(2) group, f^{abc} are the SU(2) structure constants and g and g' are the $\mathrm{SU}(2)_L$ and $\mathrm{U}(1)_Y$ gauge couplings, respectively. If the quadratic term $\mu^2 < 0$, the minimum of the potential is

$$\langle\Phi\rangle = \frac{1}{\sqrt{2}}\begin{pmatrix}0\\ \nu\end{pmatrix} \text{ with } \quad \nu = \sqrt{\frac{-\mu^2}{\lambda}}, \tag{2.8}$$

where the vev, $\nu \sim 246$ GeV, can be determined experimentally by measuring the Fermi constant G_F in the muon decay. The doublet field Φ can be expanded and expressed in terms of the vacuum expectation value (vev), the Higgs field h and three Goldstone bosons $\phi_{1,2,3}$,

$$\Phi = \frac{1}{\sqrt{2}}\begin{pmatrix}\phi_1 + i\phi_2\\ \nu + H + i\phi_3\end{pmatrix}. \tag{2.9}$$

The three massless Goldstone bosons are absorbed as longitudinal components of the three massive gauge bosons $W_\mu^\pm$, Z_μ and the massless photon A_μ. The eigenstates are given by

$$W_\mu^\pm = \frac{1}{\sqrt{2}}(W_\mu^1 \pm iW_\mu^2), \tag{2.10}$$

$$Z_\mu = c_w W_\mu^3 - s_w B_\mu, \tag{2.11}$$

$$A_\mu = s_w W_\mu^3 + c_w B_\mu. \tag{2.12}$$

We have introduced the weak mixing angle $\theta_W = arctan\,(g'/g)$, with $s_w = sin(\theta_W)$ and $c_w = cos(\theta_W)$. The Lagrangian describing the Higgs-gauge boson interaction can now be given as

$$\mathcal{L}_{hg} = \left[M_W^2 W_\mu^+ W^{-\mu} + \frac{1}{2}M_Z^2 Z_\mu Z^\mu\right]\left(1 + \frac{H}{v}\right)^2$$

$$-\frac{1}{2}M_H^2H^2-\frac{\lambda_{hhh}^{SM}}{3!}H^3-\frac{\lambda_{hhhh}^{SM}}{4!}H^4,$$

where

$$M_W=\frac{1}{2}gv,\quad M_Z=\frac{1}{2}v\sqrt{g^2+g'^2}, \tag{2.13}$$

$$M_H=\sqrt{2\lambda}v,\quad \lambda_{hhh}^{SM}=3\frac{M_H^2}{v},\quad \lambda_{hhhh}^{SM}=3\frac{M_H^2}{v^2}. \tag{2.14}$$

The two massive gauge bosons are related via

$$\frac{M_W}{M_Z}=\frac{g}{\sqrt{g^2+g'^2}}=c_w. \tag{2.15}$$

We will now briefly discuss the implications of EWSB on the fermion sector. The Yukawa interaction terms for the first generation of fermions are given by the Lagrangian

$$\mathcal{L}=y_u\bar{Q}_L\Phi_c u_R+y_d\bar{Q}_L\Phi d_R+y_e\bar{L}_L\Phi e_R+h.c., \tag{2.16}$$

where $\Phi_c=-i\tau_2\Phi^*$. A SU(2) transformation to the unitarity gauge brings Φ into the form

$$\Phi=\frac{1}{\sqrt{2}}\begin{pmatrix}0\\ v+H\end{pmatrix} \tag{2.17}$$

.

We can insert Eq.(2.17) into Eq.(2.16) and obtain

$$\mathcal{L}=m_u\bar{u}u\left(1+\frac{H}{v}\right)+m_d\bar{d}d\left(1+\frac{H}{v}\right)+m_e\bar{e}e\left(1+\frac{H}{v}\right) \tag{2.18}$$

where we define $\bar{x}x=x_L^\dagger x_R+x_R^\dagger x_L$ and $m_x=y_xv/\sqrt{2}$ with $x=u,d,e$. When this is extended to the three-family case, the Yukawa couplings $y_{u,d,e}$ become 3×3 matrices.

In Tab. 1 we summarize the resulting field content with the corresponding generations and their representation in the SM gauge groups.

gauge/matter Field	generations	$U_Y(1)$	$SU_L(2)$	$SU_c(3)$
B	1	0	1	1
W	1	0	3	1
G	1	0	1	8
q	$\begin{pmatrix} u \\ d \end{pmatrix}_L, \begin{pmatrix} c \\ s \end{pmatrix}_L, \begin{pmatrix} t \\ b \end{pmatrix}_L$	1/6	2	3
l	$\begin{pmatrix} \nu_\tau \\ \tau \end{pmatrix}_L, \begin{pmatrix} \nu_\mu \\ \mu \end{pmatrix}_L, \begin{pmatrix} \nu_e \\ e \end{pmatrix}_L$	-1/2	2	1
d	d_R, s_R, b_R	1/3	1	3
u	u_R, c_R, t_R	-2/3	1	3
e	τ_R, μ_R, e_R	1/2	2	1
Φ	1	1/2	2	1

Table 1: The Standard Model Field content categorized into the gauge and matter fields (left column). The last row represents the Higgs doublet, which contains the only scalar degree of freedom. The middle column shows the number of generations for each field and the notation used to distinguish each generation. The L and R denote respectively left- and right-handed states. The last three columns identify their representation in the SM gauge groups.

2.1 SM Higgs boson production and decay at the LHC

The Higgs boson was discovered at the LHC in pp collisions. The main production mechanisms are gluon fusion (ggF), Vector-boson fusion (VBF), production associated with a gauge boson (VH), a pair of top quarks ($t\bar{t}H$) or with a single top quark (tqH). The corresponding Feynman diagrams are shown in Fig. 1. In Fig. 2 (left) the contribution of these subchannels to the SM Higgs boson production cross sections is shown as a function of the center of mass energy $\sqrt{s}$. The blue line corresponds the production cross section via gluon fusion. The red line shows the same for Vector-boson fusion. The green and grey line show the cross section for production associated with a W or Z boson respectively. The pink and dark violet lines correspond to the cross section for Higgs production with a pair of bottom or top quarks respectively, whereas the light violet line shows the same for production with a single top quark [22].

On the right of Fig. 2 the branching ratios including QCD and EW corrections are shown for the decay of the SM Higgs boson. The dominant decay modes are $h \to b\bar{b}$, $h \to WW$, $h \to gg$, $h \to \tau\bar{\tau}$, $h \to c\bar{c}$ and $h \to ZZ$ [22].

2.1.1 SM Higgs Pair Production and Self Coupling

The measurement of the Higgs boson trilinear and quartic self couplings are an important direct probe of the SM. The tree level prediction from the SM are given in Eq. (2.14). Reconstructing the Higgs scalar potential will help to deepen our understanding of the EW phase transition.

The trilinear and quartic self couplings could in principle be measured directly using double and triple Higgs production processes. However, the hhh final state is constrained from very small production rates and intricate final states at the LHC [22]. The cubic self coupling can be constrained through measurements of double Higgs production at a hadron collider, where the production is dominated by gluon fusion $gg \to hh$ and at a lepton collider via Higgs-strahlung $e^+e^- \to Zhh$ especially at low energies, or VBF $e^+e^- \to hh\nu_e\bar{\nu}_e$ at higher energies of ≥ 1 TeV. The currently strongest limit at 95% C.L. on the trilinear Higgs self coupling was reported by ATLAS [23] at

$$-0.4 < \kappa_\lambda < 6.3, \tag{2.19}$$

where $\kappa_\lambda = \lambda_{hhh}/\lambda_{hhh}^{SM}$.

2.2 Open Problems in the Standard Model

Although the SM is in very good agreement with a large number of experimental observations, there are several shortcomings of the SM, which imply that there must be physics beyond the SM (BSM). We already mentioned that the SM doesn't contain a description of gravitational interactions. In the following we will a give an overview on further open problems in particle physics which can not be described by the SM.

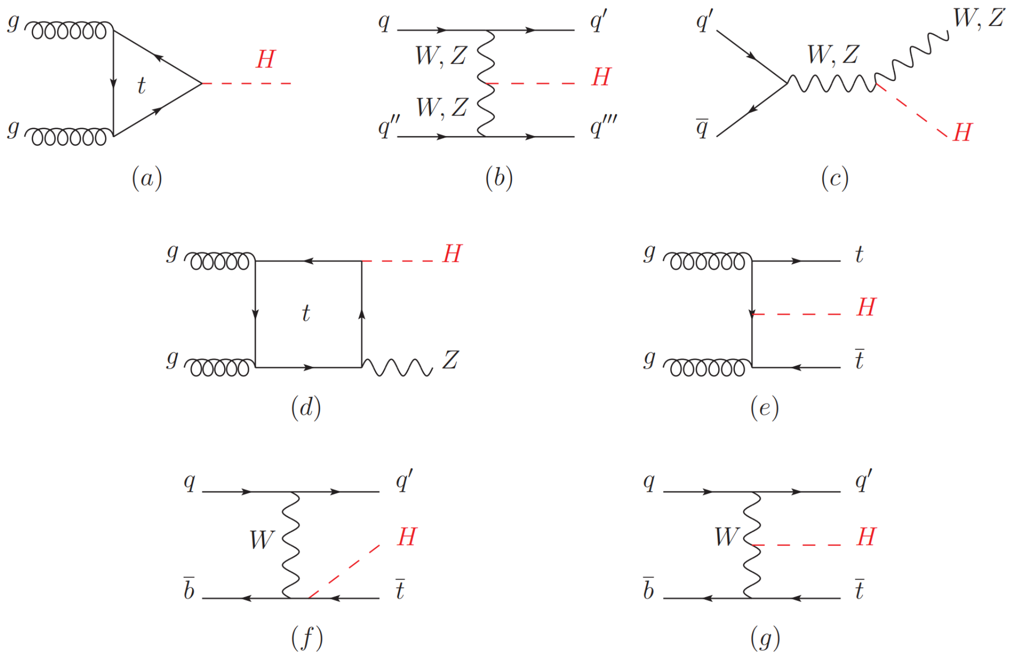

Figure 1: Main leading order Feynman diagrams contributing to the Higgs boson production at the LHC via (a) gluon fusion, (b) Vector-boson fusion, (c) Higgs-strahlung (or associated production with a gauge boson at tree level from a quark-quark interaction), (d) associated production with a gauge boson (at loop level from a gluon-gluon interaction), (e) associated production with a pair of top quarks. Taken from [22].

2.2.1 Dark Matter

There is evidence for gravitationally interacting and invisible matter, i.e. not or only weakly interacting with visible matter. It was first postulated by Zwicky [24, 25]. He measured the speed of individual galaxies in clusters of galaxies und calculated the mass of these clusters. By determining the mass of the visible matter by measuring the brightness of galaxies in the clusters he was able to show that typical galaxy clusters have around ten times more invisible than visible matter. Further astrophysical evidence for Dark Matter (DM) has since been found e.g. in the rotation curves of galaxies [26, 27], data from weak [28] and strong [29] lensing and measurements of the cosmic microwave background (CMB) [30]. The following short overview is based on [22].

One of the most important evidence is the measurement of the rotational curves of galaxies. The rotational velocity v on a stable Kepler orbit with a radius r scales with

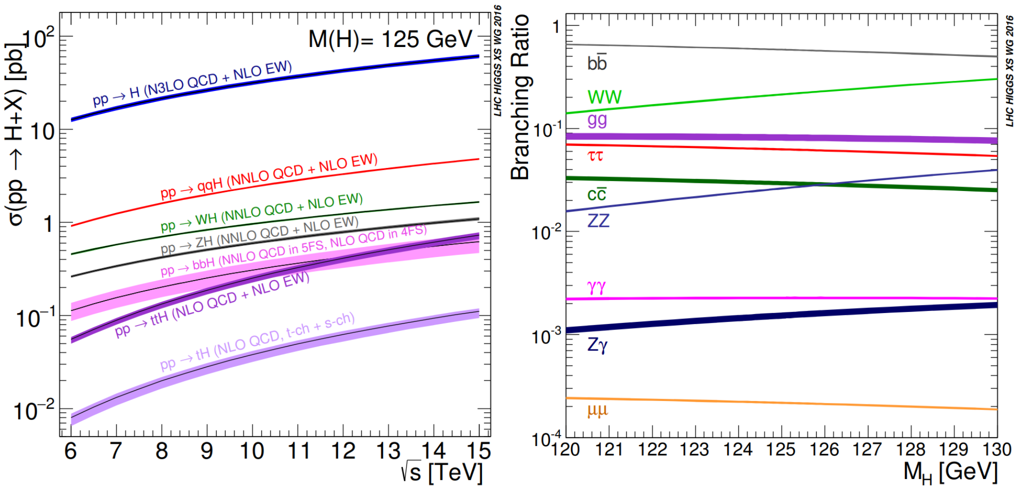

Figure 2: (Left): SM Higgs boson production cross sections depending on the center of mass energy $\sqrt{s}$ for pp collisions. (Right): SM Higgs boson branching ratios for the main decay channels near the observed Higgs boson mass of $m_H = 125$ GeV. Taken from [22].

$$v(r) \propto \sqrt{\frac{M(r)}{r}} \tag{2.20}$$

where $M(r)$ is the mass inside the orbit. Outside the part of a galaxie with visible matter, one would expect the velocity v to scale with $v(r) \propto \sqrt{1/r}$ when all the mass is inside the orbit with radius r. Instead one finds that v becomes approximately constant. This implies the existence of a dark matter halo which envelops galaxies with a mass density $\rho \propto 1/r^2$. This leads to a lower bound on the Dark matter mass density of $\Omega_{DM}h^2 \geq 0.1$.

Currently the most accurate value on the DM density comes from measurements of the cosmic microwave background (CMB) and the spatial distribution of galaxies leading to a density of

$$\Omega_{DM}h^2 = 0.1186 \pm 0.0020, \tag{2.21}$$

where h is the Hubble constant. DM candidates can be included in extensions of the SM. The particle has to be electrically neutral, a $SU(3)_c$ singlet and stable on cosmological scales. DM particles are allowed to interact with SM particles with couplings comparable to the weak interaction. Well studied DM candidates are weakly interacting massive particles (WIMPs). These particles have masses at the EW scale and couplings comparable to those of the weak interaction. The

WIMP-miracle describes the coincidence that these particles are produced in the early universe as thermal relics and produce a DM relic density in good agreement with the observed DM density.

There are experimental efforts to search for DM particles via direct and indirect detection. These searches rely on the scattering process between two DM particles and two SM particles S through a vertex as shown in Fig. 3.

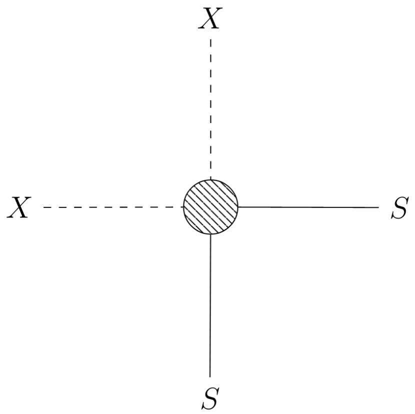

Figure 3: Scattering process of two DM particles X and two SM particles S.

Indirect detection looks at the annihilation of two DM particles X in cosmic rays. Additionally one can study the production of dark matter particles at colliders through initial state radiation pluss missing energy. These are called mono-X searches. Direct detection relies on the scattering of a dark matter particle off a SM particle, i.e. heavy nucleons. The Xenon experiment currently gives the strongest bounds for WIMPs via direct detection, see Fig. 4.

2.2.2 Baryogenesis

The observable universe exhibits a matter-antimatter asymmetry which can be estimated from the baryon to photon ratio η when assuming that all photons are created from annihilation processes of baryons. It can be obtained from CMB measurements [32] and is given by

$$\eta = \frac{n_b - n_{\bar{b}}}{n_\gamma} = 6.1 \times 10^{-10}. \tag{2.22}$$

To realize this baryon-asymmetry, which is necessary for the existence of ordinary matter, a model has to fulfill the three Sakharov criteria in the early universe. They

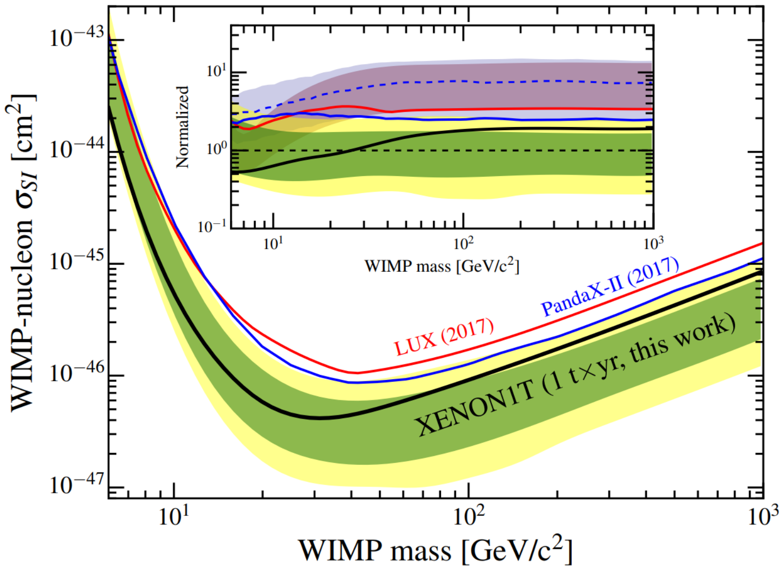

Figure 4: Limit on the dark matter nucleon scattering cross section are 90% confidence level as a function of the WIMP mass given by the XENON1T experiment [31].

are given by

- Baryon number (B) violation
- C and CP violation
- Departure from thermal equilibrium.

There are two different types of baryogenesis. In leptogenesis [33, 34] the CP-violating scattering processes of heavy neutrinos induce the baryon asymmetry. In electroweak baryogenesis the baryon asymmetry is generated through a strong first-order EW phase transition. Electroweak baryogenesis requries new physics at the EW scale, which makes it interesting when studying BSM models with extended Higgs sectors.

In order to realize a first-order EW phase transition in the SM, one would require a Higgs mass of $m_H \leq 60$ GeV which does not match the observed mass of $m_H = 125$ GeV. In models with extended Higgs sectors, which are studied in this work, a strong first-order EW phase transition can be realized (see. e.g. [35] for applications). A phase transition of this kind will progress with an expanding vacuum bubble which is out of thermal equilibrium and satisfy the third Sakharov criterion. During this phase transition baryon number violating sphaleron process will satisfy the first Sakharov criterion. Finally, when the BSM model introduces CP violating effects this will satisfy the second Sakharov criterion and generate a baryon asymmetry [36, 37].

Part II

Extensions of the Standard Model

3 Models with extended Higgs-sectors

In this section a description for the Two Higgs Doublet model and its real and complex singlet extensions is provided. We will discuss the vacuum structure, symmetries, mass matrices and couplings in the models respectively. Additionally we discuss a change of the basis from Lagrangian input parameters to physical masses and mixing angles.

3.1 Two Higgs Doublet models

The 2HDM extends the SM Higgs sector by a second $\mathrm{SU}(2)_L$ scalar doublet (see [38] for a detailed review). The most general scalar potential for two Higgs doublets Φ_1 and Φ_2 is given by:

$$\begin{aligned} V =& m_{11}^2 \Phi_1^\dagger \Phi_1 + m_{22}^2 \Phi_2^\dagger \Phi_2 - (m_{12}^2 \Phi_1^\dagger \Phi_2 + \text{h.c.}) + \frac{\lambda_1}{2} (\Phi_1^\dagger \Phi_1)^2 \\ &+ \frac{\lambda_2}{2} (\Phi_2^\dagger \Phi_2)^2 + \lambda_3 (\Phi_1^\dagger \Phi_1)(\Phi_2^\dagger \Phi_2) + \lambda_4 (\Phi_1^\dagger \Phi_2)(\Phi_2^\dagger \Phi_1) \\ &+ \left[\frac{\lambda_5}{2} (\Phi_1^\dagger \Phi_2)^2 + \lambda_6 (\Phi_1^\dagger \Phi_1)(\Phi_1^\dagger \Phi_2) + \lambda_7 (\Phi_1^\dagger \Phi_2)(\Phi_2^\dagger \Phi_2) + \text{h.c.} \right] \end{aligned} \tag{3.1}$$

The parameters m_{12}^2 and $\lambda_{5,6,7}$ can be complex and may lead to CP-violating scenarios. Both scalar doublets acquire a vev during EW symmetry breaking. These vevs v_1 and v_2 have to fulfill

$$v = \sqrt{v_1^2 + v_2^2} = 174 \text{GeV}. \tag{3.2}$$

The ratio of the two vevs v_1 and v_2 is defined as the parameter $\tan\beta$ as

$$\tan\beta = \frac{v_2}{v_1}. \tag{3.3}$$

The terms containing λ_6 and λ_7 will introduce flavor changing neutral currents (FCNC) for any coupling of Φ_1 and Φ_2 to fermions.

Flavor Changing Neutral Currents

In the the SM we have no tree-level flavor changing neutral currents as a consequence of the $\mathrm{SU}(2)_L \otimes \mathrm{U}(1)_Y$ gauge invariance. In the SM FCNCs only appear in loop-induced processes, which make them tiny but sensitive to BSM contributions. Considering the 2HDM the most general interaction of the doublets Φ_1 and Φ_2 to SM quarks is given by (see section 2 in [39] for more details):

$$-\mathcal{L}_Y = \bar{Q}_L(X_{d1}\Phi_1 + X_{d2}\Phi_2)d'_R + \bar{Q}_L(X_{u1}\Phi_1 + X_{u2}\Phi_2)u'_R \tag{3.4}$$

where $\Phi^c_{1(2)} = -i\tau_2\Phi^*_{1(2)}$ and the X_i are generic flavor space matrices. After EW symmetry breaking this leads to the quark mass matrices with $q \in \{u, d\}$

$$M_q = \frac{1}{\sqrt{2}}(v_1 X_{q1} + v_2 X_{q2}). \tag{3.5}$$

For generic X_i these matrices cannot be diagonalized simultaneously with the Yukawa interactions. This leads to FCNC couplings for some of the interactions. There are two approaches to keep the FCNC contributions small. In minimal flavor violation (MFV) it is assumed that the tree-level flavor symmetry of the SM is broken only by terms proportional to Yukawa couplings. In this case the flavor matrices X_i in eq. 3.4 are given by

$$X_{q1} = c_{q1}Y_q, X_{q2} = c_{q2}Y_q, \tag{3.6}$$

where Y_q are the SM Yukawa matrices and c are arbitrary prefactors. This keeps contributions to FCNCs small.
Another approach is natural flavor conservation (NFC), which guarantees the absence of tree-level FCNCs by allowing only one doublet Φ_i to couple to a fermion field. This means that either $X_{q1} = 0$ or $X_{q2} = 0$ for $q \in \{u, d\}$. Then the Yukawa interactions and quark masses are diagonalizable simultaneously and tree-level FCNCs are absent. This can be ensured by imposing discrete symmetries to the scalar potential and extending it to the Yukawa sector.

$\mathbb{Z}_2$-symmetry

In this work we encounter three discrete symmetries that reduce the number of free parameters in the 2HDM and in its extensions the N2HDM and the 2HDMS. The most commonly used symmetry ensuring the absence of FCNCs is called $\mathbb{Z}_2$-symmetry

	u-type	d-type	leptons	Q	u_R	d_R	L	l_R
type I	Φ_2	Φ_2	Φ_2	+	−	−	+	−
type II	Φ_2	Φ_1	Φ_1	+	−	+	+	−
lepton-specific	Φ_2	Φ_2	Φ_1	+	−	+	+	−
flipped	Φ_2	Φ_1	Φ_2	+	−	−	+	+

Table 2: In the three columns on the left the four Yukawa types of the $\mathbb{Z}_2$-symmetric 2HDM are defined by the coupling of each type of fermion to the Higgs doublets. The five columns to the right show the parity assignments of the fermions. Q and L are the quark and lepton doublets, u_R and d_R are the up- and down-type quark singlets and l_R is the lepton singlet.

and leading to four types of Yukawa structure in 2HDMs. Considering a 2HDM with two doublets Φ_1 and Φ_2 and a Singlet S, a $\mathbb{Z}_2$-symmetry transforms the fields as

$$\mathbb{Z}_2 \;:\; \Phi_1 \to \Phi_1, \qquad \Phi_2 \to -\Phi_2, \qquad S \to S. \tag{3.7}$$

It is assumed, without loss of generality, that up-type quarks only couple to Φ_2, i.e. $X_{d2} = 0$. This leaves four possible scenarios for the coupling of down-type quarks and leptons to the doublets. These coupling structures and the corresponding charge assignments are given in table 3.1. In the type I 2HDM all fermions couple to Φ_2. In the type II 2HDM up-type quarks couple to Φ_2 while down-type quarks and leptons couple to Φ_1. The coupling structure of the type II 2HDM is similar to that in supersymmetric extensions of the SM like the Minimal Supersymmetric Standard Model (MSSM) and the Next-to Minimal Supersymmetric Standard Model (NMSSM)(see [3, 40] for detailed reviews). There are two additional symmetries, called $\mathbb{Z}_2'$ and $\mathbb{Z}_3$, which can also be imposed on the potential of singlet extensions of the 2HDM. These will be discussed in the section 3.2.

3.2 Singlet Extensions of Two Higgs Doublet models

In this section we describe the N2HDM and the 2HDMS which can be obtained by extending the 2HDM with two doublets ϕ_1, ϕ_2 and a singlet S which is taken to be real (complex) in the N2HDM (2HDMS). After electroweak symmetry breaking, the doublet fields ϕ_1, ϕ_2 and the singlet field S aquire non zero vaccum expectation values (vevs). This means the fields can be expanded around these vevs and we get the expressions [6]:

$$\Phi_1 = \begin{pmatrix} \chi_1^+ \\ \phi_1 \end{pmatrix} = \begin{pmatrix} \chi_1^+ \\ v_1 + \frac{\rho_1 + i\eta_1}{\sqrt{2}} \end{pmatrix} \Phi_2 = \begin{pmatrix} \chi_2^+ \\ \phi_2 \end{pmatrix} = \begin{pmatrix} \chi_2^+ \\ v_2 + \frac{\rho_2 + i\eta_2}{\sqrt{2}} \end{pmatrix}$$

$$S = v_S + \frac{\rho_S + i\eta_S}{\sqrt{2}}, \tag{3.8}$$

where the η_S is absent in the N2HDM. The most general potential of a model with two doublets and one singlet is given by [2]

$$\begin{aligned} V =& m_{11}^2 \Phi_1^\dagger \Phi_1 + m_{22}^2 \Phi_2^\dagger \Phi_2 - (m_{12}^2 \Phi_1^\dagger \Phi_2 + \text{h.c.}) \\ &+ \frac{\lambda_1}{2}(\Phi_1^\dagger \Phi_1)^2 + \frac{\lambda_2}{2}(\Phi_2^\dagger \Phi_2)^2 + \lambda_3 (\Phi_1^\dagger \Phi_1)(\Phi_2^\dagger \Phi_2) + \lambda_4 (\Phi_1^\dagger \Phi_2)(\Phi_2^\dagger \Phi_1) \\ &+ \Big[\frac{\lambda_5}{2}(\Phi_1^\dagger \Phi_2)^2 + \lambda_6 (\Phi_1^\dagger \Phi_1)(\Phi_1^\dagger \Phi_2) + \lambda_7 (\Phi_2^\dagger \Phi_2)(\Phi_1^\dagger \Phi_2) + \text{h.c.}\Big] \\ &+ (\xi S + \text{h.c.}) + m_S^2 S^\dagger S + (\frac{{m'_S}^2}{2} S^2 + \text{h.c.}) \\ &+ \Big(\frac{\mu_{S1}}{6} S^3 + \frac{\mu_{S2}}{2} S S^\dagger S + \text{h.c.}\Big) + \Big(\frac{\lambda''_1}{24} S^4 + \frac{\lambda''_2}{6} S^2 S^\dagger S + \text{h.c.}\Big) + \frac{\lambda''_3}{4}(S^\dagger S)^2 \\ &+ \Big[S(\mu_{11}\Phi_1^\dagger \Phi_1 + \mu_{22}\Phi_2^\dagger \Phi_2 + \mu_{12}\Phi_1^\dagger \Phi_2 + \mu_{21}\Phi_2^\dagger \Phi_1) + \text{h.c.}\Big] \\ &+ S^\dagger S\Big[\lambda'_1 \Phi_1^\dagger \Phi_1 + \lambda'_2 \Phi_2^\dagger \Phi_2 + \lambda'_3 \Phi_1^\dagger \Phi_2 + \text{h.c.}\Big] \\ &+ \Big[S^2(\lambda'_4 \Phi_1^\dagger \Phi_1 + \lambda'_5 \Phi_2^\dagger \Phi_2 + \lambda'_6 \Phi_1^\dagger \Phi_2 + \lambda'_7 \Phi_2^\dagger \Phi_1) + \text{h.c.}\Big] \end{aligned} \tag{3.9}$$

with 29 free parameters. The N2HDM and 2HDMS can be obtained by applying a different set of symmetries to this potential.

Symmetries in singlet Extensions of the 2HDM

The N2HDM is obtained by imposing a $\mathbb{Z}'_2$ symmetry on the potential in eq. 3.9 in addition to the $\mathbb{Z}_2$ symmetry. It has the form

$$\mathbb{Z}'_2 \;:\; \Phi_1 \to \Phi_1, \qquad \Phi_2 \to \Phi_2, \qquad S \to -S. \tag{3.10}$$

It forbids all linear and cubic terms in the potential and gives rise to a conserved "darkness" quantum number if the singlet S does not acquire a vev. This gives rise to a singlet like dark matter candidate [1].

The 2HDMS is obtained by imposing an additional $\mathbb{Z}_3$ symmetry on the potential in eq. 3.9. It has the form

$$\begin{pmatrix} \Phi_1 \\ \Phi_2 \\ S \end{pmatrix} \rightarrow \begin{pmatrix} 1 & & \\ & e^{i2\pi/3} & \\ & & e^{-i2\pi/3} \end{pmatrix} \begin{pmatrix} \Phi_1 \\ \Phi_2 \\ S \end{pmatrix} \tag{3.11}$$

and makes the Higgs-sector of the 2HDMS similar to that of the NMSSM.

3.2.1 N2HDM

The N2HDM obeys the $\mathbb{Z}_2$ symmetries to avoid flavour-changing neutral currents (see section 3.1). Additionally the singlet S is odd under a $\mathbb{Z}_2'$ symmetry.
Applying the $\mathbb{Z}_2$ symmetry on the potential in eq. 3.9 sets the parameters $\lambda_6, \lambda_7, \lambda_3', \lambda_6', \lambda_7'$, which break the $\mathbb{Z}_2$ symmetry explicitely, to zero. The $\mathbb{Z}_2'$ requires all linear and cubic terms to be zero, i.e. $\mu_{S1,2}$, μ_{11}, μ_{22},μ_{12}, μ_{21} and ξ. We keep m_{12}, which softly breaks the $\mathbb{Z}_2$ symmetry. Furthermore, since the S is real, one has $S^\dagger = S$. Summing up all terms containing $S^2\Phi_1\Phi_1, S^2\Phi_2\Phi_2, S^4$ allows to redefine accordingly the coefficients

$$\lambda_1'' + \lambda_2'' \rightarrow \lambda_6 \ , \tag{3.12a}$$
$$\lambda_1' + \lambda_4' \rightarrow \lambda_7 \ , \tag{3.12b}$$
$$\lambda_2' + \lambda_5' \rightarrow \lambda_8 \tag{3.12c}$$

to meet the definitions in [1]. The potential then reads,

$$\begin{aligned} V_{\text{N2HDM}} =& m_{11}^2 \Phi_1^\dagger \Phi_1 + m_{22}^2 \Phi_2^\dagger \Phi_2 - (m_{12}^2 \Phi_1^\dagger \Phi_2 + \text{h.c.}) + \frac{\lambda_1}{2}(\Phi_1^\dagger \Phi_1)^2 + \frac{\lambda_2}{2}(\Phi_2^\dagger \Phi_2)^2 \\ &+ \lambda_3 (\Phi_1^\dagger \Phi_1)(\Phi_2^\dagger \Phi_2) + \lambda_4 (\Phi_1^\dagger \Phi_2)(\Phi_2^\dagger \Phi_1) + \frac{\lambda_5}{2}[(\Phi_1^\dagger \Phi_2)^2 + \text{h.c.}] \\ &+ \frac{1}{2} m_S^2 S^2 + \frac{\lambda_6}{8} S^4 + \frac{\lambda_7}{2}(\Phi_1^\dagger \Phi_1) S^2 + \frac{\lambda_8}{2}(\Phi_2^\dagger \Phi_2) S^2 \ . \end{aligned} \tag{3.13}$$

We can define $\tan\beta := v_2/v_1$ as in the 2HDM (see section 3.1). Therefore, we obtain $v = \sqrt{v_1^2 + v_2^2} = 174$ GeV based on our convention of the doublet fields (and internally for the N2HDM we use a definition with an additional factor of $1/\sqrt{2}$). After inserting the parametrizations for Φ_1, Φ_2 and Φ_S in Eq. (3.8) into the potential, followed by using using the minimization conditions:

$$\left.\frac{\partial V}{\partial \Phi_1}\right|_{\substack{\Phi_1=v_1\\ \Phi_2=v_2\\ S=v_S}} = \left.\frac{\partial V}{\partial \Phi_2}\right|_{\substack{\Phi_1=v_1\\ \Phi_2=v_2\\ S=v_S}} = \left.\frac{\partial V}{\partial S}\right|_{\substack{\Phi_1=v_1\\ \Phi_2=v_2\\ S=v_S}} = 0 \tag{3.14}$$

we obtain three minimum conditions given by

$$\frac{v_2}{v_1}m_{12}^2 - m_{11}^2 = \frac{1}{2}(v_1^2\lambda_1 + v_2^2\lambda 345 + v_S^2\lambda_7), \tag{3.15}$$

$$\frac{v_1}{v_2}m_{12}^2 - m_{22}^2 = \frac{1}{2}(v_1^2\lambda_{345} + v_2^2\lambda 2 + v_S^2\lambda_8), \tag{3.16}$$

$$-m_S^2 = \frac{1}{2}(v_1^2\lambda_7 + v_2^2\lambda 8 + v_S^2\lambda_6), \tag{3.17}$$

$$\tag{3.18}$$

with

$$\lambda_{345} = \lambda_3 + \lambda_4 + \lambda_5. \tag{3.19}$$

After using 3.3 and replacing m_{11}^2, m_{22}^2 and m_S^2 we now have 11 free parameters in the N2HDM,

$$\tan\beta,\ \lambda_1,\ \lambda_2,\ \lambda_3,\ \lambda_4,\ \lambda_5,\ \lambda_6,\ \lambda_7,\ \lambda_8\ m_{12}^2,\ v_S. \tag{3.20}$$

The charged Higgs sector of the N2HDM is identical to the structure in the 2HDM. The additional singlet mixes with the two doublets in the CP-even and CP-odd sector. This generates an additional pseudo-scalar Higgs boson in the N2HDM. We then have 3 scalar Higgs bosons h_1, h_2, h_3, the charged Higgs boson $H^\pm$ and one pseudo-scalar Higgs boson a_1. We use the convention $m_{h_1} < m_{h_2} < m_{h_3}$. The symmetric CP-even Higgs-boson mass eigenstates are obtained by diagonalizing the 3×3 mass matrix, M_S^2. By taking the second derivative of the scalar potential, one can obtain the tree level Higgs mass matrices:

$$M_{Sij}^2 = \left.\frac{\partial^2 V}{\partial\rho_i\partial\rho_j}\right|_{\substack{\Phi_1=v_1\\ \Phi_2=v_2\\ S=v_S}}, \qquad M_{Pij}^2 = \left.\frac{\partial^2 V}{\partial\eta_i\partial\eta_j}\right|_{\substack{\Phi_1=v_1\\ \Phi_2=v_2\\ S=v_S}}, \qquad M_{Cij}^2 = \left.\frac{\partial^2 V}{\partial\chi_i\partial\chi_j}\right|_{\substack{\Phi_1=v_1\\ \Phi_2=v_2\\ S=v_S}}. \tag{3.21}$$

For the CP-even mass matrix we find

$$
\begin{aligned}
M^2_{S11} &= 2\lambda_1 v^2 \cos^2\beta + m^2_{12}\tan\beta \ , && (3.22a)\\
M^2_{S22} &= 2\lambda_2 v^2 \sin^2\beta + m^2_{12}\cot\beta \ , && (3.22b)\\
M^2_{S12} &= (\lambda_3+\lambda_4+\lambda_5) v^2 \sin\beta\cos\beta - m^2_{12} \ , && (3.22c)\\
M^2_{S13} &= 2\lambda_7 v_S \cos\beta v \ , && (3.22d)\\
M^2_{S23} &= 2\lambda_8 v_S \sin\beta v \ , && (3.22e)\\
M^2_{S33} &= \lambda_6 v_S \ . && (3.22f)
\end{aligned}
$$

The diagonalization matrix is orthogonal and is given by the following 3×3 rotation matrix for the scalar case:

$$
R = \begin{pmatrix} c_{\alpha_1}c_{\alpha_2} & s_{\alpha_1}c_{\alpha_2} & s_{\alpha_2} \\ -s_{\alpha_1}c_{\alpha_3} - c_{\alpha_1}s_{\alpha_2}s_{\alpha_3} & c_{\alpha_1}c_{\alpha_3} - s_{\alpha_1}s_{\alpha_2}s_{\alpha_3} & c_{\alpha_2}s_{\alpha_3} \\ s_{\alpha_1}s_{\alpha_3} - c_{\alpha_1}s_{\alpha_2}c_{\alpha_3} & -s_{\alpha_1}s_{\alpha_2}c_{\alpha_3} - c_{\alpha_1}s_{a3} & c_{\alpha_2}c_{\alpha_3} \end{pmatrix} , \tag{3.23}
$$

where α_1, α_2 and α_3 are the three mixing angles. The mass basis and the interaction basis are related by,

$$
\begin{pmatrix} h_1 \\ h_2 \\ h_3 \end{pmatrix} = R \begin{pmatrix} \rho_1 \\ \rho_2 \\ \rho_S \end{pmatrix} , \quad \mathrm{diag}\{m^2_{h_1}, m^2_{h_2}, m^2_{h_3}\} = R^T M^2_S R \ . \tag{3.24}
$$

In the CP-odd sector such a rotation matrix is given by the 2×2 matrix

$$
R^A = \begin{pmatrix} c_\beta & s_\beta \\ -s_\beta & c_\beta \ , \end{pmatrix} . \tag{3.25}
$$

We perform a rotation of the basis of parameters in the potential to the physical masses and mixing angles. This is given by

$$\lambda_1 = \frac{1}{v^2\cos^2\beta}\left(\sum_i m_{h_i}^2 R_{i1}^2 - \hat{\mu}^2\sin^2\beta\right) \ , \tag{3.26a}$$

$$\lambda_2 = \frac{1}{v^2\sin^2\beta}\left(\sum_i m_{h_i}^2 R_{i2}^2 - \hat{\mu}^2\cos^2\beta\right) \ , \tag{3.26b}$$

$$\lambda_3 = \frac{1}{v^2}\left(\frac{1}{\sin\beta\cos\beta}\sum_i m_{h_i}^2 R_{i1}R_{i2} + 2m_{h^\pm}^2 - \hat{\mu}^2\right) \ , \tag{3.26c}$$

$$\lambda_4 = \frac{1}{v^2}\left(\hat{\mu}^2 + m_A^2 - 2m_{h^\pm}^2\right) \ , \tag{3.26d}$$

$$\lambda_5 = \frac{1}{v^2}\left(\hat{\mu}^2 - m_A^2\right) \ , \tag{3.26e}$$

$$\lambda_6 = \frac{1}{v_S^2}\sum_i m_{h_i}^2 R_{i3} \ , \tag{3.26f}$$

$$\lambda_7 = \frac{1}{v v_S\cos\beta}\left(\sum_i m_{h_i}^2 R_{i1}R_{i3}\right) \ , \tag{3.26g}$$

$$\lambda_8 = \frac{1}{v v_S\sin\beta}\left(\sum_i m_{h_i}^2 R_{i2}R_{i3}\right) \ , \tag{3.26h}$$

$$\tag{3.26i}$$

where $\hat{\mu}^2$ is defined as

$$\hat{\mu}^2 = \frac{m_{12}^2}{\sin\beta\cos\beta} \ . \tag{3.27}$$

This results in the new set of input parameters

$$\tan\beta, \quad \alpha_{1,2,3}, \quad m_{h_1}, \quad m_{h_2}, \quad m_{h_3}, \quad m_{a_1}, \quad m_{12}^2, \quad m_{H^\pm}, \quad v_S. \tag{3.28}$$

3.2.2 2HDMS

In this section we will present a first description of the 2HDMS (this was not done in the literature before). It is based on the work found in [2] which studies phenomenological aspects of the most general extension of the 2HDM with a complex singlet, without applying further symmetries. We introduce a $\mathbb{Z}_3$ symmetry to obtain a Higgs sector similar to the NMSSM. This leads to a scalar potential very similar to that of the N2HDM, but with 2 additional trilinear parameters μ_{12} and μ_{S1} which are forbidden in the $\mathbb{Z}_2'$ symmetric N2HDM, see above.

The 2HDMS obeys the $\mathbb{Z}_2$ symmetries to avoid flavour-changing neutral currents (see section 3.1). Additionally the Doublets Φ_1, Φ_2 and the Singlet S obey a $\mathbb{Z}_3$ symmetry similar to that in the NMSSM ([3]). This makes the Higgs-sector similar to that in the NMSSM without restrictions from SUSY.
Applying the $\mathbb{Z}_2$ symmetry on the potential in eq. 3.9 sets the parameters $\lambda_6, \lambda_7, \lambda'_3, \lambda'_6, \lambda'_7$, which break the $\mathbb{Z}_2$ symmetry explicitely, to zero. Imposing the $\mathbb{Z}_3$ Symmetry sets the $\mathbb{Z}_3$ breaking parameters $\lambda_5 = \lambda''_1 = \lambda''_2 = \lambda'_4 = \lambda'_5 = 0$. On the other hand, we keep the terms $m'_S, m_{12}, \mu_{S2}, \mu_{11}, \mu_{22}, \mu_{21}$, which softly break the $\mathbb{Z}_3$ symmetry. Taking the mapping of the 2HDMS to the NMSSM in [2] into account, we only keep m_{12} and μ_{12} as soft breaking parameters. The $\mathbb{Z}_3$-invariant potential then reads,

$$\begin{aligned} V_{\text{2HDMS}} =& m_{11}^2(\Phi_1^\dagger\Phi_1) + m_{22}^2(\Phi_2^\dagger\Phi_2) + \frac{\lambda_1}{2}(\Phi_1^\dagger\Phi_1)^2 + \frac{\lambda_2}{2}(\Phi_2^\dagger\Phi_2)^2 + \lambda_3(\Phi_1^\dagger\Phi_1)(\Phi_2^\dagger\Phi_2) \\ &+ \lambda_4(\Phi_1^\dagger\Phi_2)(\Phi_2^\dagger\Phi_1) + m_S^2(S^\dagger S) + \lambda'_1(S^\dagger S)(\Phi_1^\dagger\Phi_1) + \lambda'_2(S^\dagger S)(\Phi_2^\dagger\Phi_2) \\ &+ \frac{\lambda''_3}{4}(S^\dagger S)^2 + \Big(- m_{12}^2\Phi_1^\dagger\Phi_2 + \frac{\mu_{S1}}{6}S^3 + \mu_{12}S\Phi_1^\dagger\Phi_2 + \text{h.c.}\Big) \ . \end{aligned} \tag{3.29}$$

The definitions for $\tan\beta$ and the vevs are the same as in the N2HDM, see section 3.2.1. After using the minimization conditions in Eq. (3.14) we can again replace m_{11}^2, m_{22}^2 and m_S^2 by the tapdole equations

$$m_{11}^2 = (m_{12}^2 - \mu_{12}v_S)\frac{v_2}{v_1} - \lambda_1 v_1^2 - (\lambda_3 + \lambda_4)v_2^2 - \lambda'_1 v_S^2 \ , \tag{3.30}$$
$$m_{22}^2 = (m_{12}^2 - \mu_{12}v_S)\frac{v_1}{v_2} - \lambda_2 v_2^2 - (\lambda_3 + \lambda_4)v_1^2 - \lambda'_2 v_S^2 \ , \tag{3.31}$$
$$m_S^2 = -\frac{\mu_{S1}}{2}v_S - \frac{\lambda''_3}{2}v_S^2 - \mu_{12}\frac{v_1 v_2}{v_S} - \lambda'_1 v_1 - \lambda'_2 v_2^2 \ . \tag{3.32}$$
$$\tag{3.33}$$

We obtain 12 free parameters in the 2HDMS, coming from the additional degree of freedom,

$$\tan\beta,\ \lambda_1,\ \lambda_2,\ \lambda_3,\ \lambda_4,\ \lambda'_1,\ \lambda'_2,\ \lambda''_3,\ m_{12}^2,\ \mu_{S1},\ \mu_{12},\ v_S. \tag{3.34}$$

The charged Higgs sector of the 2HDMS is identical to the structure in the 2HDM.

The additional neutral singlet, however, mixes with the two doublets in the CP-even and CP-odd sector. This generates two additional pseudo-scalar Higgs bosons in the 2HDMS. We then have 3 scalar Higgs bosons h_1, h_2, h_3, the charged Higgs boson $H^\pm$ and two pseudo-scalar Higgs bosons a_1 and a_2. We use the conventions $m_{h_1} < m_{h_2} < m_{h_3}$ and $m_{a_1} < m_{a_2}$.

The CP-even Higgs-boson mass eigenstates are obtained by diagonalizing the 3×3 mass matrix, M_S^2. For the CP-even Higgs mass matrix one finds,

$$
\begin{aligned}
M^2_{S11} &= 2\lambda_1 v^2 \cos^2\beta + (m^2_{12} - \mu_{12} v_S)\tan\beta \ , && (3.35a)\\
M^2_{S22} &= 2\lambda_2 v^2 \sin^2\beta + (m^2_{12} - \mu_{12} v_S)\cot\beta \ , && (3.35b)\\
M^2_{S12} &= (\lambda_3 + \lambda_4) v^2 \sin 2\beta - (m^2_{12} - \mu_{12} v_S) \ , && (3.35c)\\
M^2_{S13} &= (2\lambda'_1 v_S \cos\beta + \mu_{12}\sin\beta) v \ , && (3.35d)\\
M^2_{S23} &= (2\lambda'_2 v_S \sin\beta + \mu_{12}\cos\beta) v \ , && (3.35e)\\
M^2_{S33} &= \frac{\mu_{s1}}{2} v_S + \lambda''_3 v_S^2 - \mu_{12}\frac{v^2}{2v_S}\sin 2\beta \ . && (3.35f)
\end{aligned}
$$

For the CP-odd Higgs sector we obtain

$$
\begin{aligned}
M^2_{P11} &= (m^2_{12} - \mu_{12} v_S)\tan\beta \ , && (3.36a)\\
M^2_{P22} &= (m^2_{12} - \mu_{12} v_S)\cot\beta \ , && (3.36b)\\
M^2_{P12} &= -(m^2_{12} - \mu_{12} v_S) \ , && (3.36c)\\
M^2_{P13} &= \mu_{12} v \sin\beta \ , && (3.36d)\\
M^2_{P23} &= -\mu_{12} v \cos\beta \ , && (3.36e)\\
M^2_{P33} &= -\frac{3}{2}\mu_{S1} v_S - \mu_{12}\frac{v^2}{2v_S}\sin 2\beta \ . && (3.36f)
\end{aligned}
$$

The charged Higgs Boson mass is given by

$$
M^2_C = 2(m^2_{12} - \mu_{12} v_S)\csc 2\beta - \lambda_4 v^2 \ . \tag{3.37}
$$

The scalar diagonalization matrix is orthogonal and is given by the same 3×3 rotation matrix as for the N2HDM (see section 3.2.1).

In the CP-odd sector the diagonalization matrix is given by

$$R^A = \begin{pmatrix} -s_\beta c_{\alpha_4} & c_\beta c_{\alpha_4} & s_{\alpha_4} \\ s_\beta s_{\alpha_4} & -c_\beta s_{\alpha_4} & c_{\alpha_4} \\ c_\beta & s_\beta & 0 \end{pmatrix} \tag{3.38}$$

$$\text{with} \quad \begin{pmatrix} a_1 \\ a_2 \\ \xi \end{pmatrix} = R^A \begin{pmatrix} \eta_1 \\ \eta_2 \\ \eta_S \end{pmatrix} \qquad \text{and} \qquad \mathrm{diag}\{m_{a_1}^2, m_{a_2}^2, 0\} = (R^A)^T M_P^2 R^A \ , \tag{3.39}$$

parametrized by the angle β and the CP-odd mixing angle α_4.

We perform, as in the case before, a rotation of the basis from the parameters to the physical masses and mixing angles. This is given by

$$\mu_{12} = \frac{m_{a_2}^2 - m_{a_1}^2}{v} \sin\alpha_4 \cos\alpha_4 \ , \tag{3.40a}$$

$$v_S = \frac{m_{12}^2 - \tilde{\mu}^2 \sin\beta\cos\beta}{\mu_{12}} \ , \tag{3.40b}$$

$$\mu_{S1} = -\frac{2}{3v_S}\left(\sin^2\alpha_4 m_{a_1}^2 + \cos^2\alpha_4 m_{a_2}^2 + \frac{v^2}{2v_S}\sin 2\beta\mu_{12}\right) \ , \tag{3.40c}$$

$$\lambda_1 = \frac{1}{2v^2\cos^2\beta}\left(\sum_i m_{h_i}^2 R_{i1}^2 - \tilde{\mu}^2 \sin^2\beta\right) \ , \tag{3.40d}$$

$$\lambda_2 = \frac{1}{2v^2\sin^2\beta}\left(\sum_i m_{h_i}^2 R_{i2}^2 - \tilde{\mu}^2 \cos^2\beta\right) \ , \tag{3.40e}$$

$$\lambda_3 = \frac{1}{v^2}\left(\frac{1}{\sin 2\beta}\sum_i m_{h_i}^2 R_{i1}R_{i2} + m_{h^\pm}^2 - \frac{\tilde{\mu}^2}{2}\right) \ , \tag{3.40f}$$

$$\lambda_4 = \frac{\tilde{\mu}^2 - m_{h^\pm}^2}{v^2} \ , \tag{3.40g}$$

$$\lambda_1' = \frac{1}{2v_S v\cos\beta}\left(\sum_i m_{h_i}^2 R_{i1}R_{i3} - \mu_{12} v \sin\beta\right) \ , \tag{3.40h}$$

$$\lambda_2' = \frac{1}{2v_S v\sin\beta}\left(\sum_i m_{h_i}^2 R_{i2}R_{i3} - \mu_{12} v \cos\beta\right) \ , \tag{3.40i}$$

	u-type	d-type	leptons
Type I	$\frac{R_{i2}}{s_\beta}$	$\frac{R_{i2}}{s_\beta}$	$\frac{R_{i2}}{s_\beta}$
Type II	$\frac{R_{i2}}{s_\beta}$	$\frac{R_{i1}}{c_\beta}$	$\frac{R_{i1}}{c_\beta}$
Lepton-Specific	$\frac{R_{i2}}{s_\beta}$	$\frac{R_{i2}}{s_\beta}$	$\frac{R_{i1}}{c_\beta}$
Flipped	$\frac{R_{i2}}{s_\beta}$	$\frac{R_{i1}}{c_\beta}$	$\frac{R_{i2}}{s_\beta}$

Table 3: Effective Yukawa couplings of the Higgs bosons H_i in the N2HDM and 2HDMS.

$$\lambda_3'' = \frac{1}{v_S^2}\left(\sum_i m_{h_i}^2 R_{i3}^2 + \mu_{12}\frac{v^2}{2v_S}\sin 2\beta - \frac{\mu_{S1}}{2}v_S\right) \ , \tag{3.40j}$$

where we define the parameter $\tilde{\mu}^2$ as,

$$\tilde{\mu}^2 = \frac{m_{12}^2 - v_S\mu_{12}}{\sin\beta\cos\beta} \equiv \cos^2\alpha_4 m_{a_1}^2 + \sin^2\alpha_4 m_{a_2}^2 \ . \tag{3.41}$$

This results in the new set of input parameters

$$\tan\beta, \quad \alpha_{1,2,3,4}, \quad m_{h_1}, \quad m_{h_2}, \quad m_{h_3}, \quad m_{a_1}, \quad m_{a_2}, \quad m_{H^\pm}, \quad v_S \tag{3.42}$$

for the 2HDMS.

The effective Yukawa couplings for the Higgs bosons H_i in the N2HDM and 2HDMS are the same and shown in Tab. 3.

3.2.3 Type II SM-like Higgs boson

Following Eq. (3.23), one finds that the singlet component of h_1 can be expressed by $|R_{13}|^2 = \sin^2\alpha_2$. In our study, the lightest scalar Higgs h_1 should be a singlet-dominant Higgs, which is motivated by the experimental excesses, see the discussion below, i.e. $\sin^2\alpha_2$ should be close to 1.

Since the type-II N2HDM is favored for interpreting the current experimental excess [41–45], we will stick to the type-II Yukawa structure for our analysis. We choose h_2 to be the SM-like Higgs, and one can obtain the reduced couplings of h_2 to t-quarsk, b-quarks and gauge bosons from Tab. 5, Eq. (3.23) and Eq. (5.4),

$$c_{h_2tt} = (c_{\alpha_1}c_{\alpha_3} - s_{\alpha_1}s_{\alpha_2}s_{\alpha_3})/s_\beta, \tag{3.43}$$

$$c_{h_2bb} = (-s_{\alpha_1}c_{\alpha_3} - c_{\alpha_1}s_{\alpha_2}s_{\alpha_3})/c_\beta, \tag{3.44}$$

$$c_{h_2VV} = c_{\alpha_3}s_{\beta-\alpha_1} - s_{\alpha_2}s_{\alpha_3}c_{\beta-\alpha_1}. \tag{3.45}$$

In the limit of $\sin^2\alpha_2 \to 1$, one can factor out $|\sin\alpha_2|$, and the h_2 couplings are approximately given by

$$c_{h_2tt} \approx \frac{\cos(\alpha_1 + \mathrm{sgn}(\alpha_2)\alpha_3)}{\sin\beta}|\sin\alpha_2|, \tag{3.46}$$

$$c_{h_2bb} \approx -\frac{\sin(\alpha_1 + \mathrm{sgn}(\alpha_2)\alpha_3)}{\cos\beta}|\sin\alpha_2|, \tag{3.47}$$

$$c_{h_2VV} \approx \sin(\beta - (\alpha_1 + \mathrm{sgn}(\alpha_2)\alpha_3))|\sin\alpha_2|. \tag{3.48}$$

These three reduced couplings, Eqs. (3.46)–(3.48), are required to be close to 1 for an SM-like h_2. The so-called alignment limit is thus reached for $\beta - (\alpha_1 + \mathrm{sgn}(\alpha_2)\alpha_3) \to \pi/2$. All three couplings of the h_2 are close to 1 simultaneously in this limit.

3.2.4 Differences between the 2HDMS and the N2HDM

As discussed above, the 2HDMS has an additional $\mathcal{CP}$-odd Higgs boson and an additional mixing angle α_4 compared to the N2HDM, because of the imaginary part of the singlet field. Therefore, the α_4 determines whether the lighter a_1 or the heavier a_2 plays the role of the singlet-like $\mathcal{CP}$-odd Higgs. By taking our convention for the $\mathcal{CP}$-odd mixing matrix in Eq. (3.38), the lighter $\mathcal{CP}$-odd Higgs a_1 would be singlet dominated when $\alpha_4 \to \pi/2$. Conversely, when $\alpha_4 \to 0$, the a_1 would be doublet-like and the heavier a_2 becomes singlet-like. If $\alpha_4 = \pi/4$, both a_1 and a_2 are admixtures of the singlet component and the doublet components. In the case $\alpha_4 \to \pi/4$, one could potentially distinguish the $\mathcal{CP}$-odd Higgs A in the N2HDM from the $\mathcal{CP}$-odd Higgs a_i in the 2HDMS with some singlet admixture, by comparing the decays of $A/a_i \to \tau^+\tau^-$ or $A/a_i \to t\bar{t}$. On the other hand, if α_4 is too close to 0 or $\pi/2$, the singlet dominant $\mathcal{CP}$-odd Higgs would completely decouple from the other SM particles, where the 2HDMS can be approximately in the "N2HDM limit", and only the doublet-like $\mathcal{CP}$-odd Higgs of the 2HDMS would remain potentially visible. In this case it would be difficult to resolve experimentally the difference in the couplings of the doublet-like $\mathcal{CP}$-odd Higgs to fermions.

However, even in the limit of $\alpha_4 = 0$ or $\pi/2$ the two models differ by their symmetries. The $\mathbb{Z}_3$ symmetry of the 2HDMS yields two additional trillinear terms μ_{12} and μ_{S1} in the Higgs potential. By neglecting the effect of the imaginary part of the singlet field, the λ_1', λ_2' and λ_3'' in Eq. (3.29) can play similar roles as λ_7, λ_8 and λ_6 in Eq. (3.13), respectively. On the other hand, the terms given by μ_{S1} and μ_{12} have no corresponding terms in the N2HDM. Consequently, these two terms can give additional contributions to triple-Higgs couplings which can be expressed as

$$\lambda_{h_ih_jh_k} = \lambda_{h_ih_jh_k}^{\text{N2HDM-like}} + \frac{\mu_{S1}}{2v} R_{i3}R_{j3}R_{k3} + \frac{\mu_{12}}{2v}(R_{i2}R_{j3} + R_{j2}R_{i3})R_{k1} \tag{3.49}$$

$$+ \frac{\mu_{12}}{2v}[(R_{i1}R_{j3} + R_{j1}R_{i3})R_{k2} + (R_{i1}R_{j2} + R_{j2}R_{i1})R_{k3}]. \tag{3.50}$$

Here the N2HDM-like part is the N2HDM triple Higgs couplings, but replacing the $\lambda_7, \lambda_8, \lambda_6$ by the $\lambda_1', \lambda_2', \lambda_3''$. In the limit of $\alpha_4 = 0$ or $\pi/2$, one finds $\mu_{12} = 0$ according to Eq. (3.40a). However, μ_{S1} would be non-zero as long as the singlet $\mathcal{CP}$-odd Higgs remains massive. In this case, the additional μ_{S1} contributions can lead to differences in $\lambda_{h_1h_1h_1}$, $\lambda_{h_1h_1h_2}$ and $\lambda_{h_1h_2h_2}$, since μ_{S1} is the trilinear self-coupling of the singlet field and the h_1 is the singlet dominated Higgs. This would lead to phenomenological differences, e.g., in various di-Higgs production modes at pp or e^+e^- colliders. On the other hand, the differences in the triple-Higgs couplings with h_3 involved, would be relatively small and difficult to detect in the decay $h_3 \to h_ih_j$. We leave such studies for future work.

In principle, the μ_{S1} term can also vanish in the case of a massless $\mathcal{CP}$-odd singlet Higgs according to (3.40c). In this case the triple-Higgs couplings can be similar in both models in the limit of $\alpha_4 \to \pi/2$ and $m_{a_1} \to 0$. However, the decay channel of $h_2 \to a_1a_1$ would then be open ($m_{h_2} > 2m_{a_1}$), which would drastically change the behavior of the Higgs at ~ 125 GeV.

3.3 The Complex Two Higgs Doublet Model

The complex two Higgs doublet model (C2HDM) has an explicitly $\mathcal{CP}$-violating scalar potential, with a softly broken $\mathbb{Z}_2$ symmetry. The following, brief description is based on Ref. [8].

The scalar potential can be written as

$$
\begin{aligned}
V =& m_{11}^2\Phi_1^\dagger\Phi_1 + m_{22}^2\Phi_2^\dagger\Phi_2 - (m_{12}^2\Phi_1^\dagger\Phi_2 + \text{h.c.}) + \frac{\lambda_1}{2}(\Phi_1^\dagger\Phi_1)^2 \\
&+ \frac{\lambda_2}{2}(\Phi_2^\dagger\Phi_2)^2 + \lambda_3(\Phi_1^\dagger\Phi_1)(\Phi_2^\dagger\Phi_2) + \lambda_4(\Phi_1^\dagger\Phi_2)(\Phi_2^\dagger\Phi_1) \\
&+ \left[\frac{\lambda_5}{2}(\Phi_1^\dagger\Phi_2)^2 + \text{h.c.}\right]
\end{aligned} \tag{3.51}
$$

All parameters are real, except for m_{12}^2 and λ_5. The doublet fields take the known form of

$$
\Phi_1 = \begin{pmatrix} \chi_1^+ \\ v_1 + \dfrac{\rho_1 + i\eta_1}{\sqrt{2}} \end{pmatrix}, \qquad \Phi_2 = \begin{pmatrix} \chi_2^+ \\ \dfrac{v_2 + \rho_2 + i\eta_2}{\sqrt{2}} \end{pmatrix}. \tag{3.52}
$$

There are two $\mathcal{CP}$-violating phases $\phi(m_{12}^2)$ and $\phi(\lambda_5)$, defined as

$$
m_{12}^2 = |m_{12}^2|e^{i\phi(m_{12}^2)}, \quad \lambda_5 = |\lambda_5|e^{i\phi(\lambda_5)}. \tag{3.53}
$$

The rotation matrix is the same as given in Eq. (3.23). Diagonalization and basis change, as discussed in the previous sections, leads to the minimum conditions

$$
m_1 1^2 v_1 + \frac{\lambda_1}{2}v_1^3 + \frac{\lambda_{345}}{2}v_1 v_2^2 = \text{Re}(m_{12}^2)v_2 \ , \tag{3.54}
$$

$$
m_2 2^2 v_2 + \frac{\lambda_1}{2}v_2^3 + \frac{\lambda_{345}}{2}v_1^2 v_2 = \text{Re}(m_{12}^2)v_1 \ , \tag{3.55}
$$

$$
2\text{Im}(m_{12}^2) = v_1 v_2 \text{Im}(\lambda_5) \ , \tag{3.56}
$$

where we now have

$$
\lambda_{345} = \lambda_3 + \lambda_4 + \text{Re}(\lambda_5). \tag{3.57}
$$

This results in the following set of input parameters.

$$
v, \ \tan\beta, \ \alpha_1, \ \alpha_2, \ \alpha_3, \ m_{H_i}, \ m_{H_j}, \ m_{H^\pm}, \ \text{Re}(m_{12}^2). \tag{3.58}
$$

	u-type	d-type	leptons
Type I	$\frac{R_{i2}}{s_\beta} - i\frac{R_{i3}}{t_\beta}\gamma_5$	$\frac{R_{i2}}{s_\beta} + i\frac{R_{i3}}{t_\beta}\gamma_5$	$\frac{R_{i2}}{s_\beta} + i\frac{R_{i3}}{t_\beta}\gamma_5$
Type II	$\frac{R_{i2}}{s_\beta} - i\frac{R_{i3}}{t_\beta}\gamma_5$	$\frac{R_{i1}}{c_\beta} - iR_{i3}t_\beta\gamma_5$	$\frac{R_{i1}}{c_\beta} - iR_{i3}t_\beta\gamma_5$
Lepton-Specific	$\frac{R_{i2}}{s_\beta} - i\frac{R_{i3}}{t_\beta}\gamma_5$	$\frac{R_{i2}}{s_\beta} + i\frac{R_{i3}}{t_\beta}\gamma_5$	$\frac{R_{i1}}{c_\beta} - iR_{i3}t_\beta\gamma_5$
Flipped	$\frac{R_{i2}}{s_\beta} - i\frac{R_{i3}}{t_\beta}\gamma_5$	$\frac{R_{i1}}{c_\beta} - iR_{i3}t_\beta\gamma_5$	$\frac{R_{i2}}{s_\beta} + i\frac{R_{i3}}{t_\beta}\gamma_5$

Table 4: Effective Yukawa couplings of the Higgs bosons H_i in the C2HDM

Here m_{H_i} and m_{H_j} denote two of the three neutral Higgs boson masses. The third mass is not an independent parameter and is calculated from the other parameters by

$$m_{H_3} = \frac{m_{H_1}^2 R_{13}(R_{12}\tan\beta - R_{11}) + m_{H_2}^2 R_{23}(R_{22}\tan\beta - R_{21}}{R_{33}(R_{31} - R_{23}\tan\beta)}. \tag{3.59}$$

The couplings, including $\mathcal{CP}$-violating admixtures are given in Tab. 4.

4 Constraints on models with extended Higgs-sectors

In this section we will discuss the various theoretical and experimental constraints on BSM models. The general principle of each constraint and its application for the 2HDMS and N2HDM will be discussed. Each point of a parameter scan is required to fulfill various theoretical and experimental constraints. Theoretical constraints directly influence the allowed values of the parameters in the model Lagrangian. When a benchmark point passes all theoretical constraints it is tested against experimental constraints, which test the measured properties of the predicted particles and general limits from searches.

The calculation of constraints in the 2HDMS was a crucial part in the publication [6], on which this section is based. My contribution to this section was the calculation of conditions to fulfill tree-level perturbative unitarity, boundedness from below and vacuum stability constraints. I also carried out the calculation of the oblique parameters S,T and U coming from EW precision measurements.

4.1 Theoretical Constraints

The 2HDMS and the N2HDM face constraints from all mentioned constraints. In the following we show the conditions for the 2HDMS. For the N2HDM these conditions were already derived in [46] (see below).

4.1.1 Tree-Level perturbative unitarity

Tree-level perturbative unitarity conditions ensure perturbativity of the model up to very high scales. They ensure a controlled growth of the scattering amplitude with growing energy scale. A scattering amplitude can be decomposed into partial waves [47]

$$\mathcal{M}(\theta) = 16\pi \sum_{l=0}^{\infty} (2l+1) P_l(cos\theta) a_l, \tag{4.1}$$

where P_l are the Legendre polynomials of degree l, θ is the scattering angle and a_l are coefficients that can be extracted by an orthogonality condition. The $2 \to 2$ scattering cross-section is given by

$$\sigma = \frac{16\pi}{s} \sum_l (2l+1)|a_l|^2, \tag{4.2}$$

where s is the center of mass energy. The cross-section can be related to the scattering amplitude with the optical theorem:

$$\sigma = \frac{1}{s}\ \mathrm{Im}\mathcal{M}(\theta = 0) = \frac{1}{s}\ 16\pi(2l+1)\ Im\ a_l. \tag{4.3}$$

This can be rewritten as a circle in the complex plane as

$$(\mathrm{Re}\ a_l)^2 + (\mathrm{Im}\ a_l - \frac{1}{2})^2 = \frac{1}{4}, \tag{4.4}$$

which results in the the condition

$$|a_l| < \frac{1}{2}. \tag{4.5}$$

In the high energy limit the leading contributions to the scattering amplitude do not have angular dependence and thus only $\mathcal{M}_0$ contributes to the full tree-level matrix element $\mathcal{M}$. Taking the normalization factor of 16π from the partial wave expansion into account we can write the tree-level perturbative unitarity constraint as [48]

$$\mathcal{M} \leq 8\pi. \tag{4.6}$$

Following the procedure of [48] and using a `Mathematica` package implemented in `ScannerS` [49] the conditions can be calculated for any model with an extended scalar sector.

Tree-level perturbative unitarity in the 2HDMS

We carried out the calculation in the 2HDMS and found the following conditions:

$$|\lambda'_{1,2}| < 8\pi, \tag{4.7}$$

$$|\frac{\lambda_3''}{2}| < 8\pi, \tag{4.8}$$

$$|\lambda_{1,2,3}| < 8\pi, \tag{4.9}$$

$$|\lambda_3 \pm \lambda_4| < 8\pi, \tag{4.10}$$

$$|\frac{1}{2}(\lambda_1 + \lambda_2 \pm \sqrt{(\lambda_1 - \lambda_2)^2 + 4\lambda_4^2})| < 8\pi. \tag{4.11}$$

For models with extended scalar-sectors the calculation cannot be carried out purely analytically. All other eigenvalues are given by the three real roots (x_1, x_2, x_3) of the cubic polynomial

$$\begin{aligned}
&64\,(6\lambda_2'^2\lambda_1 + 6\lambda_1'^2\lambda_2 - 9\lambda_3''\lambda_1\lambda_2 - 8\lambda_1'\lambda_2'\lambda_3 + 4\lambda_3''\lambda_3^2 - 4\lambda_1'\lambda_2'\lambda_4 + 4\lambda_3''\lambda_3\lambda_4 + \lambda_3''\lambda_4^2) \\
&+ 16\,(-2\lambda_1'^2 - 2\lambda_2'^2 + 3\lambda_3''\lambda_1 + 3\lambda_3''\lambda_2 + 9\lambda_1\lambda_2 - 4\lambda_3^2 - 4\lambda_3\lambda_4 - \lambda_4^2)\,x \\
&+ (-4\lambda_3'' - 12\lambda_1 - 12\lambda_2)\,x^2 + \,x^3 = 0,
\end{aligned} \tag{4.12}$$

$$\left|\frac{x_1}{4}\right| < 8\pi, \qquad \left|\frac{x_2}{4}\right| < 8\pi, \qquad \left|\frac{x_3}{4}\right| < 8\pi \tag{4.13}$$

Tree-level perturbative unitarity in the N2HDM

In the N2HDM perturbative unitarity constraints were already derived in [46] [see their Eqs. (3.43)–(3.48)]:

$$|\lambda_{7,8}| < 8\pi, \tag{4.14}$$

$$|\lambda_3 - \lambda_4| < 8\pi, \tag{4.15}$$

$$|\lambda_{1,2,3}| < 8\pi, \tag{4.16}$$

$$|\lambda_3 + 2\lambda_4 \pm 2\lambda_5| < 8\pi, \tag{4.17}$$

$$|\frac{1}{2}(\lambda_1 + \lambda_2 \pm \sqrt{(\lambda_1 - \lambda_2)^2 + 4\lambda_4^2})| < 8\pi, \tag{4.18}$$

$$|\frac{1}{2}(\lambda_1 + \lambda_2 \pm \sqrt{(\lambda_1 - \lambda_2)^2 + 4\lambda_5^2})| < 8\pi. \tag{4.19}$$

Again, all remaining eigenvalues are given by the three real roots (x_1, x_2, x_3) of the cubic polynomial

$$
\begin{aligned}
&4\left(-27\lambda_1\lambda_2\lambda_6 + 12\lambda_3^2\lambda_6 + 12\lambda_3\lambda_4\lambda_6 + 3\lambda_4^2\lambda_6 + 6\lambda_2\lambda_7^2 - 8\lambda_3\lambda_7\lambda_8 - 4\lambda_4\lambda_7\lambda_8 + 6\lambda_1\lambda_8^2\right)\\
&+ \left(36\lambda_1\lambda_1 2 - 16\lambda_3^2 - 16\lambda_3\lambda_4 - 4\lambda_4^2 + 18\lambda_1\lambda_6 + 18\lambda_2\lambda_6 - 4\lambda_7^2 - 4\lambda_8^2\right) x\\
&+ \left(-6(\lambda_1+\lambda_2) - 3\lambda_6\right) x^2 + x^3 = 0,
\end{aligned}
\tag{4.20}
$$

$$
\left|\frac{x_1}{4}\right| < 8\pi, \qquad \left|\frac{x_2}{4}\right| < 8\pi, \qquad \left|\frac{x_3}{4}\right| < 8\pi. \tag{4.21}
$$

4.1.2 Boundedness from below

The boundedness from below conditions ensure that the potential remains positive when the field values Φ approach infinity. In other words, boundedness from below ensures the existence of a global minimum. This is shown in Fig. 5. For simple models with a small number of parameters in the potential it can be straightforward to point out the values of the parameters for which the Higgs potential is bounded from below. In models with extended Higgs sectors, the Higgs potential can have very complicated structures. This is the case for the 2HDM and it's extensions, which can have multiple scalar doublets and singlets. For these models the conditions for the parameter space, under which the potential is bounded from below, become non-trivial. The corresponding conditions and more details can be found in [50] and were adapted for the 2HDMS. The allowed region is given by

$$
\Omega_1 \cup \Omega_2 \tag{4.22}
$$

with

$$
\Omega_1 = \left\{\lambda_1, \lambda_2, \lambda_3'' > 0; \sqrt{\frac{\lambda_1\lambda_3''}{2}} + \lambda_1' > 0; \sqrt{\frac{\lambda_2\lambda_3''}{2}} + \lambda_2' > 0;\right. \tag{4.23}
$$

$$
\left.\sqrt{\lambda_1\lambda_2} + \lambda_3 + D > 0; \lambda_1' + \sqrt{\frac{\lambda_1}{\lambda_2}}\lambda_2' \geq 0\right\} \tag{4.24}
$$

and

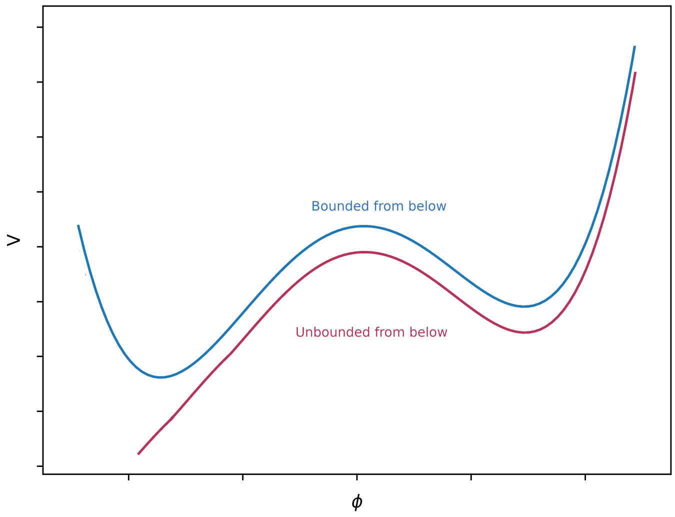

Figure 5: Schematic example of a potential bounded (blue) and unbounded(red) from below.

$$\Omega_2 = \Bigg\{\lambda_1, \lambda_2, \lambda_3'' > 0; \sqrt{\frac{\lambda_2\lambda_3''}{2}} \geq \lambda_2' > -\sqrt{\frac{\lambda_2\lambda_3''}{2}}; -\sqrt{\frac{\lambda_1}{\lambda_2}}\lambda_2' \geq \lambda_1' > -\sqrt{\frac{\lambda_1\lambda_3''}{2}}; \tag{4.25}$$

$$\frac{(D+\lambda_3)\lambda_3''}{2} > \lambda_1'\lambda_2' - \sqrt{(\lambda_1'^2 - \frac{\lambda_1\lambda_3''}{2})(\lambda_2'^2 - \frac{\lambda_2\lambda_3''}{2})}\Bigg\}, \tag{4.26}$$

where

$$D = \begin{cases} \lambda_4 & \text{for } \lambda_4 < 0 \\ 0 & \text{for } \lambda_4 \geq 0 \end{cases} . \tag{4.27}$$

The corresponding conditions for the N2HDM were already derived in [46] (see their Eqs. (3.51) and (3.52)).

4.1.3 Vacuum stability

In the SM the electroweak (EW) vacuum is required to be stable at the EW scale. This vacuum state is characterised by a non-zero vev of the Higgs field. In BSM theories vacuum stability at the EW scale places additional constraints on their extended parameter space. An obvious condition is to require the EW vacuum to be the global minimum (*true vacuum*) of the scalar potential. In this case the EW vacuum is absolutely stable. If the EW vacuum is a local minimum (*false vacuum*) the corresponding parameter region can still be allowed if it is sufficiently metastable. This is the case if the predicted lifetime of the false vacuum is longer than the current age of the universe. Any configuration with a lifetime shorter than the age of the universe is considered unstable.

Following [51] the decay of a false vacuum and thus the stability of the EW vacuum can be described by the so-called bounce action. Considering a single real field Lagrangian, which is bounded from below

$$\mathcal{L} = \frac{1}{2}(\partial\Phi)^2 - V(\Phi), \tag{4.28}$$

it was found in [52, 53] that the decay rate Γ of a metastable vacuum state per (spatial) volume V_S is given by

$$\frac{\Gamma}{V_S} = Ke^{-B}, \tag{4.29}$$

where B is the bounce action and K is a dimensionful parameter, $[K] = \text{GeV}^4$, that can be estimated from a typical scale $\mathcal{M}$ of the theory as

$$K = \mathcal{M}^4. \tag{4.30}$$

Since the decay rate Γ is mostly sensitive to the bounce action B and varying the scale $\mathcal{M}$ over a range from 10 GeV to 100 TeV shifts the border between metastability and instability by less than 10%, points where $B > 440$ are considered as long lived and points where $B < 390$ as short-lived. The intermediate range $390 < B < 440$ is considered as an uncertainty threshold from $\mathcal{M}$. For further details see section 3 in [51].

For our study we used `EVADE` [54–56] which finds the tree-level minima employing `HOM4PS2` [57]. In the case of the EW vacuum being a false vacuum, it calculates the bounce action for a given parameter point with a straight path approximation, which is sufficiently accurate for the purpose, see [55].

We additionally made a detailed comparison of the results of the straight path approximation of `EVADE` with the more sophisticated approach via path deformation of the code `FindBounce` [58] and `Vevacious++` [59]. In Fig. 7 the concept of a straight path and correct bounce path connecting two local minima in a two-dimensional scalar potential is shown. As can be seen in Fig. 6 the enhancement by the computationally more intensive `FindBounce` is negligible. The border between metastable (yellow) and unstable (red) regions is very similar for `Vevacious++` at tree-level and `FindBounce`, which both use path deformation in the calculation of the bounce action. They also put a stricter constraint on the metastable regions compared to `EVADE`. As expected for all three the stable region shown in green is the same, because for these points the EW vacuum is the global minimum of the potential. The code `Vevacious++` at 1-loop level suffers from numerical instabilities and cannot be considered for the calculation of the bounce action. Overall all three codes were in good agreement and we chose the actively developed code `EVADE` for our study.

4.2 Experimental Constraints

Parameter points in BSM models that fulfill all theoretical constraints have to be tested against current experimental results. Any new scalars have to be allowed by searches for additional Higgs bosons. These most commonly come with upper limits on the cross-section times branching ratio for a specfic search channel or upper limits on couplings. Additionally one of the scalars has to be SM-like and in agreement with measurements of the observed Higgs boson at ~ 125 GeV. Constraints from flavor physics give lower limits on the charged scalar masses and the S, T and U parameters study one-loop corrections of BSM physics to EW precision observables.

4.2.1 Measurement of Observed Higgs Bosons

Since it's discovery in 2012 we did not observe any significant deviation of the properties of the Higgs boson from the SM. This makes it necessary that parameter points in any BSM models provide a scalar that agrees with the properties of the observed Higgs boson at a mass of 125 GeV. For such tests we use the public code `HiggsSignals-3` [61–66]. The code is part of `HiggsTools` [67] and calculates a χ^2 value which quantifies the agreement between the model prediction and the experimental data, which includes Higgs boson signal rates and masses from CDF results at Tevatron and LHC results from ATLAS and CMS experiments.
There are different measurement types depending on the experiment. The LHC data at 7 TeV and 8 TeV are released in combined results for the mass [68] and

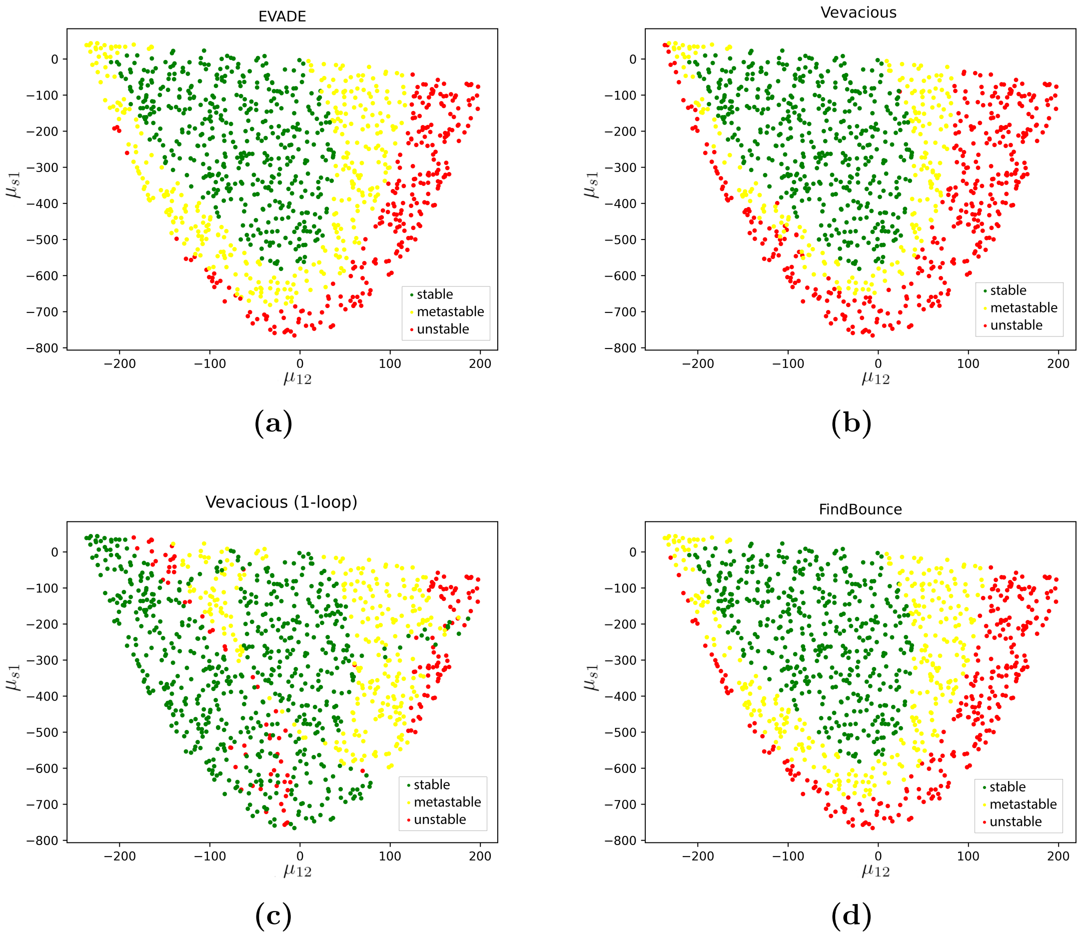

Figure 6: Vacuum stability regions in the 2HDMS in the plane of the trillinear couplings μ_{12} and μ_{S1} calculated with `EVADE` (a), `Vevacious` (b), `Vevacious` (c) at 1-loop level and `FindBounce` (d). For the green region, the EW vacuum is the global minimum. Yellow regions are sufficiently metastable, i.e. the lifetime is longer than the age of the universe and red points are short-lived. While `Vevacious` at 1-loop level suffers from numerical instabilities, the bounce action calculation with a straight path approximation used in `EVADE` and is in good agreement with the path deformation approach used in `Vevacious` at tree level and `FindBounce`.

signal rates [69]. The newer results from 13 TeV data are given in the simplified template cross sections (STXS) [70] framework by ATLAS and CMS with collected data of $\sim 137\text{fb}^{-1}$. These types of measurements correspond to the peak-centered observables, mass-centered observables and STXS measurements in HiggsSignals. With the latest version of `HiggsSignals` which is part of the `HiggsTools` framework the handling of these measurement types has been unified [67]. Further the latest version of `HiggsSignals` includes measurements that are not simple signal rate

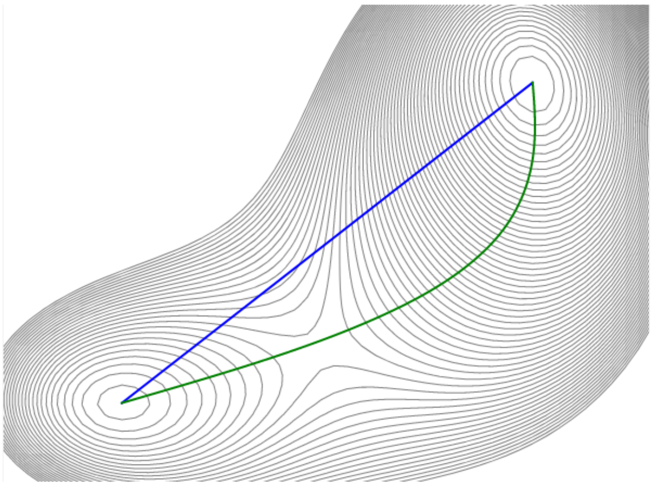

Figure 7: Two local minima of a two/dimensional scalar potential connected by a straight (blue) and correct (green) bounce path. Taken from [51, 60].

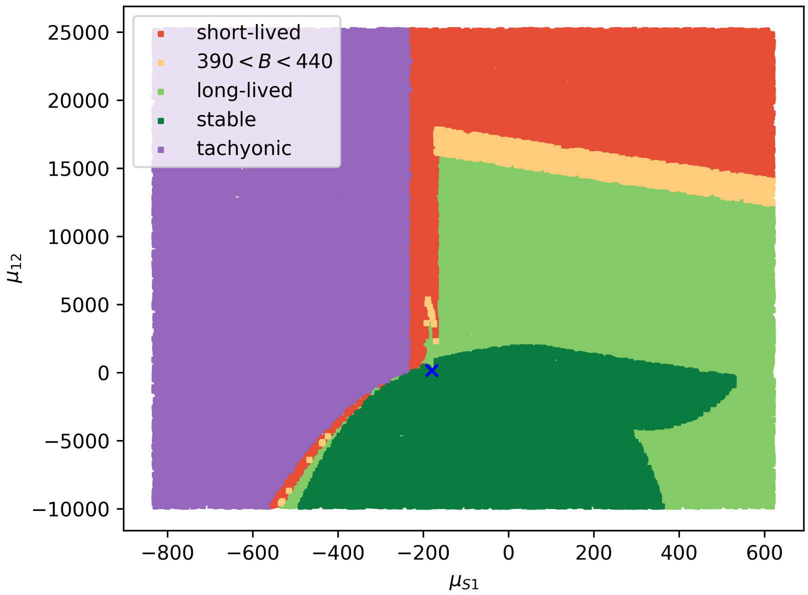

Figure 8: Vacuum stability calculated with `EVADE` for the best fit point in the 2HDMS from Tab. 8. The dark (light) green area depicts points that are absolutely stable and long-lived respectively. Points in the yellow area are in the uncertainty threshold for $390 < B < 440$ and red points are short lived. The points in purple are tachyonic (unphysical) states.

measurements but can also depend on other model parameters. An example is the recent CMS $H \to \tau^+\tau^- - \mathcal{CP}$ analysis [71] which measures the $\mathcal{CP}$ structure of the tau-Yukawa coupling and depends on the c_τ and $c_{\tilde{\tau}}$ coefficients of the CP-even and

CP-odd tau-Yukawa coupling with respect to the SM.
In our analysis we use the reduced χ^2 to judge the validity of our generated points, which is defined as

$$\chi^2_{\text{red}} = \frac{\chi^2_{\text{HS}}}{n_{\text{obs}}}. \tag{4.31}$$

Here χ^2 is evaluated by `HiggsSignals` and $n_{\text{obs}} = 111$ is the considered number of experimental measurements. The are other different ways of interpreting the χ^2 value to judge the validity of a parameter point. One can calculate the likelihood ratio test in the gaussian approximation as

$$\Delta\chi^2 = \chi^2_{Model} - \chi^2_{SM}. \tag{4.32}$$

One benefit is that the effects of the number of observables cancels in this normalisation and $\Delta\chi^2$ directly compares to the SM. $\Delta\chi^2$ describes the best-fit region of the model parameter space. For a confidence level of 2σ this leads to a region of

$$\Delta\chi^2 < 6.18. \tag{4.33}$$

4.2.2 Searches for Additional Higgs Bosons

The currently running ATLAS and CMS experiments at the LHC and earlier experiments at the Tevatron and LEP colliders have made searches for additional BSM scalar particles in various decay channels. It is necessary to ensure that the model parameter space used for phenomenological studies is not already excluded by one of the many searches available. Doing this by hand for each search individually would be very time consuming and unpractical. For this reason the code `HiggsBounds` [63–66] was developed, which is now, with its latest version, a part of `HiggsTools` [67]. The code checks whether a considered parameter point is allowed, by comparing the theory predictions for all Higgs production processes and decay rates to existing searches. Using the narrow width approximation it calculates signal rates from the supplied cross sections and branching ratios and compares with the corresponding limit.
The experimental results give expected and observed limits at 2σ or 95% confidence level as a function of one or more model parameters. This is typically the mass of an additional BSM scalar particle. This is shown for an examplary search in Fig. 10.

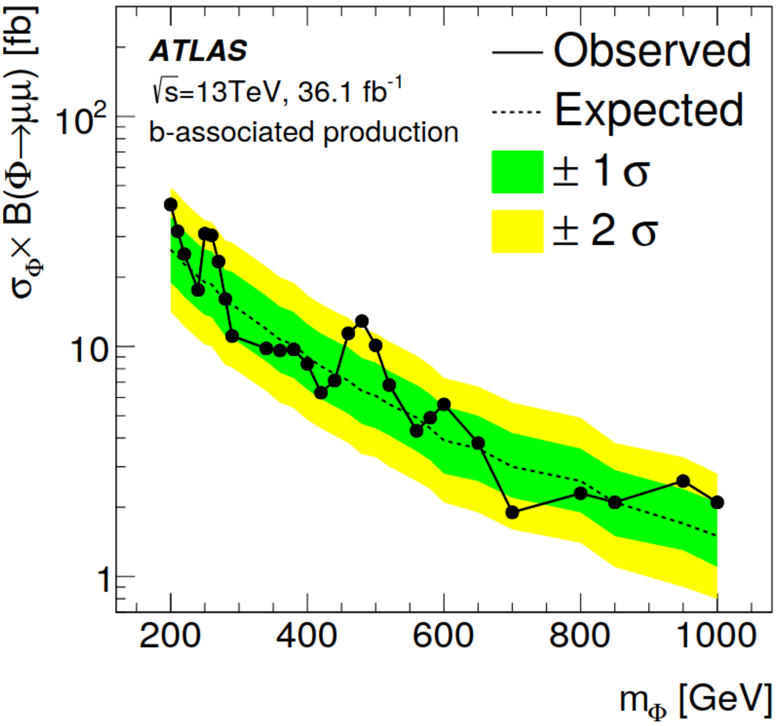

Figure 9: Examplary result of a search for an additional Higgs boson Φ with mass m_Φ. The limit is given at the 95% confidence level on the production cross section $gg \to \Phi$ times its branching ratio to $\mu\bar{\mu}$. The results is taken from the ATLAS collaboration [73].

`HiggsBounds` uses the expected limits (dashed black line and confidence interval in color) to first select the most sensitive experimental search for each scalar in the model. For such searches, the observed limit (solid black line) is applied. If the observed ratio r_{obs} of one of the scalars is greater than 1, the parameter point is considered as excluded by the search.

Concerning our study of a light Higgs boson in the N2HDM and 2HDMS, some important searches are the direct searches for charged Higgs production $pp \to H^\pm tb$ with the decay modes $H^\pm \to \tau\nu$ and $H^\pm \to tb$ [72]. The constrained regions mostly lie in the low $\tan\beta \lesssim 2$ region, due to the enhanced coupling to top quarks. Searches at LEP for charged Higgs bosons are mostly irrelevant as we focus on $\tan\beta = \{1, 20\}$ and light charged Higgs boson masses are excluded from flavor physics observables (see below). Direct searches for additional neutral Higgs bosons become relevant when the heavy scalar Higgs boson h_3 or the heavy pseudo-scalar Higgs bosons a_1, a_2 are not too heavy to be decoupled from lighter particles.

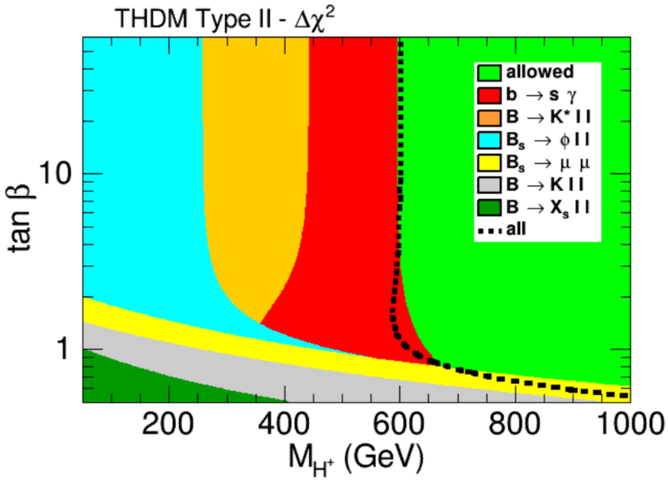

Figure 10: Constraints from flavor physics in the type II 2HDM in the plane of the charged Higgs mass $m_{H^\pm}$ and tanβ. The figure was taken from ref. [75].

4.2.3 Constraints from Flavor Physics

In Sect. 3.1 it was discussed that the introduction of a $\mathbb{Z}_2$-symmetry suppresses the occurrence of FCNCs at tree level. However, FCNC processes may still be introduced by BSM particles through loop effects. In 2HDMs effects from flavor physics mostly constrain the charged Higgs bosons $H^\pm$ in low-energy observables like B-meson decays. Since most constraints from flavor physics are expected to be independent from the presence of additional singlet fields [74], the constraints, which were evaluated in the different 2HDM types, can be applied for the N2HDM and 2HDMS. For the tanβ $= \{1, 20\}$ region we are interested in, the most important bounds according to [75] come from BR($B_s \to X_s\gamma$), constraints on ΔM_{B_s} from neutral B-meson mixing and from BR($B_s \to \mu^+\mu^-$). The dominant contributions to these bounds come from charged Higgs $H^\pm$ [76–78] and top quarks [79, 80]. As those bounds are independent from the neutral scalar sector to a good approximation we can take over the bounds directly from the 2HDM. The constraints from ΔM_{B_s} and BR($B_s \to \mu^+\mu^-$) are dominant for tan$\beta \simeq 1$ while the constraint from BR($B_s \to X_s\gamma$) is present for the whole range of tanβ that we study. Taking all this into account for our study in the type II 2HDMS and N2HDM, these constraints give a lower limit of the charged Higgs mass of $m_{H^\pm} \gtrsim 650$ GeV [75].

4.2.4 Electroweak Precision Observables

The oblique parameters S, T and U were introduced by Peskin and Takeuchi [81] in order to study one-loop corrections of BSM physics to EW precision observables relative to those of the SM. These variables are a parametrization for the W mass m_W and several Z-pole observables. Especially

$$T \propto \rho - 1 \tag{4.34}$$

gives the deviation of the ρ parameter from it's tree-level value of one. The current experimental value is given by $\rho = 1.00038 \pm 0.0002$ [22] and it is defined as

$$\rho = \frac{m_W^2}{m_Z^2 cos^2\theta_W}. \tag{4.35}$$

The parameters S, T and U are defined by

$$\alpha(m_Z)T = \frac{\Pi_{WW}(0)}{m_W^2} - \frac{\Pi_{ZZ}(0)}{m_Z^2}\ , \tag{4.36}$$

$$\frac{\alpha(m_Z)}{4s_W^2c_W^2}S = \frac{\Pi_{ZZ}(m_Z^2) - \Pi_{ZZ}(0)}{m_Z^2} - \frac{c_W^2 - s_W^2}{s_W c_W}\frac{\Pi_{Z\gamma}(m_Z^2)}{m_Z^2} - \frac{\Pi_{\gamma\gamma}(m_Z^2)}{m_Z^2}\ , \tag{4.37}$$

$$\frac{\alpha(m_Z)}{4s_W^2}(S+U) = \frac{\Pi_{WW}(m_W^2) - \Pi_{WW}(0)}{m_W^2} - \frac{c_W}{s_W}\frac{\Pi_{Z\gamma}(m_Z^2)}{m_Z^2} - \frac{\Pi_{\gamma\gamma}(m_Z^2)}{m_Z^2}\ , \tag{4.38}$$

where the Π_{ij} are the one loop self energies. These oblique parameters have experimental values that can be obtained from a global fit to EW precision measurements. In this work we use the results given in [82]

$$S = 0.04 \pm 0.11,\ T = 0.09 \pm 0.14,\ U = -0.02 \pm 0.11. \tag{4.39}$$

In [83, 84] predictions for these oblique parameters have been calculated for a variety of BSM models with an arbitary number of $SU(2)_L$ doublets and singlets. We use these results to calculate theory predictions and compare these to the fit results in eq. 4.39. We calculate a χ^2 and perform a cut at $\chi^2 < 7.81$ which corresponds to a 2σ limit in the plane of S,T and U. For the parametrization of BSM effects through the oblique parameters, the new particles have to be sufficiently heavy to avoid on-shell effects in the self-energy diagrams.

The oblique parameters directly constrain the possible mass values of additional particles in BSM theories. The parameter T constraints the upper bound on the mass difference between the charged scalars and the closest in mass neutral scalar coming from additional doublets. The parameter S constrains the mass difference between sufficiently mixed scalars. The parameter T is the most relevant in the scenarios we discuss. However, the strong correlation between S, T and U can lead to stronger constraints when all three are considered.

We now discuss the calculation of the oblique parameters in the 2HDMS explicitly. We follow the procedure in [85]. In the full expressions for S, T and U in [85] appear parts of the $n \times n$ unitary matrix $\tilde{\mathcal{U}}$ and the $m \times m$ orthogonal matrix $\tilde{\mathcal{V}}$. These are the diagonalizing matrices for the mass-squared matrices of the charged and neutral scalars. We have $n = n_d + n_c$ where n_d and n_c are the number of scalar $SU(2)$ doublets and complex scalar $SU(2)$ singlets, respectively. Similarly, we have $m = 2n_d + n_n$ where n_n is the number of real scalar $SU(2)$ singlets.

They are given by

$$\tilde{\mathcal{U}} = \begin{pmatrix} \mathcal{U} \\ \mathcal{T} \end{pmatrix}, \qquad \tilde{\mathcal{V}} = \begin{pmatrix} \mathrm{Re}\mathcal{V} \\ \mathrm{Im}\mathcal{V} \\ \mathcal{R} \end{pmatrix}. \tag{4.40}$$

The matrices $\mathcal{U}$ and $\mathcal{V}$, appearing in the expressions for S, T and U, are $n_d \times n$ and $n_d \times m$ dimensional, respectively. The matrix $\mathcal{V}$ can be constructed from the matrices Eq. 3.23 and Eq. 3.38 for the neutral scalars and the matrix $\mathcal{U}$ from the diagonalizing matrix of the charged sector. This gives the matrices

$$U = \begin{pmatrix} c_b & s_b \\ -s_b & c_b \end{pmatrix}, \tag{4.41}$$

$$V = \begin{pmatrix} R^A_{13} & R^A_{23} \\ iR^A_{11} & iR^A_{21} \\ iR^A_{12} & iR^A_{22} \\ R_{11} & R_{21} \\ R_{12} & R_{22} \\ R_{13} & R_{23} \end{pmatrix} = \begin{pmatrix} c_b & s_b \\ -is_b c_{\alpha_4} & ic_b c_{\alpha_4} \\ is_b s_{\alpha_4} & -ic_b s_{\alpha_4} \\ c_{\alpha_1} c_{\alpha_2} & s_{\alpha_1} c_{\alpha_2} \\ -s_{\alpha_1} c_{\alpha_3} - c_{\alpha_1} s_{\alpha_2} s_{\alpha_3} & c_{\alpha_1} c_{\alpha_3} - s_{\alpha_1} s_{\alpha_2} s_{\alpha_3} \\ s_{\alpha_1} s_{\alpha_3} - c_{\alpha_1} s_{\alpha_2} c_{\alpha_3} & -s_{\alpha_1} s_{\alpha_2} c_{\alpha_3} - c_{\alpha_1} s_{\alpha_3} \end{pmatrix}. \tag{4.42}$$

With these matrices the full calculation of the S, T and U parameters can be carried out, following [85].

Part III

A light Higgs Boson in Singlet Extensions of the Two Higgs Doublet Model

5 A light Higgs Boson in Singlet Extensions of the 2HDM

This section is based on the publication [6]. We discuss a local 2.3σ local excess discovered at LEP in the $e^+e^- \to ZH(H \to b\bar{b})$ channel [5], consistent with a scalar of mass 96 GeV. Due to the $b\bar{b}$ final state the mass resolution is rather large. ATLAS and CMS searched for light Higgs bosons in the diphoton final state. The CMS Run II results [4] show a local excess of $\sim 3\sigma$ at 96 GeV, where a similar excess of 2σ had been observed in Run I [86] at roughly the same mass.

Before the start of the LHC, searches for Higgs bosons below 125 GeV have been performed at LEP [5, 87, 88] and Tevatron [89]. Since the discovery of a Higgs boson by the ATLAS and CMS collaboration in 2012, there were further searches for a light Higgs boson performed at LHC [4, 90–92].

First Run II results from ATLAS, on the other hand, using $80\,\mathrm{fb}^{-1}$ turned out to be weaker than the corresponding CMS results, see, e.g., Fig. 1 in Ref. [93].

The excesses found by LEP and CMS were effectively at the same mass. This leads to the question if both excesses have a common origin. We interpret them as a light scalar Higgs boson at as mass of ~ 96 GeV. The goal is to accomodate both excesses simultaneously in a model, while still being in agreement with all other Higgs boson related measurements and searches. The excesses have already bin described in:

(i) the Next-to-Two Higgs doublet model, N2HDM [41–45, 94], as will be discussed below,

(ii) various realizations of the Next-to-Minimal supersymmetric SM, NMSSM [94–96],

(iii) the μ-from-ν supersymmetric SM ($\mu\nu$SSM) with one [97] and three generations [98] of right-handed neutrinos

(iv) Higgs inflation inspired μNMSSM [99],

(v) NMSSM with a seesaw extension [100],

(vi) Higgs singlet with additional vector-like matter, as well as two Higgs doublet model, 2HDM type I [101],

(vii) 2HDM type I with a moderately-to-strongly fermiophobic $\mathcal{CP}$-even Higgs [102],

(viii) radion model [103] ,

(ix) Higgs associated with the breakdown of an $U(1)_{L_\mu L_\tau}$ symmetry [104],

(x) minimal dilaton model [105],

(xi) composite framework containing a pseudo-Nambu Goldstone-type light scalar [106],

(xii) SM extended by a complex singlet scalar field (which can also accommodate a pseudo-Nambu Goldstone dark matter) [107],

(xiii) anomaly-free $U(1)'$ extensions of SM with two complex scalar singlets [108].

Having different models being able to accomodate the two excesses lets the question arise how one can distinguish the various model realizations, especially if they are very similar to each other. In this work we take a first step towards this by accomodating the two excesses both in the N2HDM and in the 2HDMS which have a very similar parameter space. We analyze which part of the parameter space is suitable for describing the two excesses and investigate possible ways to distinguish both model realizations.

For the analyses of the 2HDMS and the N2HDM Higgs-boson sectors at future colliders we employ the anticipated reach and precision of the HL-LHC, as well as a possible future e^+e^- collider, where we focus on the International Linear Collider (ILC) with a center-of-mass energy of $\sqrt{s} = 250$ GeV (ILC250). In particular we show what can be learned from a measurement of the couplings of the 125 GeV Higgs boson at the ILC250. Going one step further, we present for the first time a phenomenological analysis of the new state at ~ 96 GeV at the ILC250: we analyze to which precision its couplings can be measured at the ILC250 and what can be learned from these future measurements about the underlying model. We include all relevant technical and phenomenological details for such a coupling measurement of a light Higgs boson at the ILC250.

5.1 The Experimental Excesses

The experimental excesses at both LEP and CMS could be translated into the following signal strengths as quoted in [4, 88, 109, 110]:

$$\mu^{\text{exp}}_{\text{LEP}} = \frac{\sigma^{\text{exp}}(e^+e^- \to Z\phi \to Zb\bar{b})}{\sigma^{\text{SM}}(e^+e^- \to ZH^0_{\text{SM}} \to Zb\bar{b})} = 0.117 \pm 0.05 \quad , \tag{5.1}$$

$$\mu^{\text{exp}}_{\text{CMS}} = \frac{\sigma^{\text{exp}}(pp \to \phi \to \gamma\gamma)}{\sigma^{\text{SM}}(pp \to H^0_{\text{SM}} \to \gamma\gamma)} = 0.6 \pm 0.2 \quad , \tag{5.2}$$

where the H^0_{SM} is the SM Higgs boson with the rescaled mass at the same range as the unknown scalar particle ϕ.

For our analysis we interpret the experimental excess at ~ 96 GeV as the lightest scalar Higgs boson h_1, and we identify the second lightest scalar Higgs h_2 as the SM-like Higgs at ~ 125 GeV.

Furthermore, the elements of the rotation matrix, i.e. $|R_{ij}|^2$, represent each field admixtures of the corresponding physical states. The matrix elements thus determine the Higgs-boson couplings to the SM particles. Here we define the reduced coupling as the ratio between the 2HDMS/N2HDM Higgs coupling and the corresponding SM-Higgs coupling:

$$c_{h_i ff} = \frac{g_{h_i ff}}{g_{H_{\text{SM}} ff}} \ . \tag{5.3}$$

The reduced Higgs to fermion couplings for all four Yukawa types are summarized in Tab. 5.

	Type I	Type II	Lepton specific	Flipped
$c_{h_i tt}$	$\frac{R_{i2}}{\sin\beta}$	$\frac{R_{i2}}{\sin\beta}$	$\frac{R_{i2}}{\sin\beta}$	$\frac{R_{i2}}{\sin\beta}$
$c_{h_i bb}$	$\frac{R_{i2}}{\sin\beta}$	$\frac{R_{i1}}{\cos\beta}$	$\frac{R_{i2}}{\sin\beta}$	$\frac{R_{i1}}{\cos\beta}$
$c_{h_i \tau\tau}$	$\frac{R_{i2}}{\sin\beta}$	$\frac{R_{i1}}{\cos\beta}$	$\frac{R_{i1}}{\cos\beta}$	$\frac{R_{i2}}{\sin\beta}$

Table 5: Higgs to fermion reduced couplings for different types of Yukawa couplings

One can also derive the reduced Higgs to gauge-bosons couplings,

$$c_{h_i VV} = c_{h_i ZZ} = c_{h_i WW} = \cos\beta R_{i1} + \sin\beta R_{i2} \, . \tag{5.4}$$

Since one of the most important targets of our analysis is the interpretation of the experimental excess in the 2HDMS/N2HDM, we interpreted the scalar ϕ as the lightest $\mathcal{CP}$-even Higgs boson h_1 of the 2HDMS/N2HDM, and we evaluated such signal strengths for all the h_1. These signal strengths can be calculated by the following expressions in the narrow width approximation [41] (introduced here for the 2HDMS):

$$\mu^{\text{the}}_{\text{LEP}} = \frac{\sigma_{\text{2HDMS}}(e^+e^- \to Zh_1)}{\sigma_{\text{SM}}(e^+e^- \to ZH^0_{\text{SM}})} \times \frac{\text{BR}_{\text{2HDMS}}(h_1 \to b\bar{b})}{\text{BR}_{\text{SM}}(H^0_{\text{SM}} \to b\bar{b})} = |c_{h_1VV}|^2 \frac{\text{BR}_{\text{2HDMS}}(h_1 \to b\bar{b})}{\text{BR}_{\text{SM}}(H^0_{\text{SM}} \to b\bar{b})} \quad , \tag{5.5}$$

$$\mu^{\text{the}}_{\text{CMS}} = \frac{\sigma_{\text{2HDMS}}(gg \to h_1)}{\sigma_{\text{SM}}(gg \to H^0_{\text{SM}})} \times \frac{\text{BR}_{\text{2HDMS}}(h_1 \to \gamma\gamma)}{\text{BR}_{\text{SM}}(H^0_{\text{SM}} \to \gamma\gamma)} = |c_{h_1tt}|^2 \frac{\text{BR}_{\text{2HDMS}}(h_1 \to \gamma\gamma)}{\text{BR}_{\text{SM}}(H^0_{\text{SM}} \to \gamma\gamma)} \quad . \tag{5.6}$$

The effective couplings of c_{h_1VV} and c_{h_1tt} can be easily obtained from Eq. (5.4) and Tab. 5, while the corresponding branching ratios have been obtained with `SPheno-4.0.4` [111, 112].

The overall χ^2 corresponding to the excesses is calculated as

$$\chi^2_{\text{CMS-LEP}} = \left(\frac{\mu^{\text{the}}_{\text{LEP}} - 0.117}{0.057}\right)^2 + \left(\frac{\mu^{\text{the}}_{\text{CMS}} - 0.6}{0.2}\right)^2 \, . \tag{5.7}$$

The total χ^2 is defined as

$$\chi^2_{\text{tot}} = \chi^2_{\text{CMS-LEP}} + \chi^2_{\text{HS}} \, . \tag{5.8}$$

The points of the 2HDMS/N2HDM with the lowest χ^2_{tot} are the respective "best-fit" points in the two models.

In order to understand the effect of mixing angles on the signal strengths of the excesses, one can focus on the couplings of h_1 derived from Eq. (3.23) and Tab. 5, which are given by

$$c_{h_1tt} = \frac{\sin\alpha_1 \cos\alpha_2}{\sin\beta}, \qquad c_{h_1bb} = \frac{\cos\alpha_1 \cos\alpha_2}{\cos\beta}, \qquad c_{h_1VV} = \cos\alpha_2 \cos(\beta - \alpha_1). \tag{5.9}$$

If h_1 is the pure gauge singlet (i.e. $\cos\alpha_2 = 0$), all three couplings in Eq. (5.9), which are proportional to the $\cos\alpha_2$, would be zero. However, h_1 would then be completely invisible and could not produce any experimental excesses in this case. Therefore, in order to cover the ranges of the experimental excesses efficiently, we enforced the singlet component of h_1 to be smaller than 95% (i.e. $\cos^2\alpha_2 > 5\%$), which essentially yields non-vanishing couplings of h_1 to SM particles. As a result, the interval of α_2 is constrained by this requirement. We have checked explicitly that this constraint does not exclude any valid parameter point in our analysis.

For the signal strength of CMS, the coupling c_{h_1tt} and the $\mathrm{BR}(h_1 \to \gamma\gamma)$ play the dominant roles. Since the decay width of the h_1 is dominated by the decay to $b\bar{b}$, a smaller c_{h_1bb} would suppress the decay width of $h_1 \to b\bar{b}$ and lead to the enhancement of $\mathrm{BR}(h_1 \to \gamma\gamma)$. Consequently, $\mathrm{BR}(h_1 \to \gamma\gamma)$ can be anti-proportional to the coupling $|c_{h_1bb}|^2$. Since μ_{CMS} is also proportional to the $|c_{h_1tt}|^2$, one obtains the approximate relation for μ_{CMS} which is given by, see Eq. (5.6),

$$\mu^{\mathrm{the}}_{\mathrm{CMS}} \propto \frac{|c_{h_1tt}|^2}{|c_{h_1bb}|^2} = \left(\frac{\tan\alpha_1}{\tan\beta}\right)^2 . \tag{5.10}$$

As we see in Eq. (5.10), $\mu^{\mathrm{the}}_{\mathrm{CMS}}$ can be directly enhanced by the increment of α_1. In order to have a not too suppressed signal strength for the CMS excess, $\tan\alpha_1 > \tan\beta$ is required. However, the combination $\frac{\tan\alpha_1}{\tan\beta}$ can be arbitrarily large during the scan. Thus we scan the inverse of this combination in the range from 0 to 1, see the next subsection.

5.2 The Parameter Scan

Following the N2HDM interpretation of the excesses [41], we also focus on the type-II Yukawa structure for the 2HDMS. However, we will investigate a larger $\tan\beta$ region as it was done in Ref. [41].

In order to investigate the parameter space of the 2HDMS/N2HDM that gives rise to a description of the 96 GeV excesses, we performed an extensive scan of the parameter spaces by using the spectrum generator `SPheno-4.0.4` [111, 112], where the model implementations are generated by the public code `SARAH-4.14.3` [113]. During the scan, we fix the mass $m_{h_2} = 125.09$ GeV and enforce the mixing angles to be close to the alignment limit as explained in detail in Sect. 3.2.3. As discussed above, by employing `HiggsSignal-2.6.1`, we can ensure that the h_2 is in agreement with the LHC measurements. Concerning the exclusion bounds from flavor physics as we mentioned in Sect. 4.2, we simply apply the conservative limits given by $\tan\beta > 1$

and $m_{H^\pm} > 800$ GeV, which is above the experimental limit of 650 GeV [75].

Studying a higher region of $\tan\beta$ with different ranges for the heavy Higgs boson masses, from 1 to 20 (i. e. going beyond the region explored in Ref. [41]) raises the lower bound of the heavy Higgs boson masses m_{h_3} and m_{a_2} coming from the constraints on heavy Higgs bosons from searches for $H/A \to \tau^+\tau^-$ at the LHC [114]. We scan two intervals of $\tan\beta$ with different ranges for the heavy Higgs boson masses, see Tab. 7. Concerning unitarity constraints, the S, T, U parameters and the mass difference between the heavy Higgs states has to be small. Therefore $m_{H^\pm}$ is scanned in the interval given in Tab. 7 and the other two are scanned around this mass with a Gaussian distribution (with a width of 200 GeV or 50 GeV for the low and high $\tan\beta$ region, respectively).

In the case of the 2HDMS we have an additional lighter $\mathcal{CP}$-odd Higgs boson a_1, see Sect. 3.2.4. For $\alpha_4 < \frac{\pi}{4}$ the heavier a_2 would be singlet-like. This scenario is more likely to be excluded by vacuum stability constraints and we leave this for future studies. Therefore we choose $\frac{\pi}{4} < \alpha_4 < \frac{\pi}{2}$, which makes the lighter a_1 singlet-like. We choose $m_{h_2} < m_{a_1}$ which leads to a scan range of m_{a_1} from 200 GeV to 500 GeV to also fulfill $m_{a_1} < m_{a_2}$. Overall, the scan intervals for all the particles are given by:

m_{h_1}	$\{95,\ 98\}$ GeV
m_{h_2}	125.09 GeV
m_{a_1}	$\{200,\ 500\}$ GeV
η	$\{0.98, 1\}$
α_4	$\{\frac{\pi}{4},\ \frac{\pi}{2}\}$
v_S	$\{100,\ 2000\}$ GeV
$\frac{\tan\beta}{\tan\alpha_1}$	$\{0, 1\}$
α_2	$\pm\{0.95,\ 1.3\}$

Table 6: Scan intervals

$\tan\beta$	$m_{h_3} \sim m_{a_2} \sim m_{H^\pm}$
1 - 10	$\{800,\ 1200\}$ GeV
10 - 20	$\{1000,\ 1700\}$ GeV

Table 7: Heavy Higgs boson mass scan intervals for different $\tan\beta$ regions.

We have checked explicitly that the constraints on $\sin(\beta - (\alpha_1 + \mathrm{sgn}(\alpha_2)\alpha 3))$ and α_2 do not exclude any valid point of our parameter space.

5.3 Preferred Parameter Spaces

In this section we will discuss the preferred parameter spaces in the 2HDMS and N2HDM. This study was never carried out in the 2HDMS and will be discussed in detail. The N2HDM application was already discussed in [41] and redone with our scan setup for consistency. The results going beyond the analysis in [41] will be discussed.

5.3.1 2HDMS

The results of the 2HDMS scan in the low $\tan\beta$ region are shown in Fig. 11 in the μ_{CMS}-μ_{LEP} plane, where the color code indicates χ^2_{red}, see Eq. (4.31). The red ellipse corresponds to the 1σ ellipse, with the best-fit point (see below) marked by a red cross.

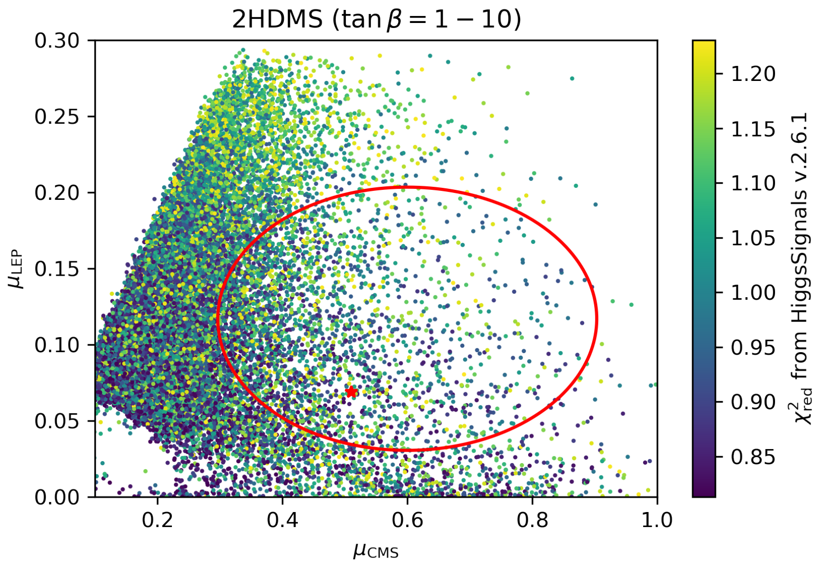

Figure 11: The signal strengths of both excesses μ_{CMS} and μ_{LEP} for the 2HDMS scan points with $\tan\beta \in \{1,\ 10\}$. The red ellipse shows the $1\,\sigma$ region of the excesses with the red star as the best-fit point. The color code indicates the χ^2_{red} and the lowest χ^2_{red} in the $1\,\sigma$ ellipse is about 0.821.

As can be seen in Fig. 11 the 1σ ellipse of μ_{CMS} and μ_{LEP} can be fully covered by the 2HDMS parameter space, while all the points in the figure have $\chi^2_{\mathrm{red}} < 1.3$. The lowest χ^2_{red} in the 1σ ellipse is about 0.821. Therefore, the 96 GeV excesses can be easily accommodated while the h_2 at ~ 125 GeV is in good agreement with the experimental measurements. The best-fit point, defined via Eq. (5.8), is marked with a red cross and lies well within the 1σ ellipse. Phenomenological details of this best-fit point can be found in Tab. 8.

Best fit point in $\tan\beta \in \{1,\ 10\}$					
m_{h_1}	m_{h_2}	m_{h_3}	m_{a_1}	m_{a_2}	$m_{H^\pm}$
96.438 GeV	125.09 GeV	784.08 GeV	413.46 GeV	660.07 GeV	808.93 GeV
$\tan\beta$	α_1	α_2	α_3	α_4	v_s
1.3393	1.3196	-1.1687	-1.2575	1.4719	653.84 GeV
Branching ratios					
$h_1 \to b\bar{b}$	$h_1 \to gg$	$h_1 \to \tau^+\tau^-$	$h_1 \to \gamma\gamma$	$h_1 \to W^{+*}W^{-*}$	$h_1 \to Z^*Z^*$
42.2%	35.3%	4.61%	0.317%	0.739%	$< 0.1\%$
$h_2 \to b\bar{b}$	$h_2 \to gg$	$h_2 \to \tau^+\tau^-$	$h_2 \to \gamma\gamma$	$h_2 \to W^{+*}W^{-*}$	$h_2 \to Z^*Z^*$
53.9%	10.5%	6.17%	0.249%	23.4%	2.54%
$h_3 \to b\bar{b}$	$h_3 \to t\bar{t}$	$h_3 \to h_2h_2$	$h_3 \to h_1h_2$	$h_3 \to h_1h_1$	$h_3 \to W^+W^-$
$< 0.1\%$	65.3%	5.26%	7.76%	0.158%	8.26%
$a_1 \to t\bar{t}$	$a_1 \to \tau^+\tau^-$	$a_2 \to t\bar{t}$	$a_2 \to \tau^+\tau^-$	$H^\pm \to tb$	$H^\pm \to W^\pm h_2$
95%	$< 0.1\%$	88.2%	$< 0.1\%$	73.7%	1.12%

Table 8: Parameters and relevant branching ratios of the best-fit point in the 2HDMS in the $\tan\beta \in \{1,\ 10\}$ region.

Best fit point in $\tan\beta \in \{10,\ 20\}$					
m_{h_1}	m_{h_2}	m_{h_3}	m_{a_1}	m_{a_2}	$m_{H^\pm}$
96.013 GeV	125.09 GeV	1437.8 GeV	323.4 GeV	1438.5 GeV	1499.6 GeV
$\tan\beta$	α_1	α_2	α_3	α_4	v_s
13.783	1.5441	1.2162	1.5338	1.5679	1212.6 GeV
Branching ratios					
$h_1 \to b\bar{b}$	$h_1 \to gg$	$h_1 \to \tau^+\tau^-$	$h_1 \to \gamma\gamma$	$h_1 \to W^{+*}W^{-*}$	$h_1 \to Z^*Z^*$
45.1%	32.5%	4.93%	0.612%	1.04%	$< 0.1\%$
$h_2 \to b\bar{b}$	$h_2 \to gg$	$h_2 \to \tau^+\tau^-$	$h_2 \to \gamma\gamma$	$h_2 \to W^{+*}W^{-*}$	$h_2 \to Z^*Z^*$
53.7%	10.0%	6.14%	0.269%	24.2%	2.62%
$h_3 \to b\bar{b}$	$h_3 \to t\bar{t}$	$h_3 \to h_2h_2$	$h_3 \to h_1h_2$	$h_3 \to h_1h_1$	$h_3 \to W^+W^-$
69.7%	4.82%	3.74%	5.73%	0.585%	2.60%
$a_1 \to b\bar{b}$	$a_1 \to \tau^+\tau^-$	$a_2 \to b\bar{b}$	$a_2 \to \tau^+\tau^-$	$H^\pm \to tb$	$H^\pm \to W^\pm h_2$
88.0%	11.7%	74.2%	12%	91.4%	0.353%

Table 9: Parameters and relevant branching ratios of the best-fit point in the high $\tan\beta$ region.

In Fig. 12 we show the results for $|c_{h_1VV}|^2$ and $|c_{h_1bb}/c_{h_1tt}|^2$, respectively, in the plane of $\mu_{\rm CMS}$ and $\mu_{\rm LEP}$. In Fig. 12, the points with higher signal strength $\mu_{\rm LEP}$

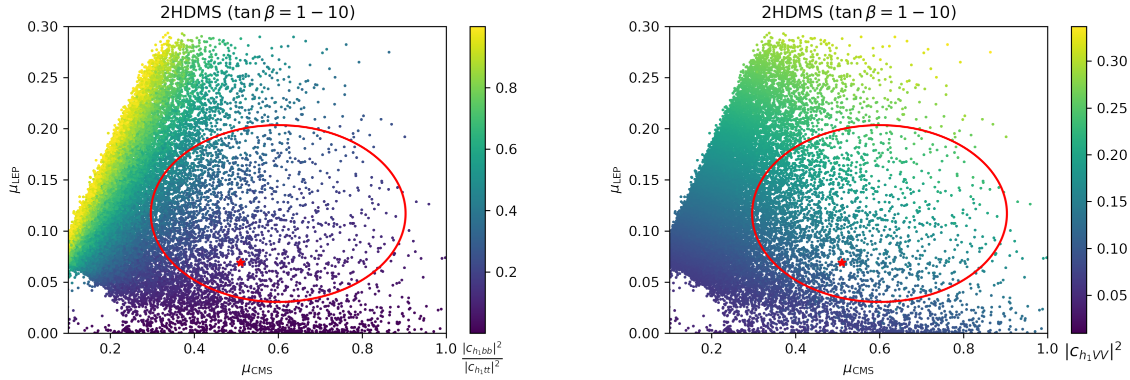

(a) The same plane as in Fig. 11, with the color code indicating the square of the effective coupling of h_1 to gauge bosons. The lowest (highest) value of $|c_{h_1VV}|^2$ in the 1σ ellipse is 0.088 (0.26).

(b) The same plane as in Fig. 11, with the color code indicating the ratio $|c_{h_1bb}|^2/|c_{h_1tt}|^2$. The lowest (highest) value in the 1σ ellipse is 0.039 (0.53).

Figure 12

always have the higher coupling c_{h_1VV}, as $\mu_{\rm LEP}$ is directly proportional to $|c_{h_1VV}|^2$, see Eq. (5.5). On the other hand, one can observe from Fig. 12 that the points with lower values of $|c_{h_1bb}|^2/|c_{h_1tt}|^2$ yield a higher signal strength $\mu_{\rm CMS}$, consistent with the discussion in Sect. 5.1, i.e. $\mu_{\rm CMS}$ is anti-proportional to $|c_{h_1bb}|^2/|c_{h_1tt}|^2$. However, a lower c_{h_1bb} coupling would slightly suppress BR($h_1 \to b\bar{b}$) leading to the lower $\mu_{\rm LEP}$, and therefore the distribution is slightly oblique in the plane of $\mu_{\rm CMS}$ and $\mu_{\rm LEP}$. The best-fit point marked by the red cross has $|c_{h_1VV}|^2 \sim 0.13$ and $|c_{h_1bb}|^2/|c_{h_1tt}|^2 \sim 0.12$.

The results of the high $\tan\beta$ region scan, using the intervals given in Tab. 7, are shown in Fig. 13, where the color coding indicates the $\chi^2_{\rm red}$. It can be observed that also in the high $\tan\beta$ region the 1σ ellipse in the plane of $\mu_{\rm CMS} - \mu_{\rm LEP}$ is well covered by our parameter scan for $\tan\beta$=10–20. The distribution of the $\chi^2_{\rm red}$ is found to be very similar to the low $\tan\beta$ case. Also the other quantities, $|c_{h_1VV}|^2$ and $|c_{h_1bb}|^2/|c_{h_1tt}|^2$ behave as in the low $\tan\beta$ case (and are thus not shown). In the Tab. 9 we summarize the details for best-fit points in the region of $\tan\beta$=10–20. The high $\tan\beta$ best-fit point has $|c_{h_1VV}|^2 \sim 0.12$ and $|c_{h_1bb}/c_{h_1tt}|^2 \sim 0.14$, which is very close to the corresponding numbers of the low $\tan\beta$ best-fit point. Overall we find that the points within the 1σ range of the 96 GeV excesses have no preference for low or high $\tan\beta$. Finally, also for the charged Higgs boson mass we do not find a preferred region (within the intervals given in Tab. 7), neither in the low nor in the

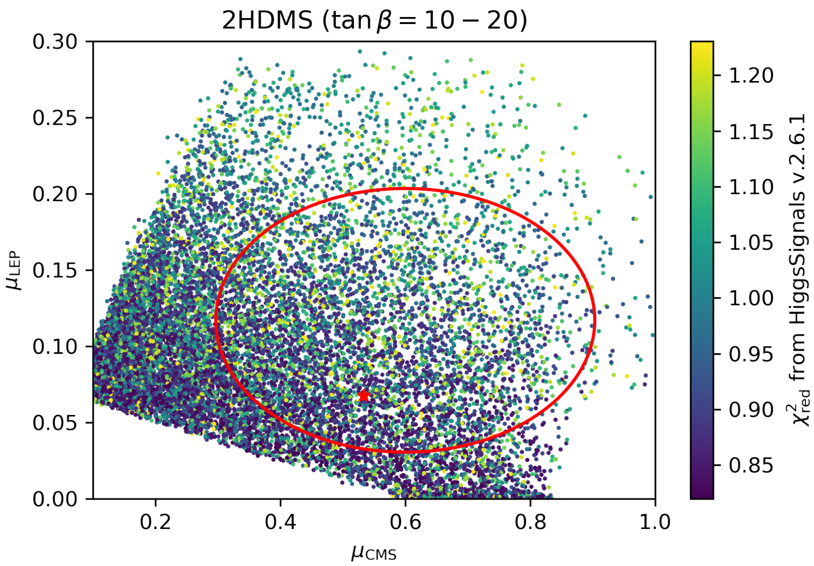

Figure 13: The same plane as in Fig. 11 with $\tan\beta \in \{10, 20\}$, and the color coding indicating the $\chi^2_{\rm red}$.

high $\tan\beta$ analysis.

5.3.2 N2HDM

We now turn to the corresponding analysis in the N2HDM, where earlier results can be found in Refs. [41–45]. In Fig. 14 we show the results of the N2HDM in the $\mu_{\rm CMS}$-$\mu_{\rm LEP}$ plane for the low (left plot) and high $\tan\beta$ range (right plot). One can observe that both the low $\tan\beta$ region and the high $\tan\beta$ region of the N2HDM parameter space can cover the 1σ range of the 96 GeV "excess". This extends the analysis in Ref. [41], where only relatively low $\tan\beta$ values were found. These differences can be traced back to an improved scan strategy as well as improvements in the parameter point generation. The behavior of the other quantities analyzed in the previous subsection is very similar for the N2HDM.

Overall, our comparative analysis of the 2HDMS (which is a new model analysis) and the N2HDM (updating the results of Ref. [41]) shows that the two models can fit equally well the 96 GeV excess. The differences between the two models (see in particular the discussion in Sect. 3, i.e. different symmetries and different particle content) do not impact in a relevant way the description of the excesses. Consequently, other phenomenological investigations will have to be performed to distinguish the two models, see the discussion in Sect. 3.2.4, as well as our analysis

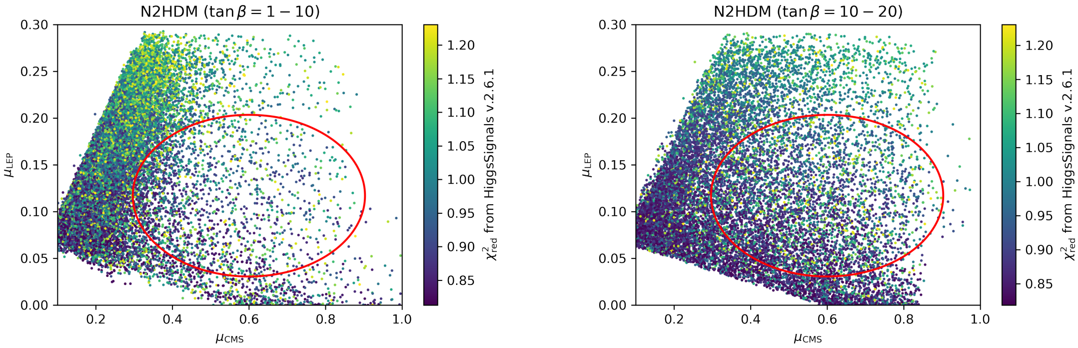

(a) **(b)**

Figure 14: The N2HDM scan results with the same plane as in Fig. 11. The left (right) plot is for $\tan\beta$=1–10 (10–20).

below in Sects. 5.4.1 and 5.4.2.

5.4 Prospects for e^+e^- colliders

The searches for a possible Higgs boson at ~ 96 GeV will continue at ATLAS and CMS. However, it is not expected that such a particle could be seen in other decay modes than $\gamma\gamma$ and possibly $\tau^+\tau^-$. The pp environment makes it difficult to perform precision measurements of such a light Higgs boson. Better suited for such a task would be a future e^+e^- collider such as the planned ILC [41, 44], where the light Higgs is produced in the Higgs-strahlung channel, $e^+e^- \to Z^* \to Zh_1$ [115–117]. The ILC can analyze the scenarios under investigations in two complementary ways. One can search for the new Higgs boson and analyze its properties directly. We also include, for the first time, an analysis of the coupling measurement of the h_1 at the ILC. On the other hand, one can perform precision measurements of the Higgs boson at ~ 125 GeV and look for indirect effects of the extended Higgs boson sector. In this section we will explore both possibilities (where we will emphasize where we go beyond Refs. [41, 44]). In particular, we analyze the 2HDMS and the N2HDM side by side to check for possible differences in their phenomenology.

5.4.1 Precision on coupling measurements

In Fig. 15 we show the plane of m_{h_1} and the quantity $|c_{h_1VV}|^2 \times \mathrm{BR}(h_1 \to b\bar{b})$. The green dashed (blue) line indicates the expected (observed) limits at LEP [5], where the 2σ excess at ~ 96 GeV can be observed. The orange and the red line show the

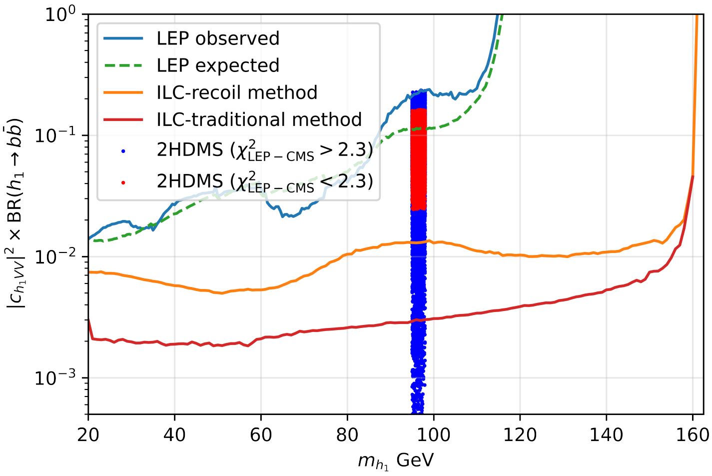

Figure 15: The plane of m_{h_1} and S_{95}, which is defined as $\sigma(e^+e^- \to Zh_1)/\sigma_{\rm SM} \times \mathrm{BR}(h_1 \to b\bar{b})$. The green dashed (blue) line indicate the expected (observed) limits at LEP [5]. The orange and the red line show the reach of the ILC using the "recoil method" or the "traditional method" (see text). The red (blue) points indicate the parameter points within (outside of) the 1σ range of the 96 GeV excesses.

reach of the ILC using the "recoil method" [118] or the "traditional method", see Ref. [115] for details (and Ref. [116] for a corresponding experimental analysis). The "recoil" method is using a Z boson produced by Higgs strahlung which is reconstructed from the $Z \to \mu^+\mu^-$ decay, while the "traditional method" is the analysis using the $H \to b\bar{b}$ channel. This analysis assumed $\sqrt{s} = 250$ GeV and an integrated luminosity of 500 fb^{-1}. The colored dots indicate the results from our parameter scan in the 2HDMS. The red (blue) points correspond to the parameter points inside (outside) the 1σ ellipse of $\mu_{\rm CMS}$ and $\mu_{\rm LEP}$. One can observe that the red points, i.e. the ones describing the two excesses, are all well above the orange line. This shows that such light Higgs boson could be produced abundantly at the ILC. The same conclusion holds for the N2HDM.

In a second step we analyze the anticipated precision of the h_1 coupling measurements that can be performed at the ILC. We would like to stress that this constitutes the first analysis of this type: to which precision the couplings of a BSM Higgs boson can be measured at a future e^+e^- collider (all relevant details of this new analysis can be found in Appendix A, and what are the phenomenological consequences. Concretely, we assume an ILC center-of-mass energy of $\sqrt{s} = 250$ GeV and an integrated luminosity of $2\,\mathrm{ab}^{-1}$. We concentrate on the points within the 1σ ellipse of the 96 GeV excesses in the $\mu_{\rm CMS}$-$\mu_{\rm LEP}$ plane. In Fig. 16 (left) we show the numbers of h_1 events produced in the Higgs-strahlung channel for the dominant decay modes. We directly compare the results for the 2HDMS and the N2HDM for the low and the high $\tan\beta$ region. It can be seen that no relevant differences can be observed, neither between the two models nor for the two $\tan\beta$ regions. It is remarkable that, depending on the channel between $\sim 10^3$ and up to 10^5 events can be expected. The statistical uncertainty for these numbers is shown in the right plot of Fig. 16.

In the left plot of Fig. 17 we show the predictions for the effective couplings, which are the same for c_{h_1bb} and $c_{h_1\tau\tau}$, as well as for c_{h_1ZZ} and c_{h_1WW}. The only visible difference between the low and high $\tan\beta$ region is the somewhat enlarged range of c_{h_1tt}, which is found in the low $\tan\beta$ region. Naively, one would expect a corresponding enhancement in the number of gg events in the left plot of Fig. 16. However, the corresponding branching ratio is largely driven by the decay $h_1 \to b\bar{b}$, and no direct correspondence of c_{h_1tt} and $\mathrm{BR}(h_1 \to gg)$ is found (see also the numbers for the best-fit points in Tabs. 8 and 9). Finally in the right plot of Fig. 17 we show a completely new type of analysis: the anticipated precision for the h_1 coupling measurement at the ILC (details about this evaluation are given in Appendix A. The coupling of the h_1 to $b\bar{b}$, $\tau^+\tau^-$, gg, and W^+W^- are determined from the respective decays, whereas the coupling to ZZ is determined from the Higgs-strahlung production. It is expected that the coupling of the h_1 to $b\bar{b}$ can be measured with an uncertainty between 2% and $\sim$ 3.5%. For $\tau^+\tau^-$ and gg, the precision is expected to be only slightly worse. Because of the smaller coupling to W bosons, the corresponding uncertainty is found between $\sim$ 4.5% and $\sim$ 12%. The highest precision, however, is expected from the light Higgs boson production via radiation from a Z boson, where an accuracy between 1% and 2% is anticipated. While these precisions are the same for the two models under investigation and as well as for the two $\tan\beta$ regions, they will nevertheless allow for a high-precision test of the 2HDMS/N2HDM predictions. Concerning a possible differentiation of the two models, as before, we find that the different symmetries and couplings do not have any relevant impact on the h_1 coupling analysis. Consequently, in order to distinguish the 2HDMS and the N2HDM more direct phenomenological analyses will have to be performed, see our discussion in Sect. 3.2.4.

5.4.2 Measurements of the h2 couplings

The Higgs boson observed at $\sim$ 125 GeV at the LHC can also serve for the exploration of BSM models. The extended Higgs boson sector of the 2HDMS/N2HDM, in

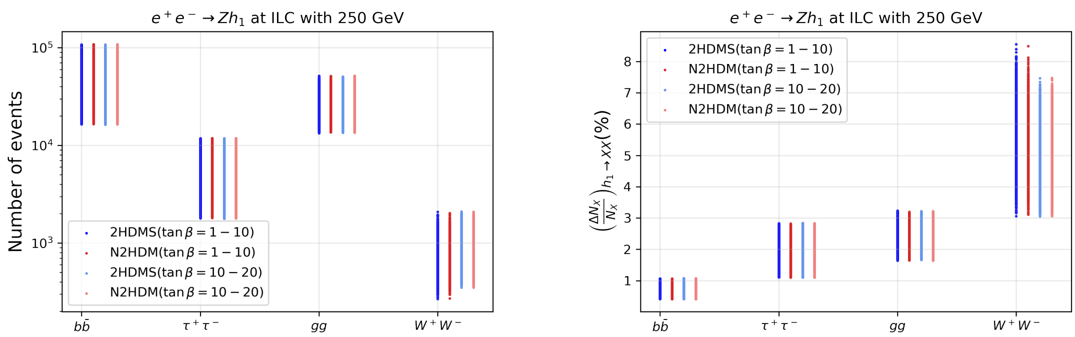

(a) **(b)**

Figure 16: Number of events (left) at the $h_1 \to b\bar{b}$, $h_1 \to \tau^+\tau^-$, $h_1 \to gg$ and $h_1 \to W^+W^-$ final states produced by the Higgs-strahlung process at the ILC, and the respective uncertainties (right) for the 2HDMS and the N2HDM scan points, which are within the 1σ ellipse of the 96 GeV excesses. The ILC center-of-mass energy is $\sqrt{s} = 250$ GeV and the integrated luminosity is $2\,\mathrm{ab}^{-1}$.

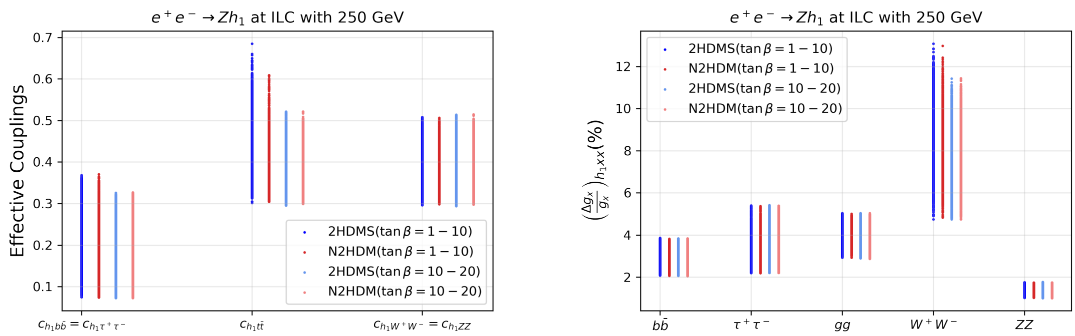

(a) **(b)**

Figure 17: Left: the effective couplings of the h_1 for both 2HDMS and N2HDM in the two $\tan\beta$ regions. Right: the anticipated coupling measurement uncertainties (see text)

particular the mixing of the lighter doublet with the singlet, yields deviations of the h_2 couplings from their SM expectations. In Fig. 18 we compare the predictions of the 2HDMS (blue points) and the N2HDM (red points) for the effective h_2 couplings with the experimental accuracies. As before, special attention is paid to potential differences between the two models, leading possibly to an experimental distinction. Only points within the 1σ ellipse of the 96 GeV excesses are used, where the two $\tan\beta$ regions have been combined. Shown are $c_{h_2}bb$ vs. c_{h_2tt} (upper left), c_{h_2VV} (upper right) and $c_{h_2\tau\tau}$ (lower plot). The black dotted (dashed) ellipses indicate the current ATLAS (CMS) 1σ limits (see Refs. [119]and [120]). The HL-LHC expectation [121], centered around the SM value, are shown as dashed violet ellipses. The orange (green) dashed ellipses indicate the improvements expected from the ILC at 250 GeV (additionally at 500 GeV), based on Ref. [122]. All the points are roughly within the 2σ range of the current Higgs boson rate measurements at the LHC, because of the `HiggsSignals` constraint. No relevant difference between the two models can be observed. While $c_{h_2bb} = c_{h_2\tau\tau}$ can reach the SM value (which by definition of the effective couplings is 1), the couplings to top quarks and to gauge bosons always deviate at least $\sim 5\%$ from the SM prediction. We have checked explicitly that this is due to the agreement with the 96 GeV excesses. For the coupling to top quarks, depending which point in the parameter space is realized, possibly no deviation can be observed, neither with the HL-LHC, nor with the ILC precision. The situation is different for the h_2 coupling to gauge bosons. The HL-LHC precision might still yield a significance below the $\sim 3\sigma$ level. The in this case strongly improved ILC precision, on the other hand, yields for all parameter points of the 2HDMS or the N2HDM a deviation from the SM prediction larger than 5σ. Consequently, the anticipated high-precision h_2 coupling measurements at the ILC will always either rule out the 2HDMS/N2HDM or refute the SM prediction. There will be no distinction visible between the two models via the h_2 coupling determinations. This re-enforces our finding of the h_1 analysis in the previous subsection: only more direct phenomenological analyses will be able to distinguish the 2HDMS and the N2HDM, see our discussion in Sect. 3.2.4.

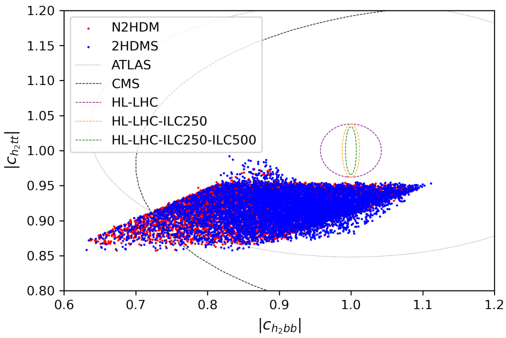

(a)

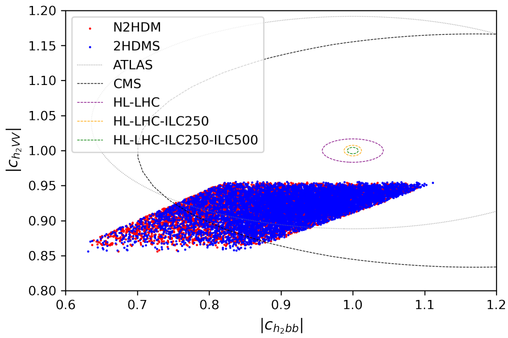

(b)

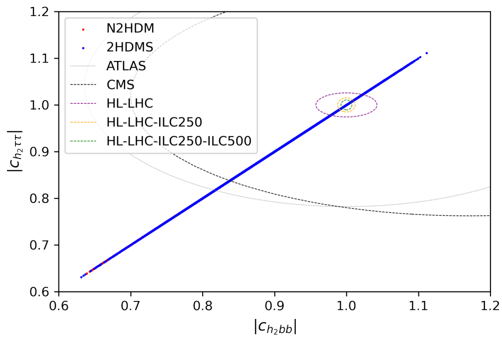

(c)

Figure 18: The effective couplings of the SM-like Higgs-boson h_2. Shown are $|c_{h_2}bb$ vs. c_{h_2tt} (upper left), c_{h_2VV} (upper right) and $c_{h_2\tau\tau}$ (lower plot). The blue (red) points show the 2HDMS (N2HDM) points within the $1\,\sigma$ range of the 96 GeV excesses, with the two $\tan\beta$ ranges combined. The black dotted (dashed) ellipses indicate the current ATLAS (CMS) $1\,\sigma$ limits. The HL-LHC expectation, centered around the SM value, are shown as dashed violet ellipse. The orange (green) dashed ellipses indicate the improvements expected from the ILC at 250 GeV (additionally at 500 GeV).

Part IV

Four top final states as a probe of Two Higgs Doublet Models and its Extensions

6 Four top final states as a probe of Two Higgs Doublet Models

Higgs–top-quark interactions are an especially important part of BSM Higgs physics. For the discovered Higgs boson, the top-Yukawa coupling is the largest Yukawa coupling and plays a crucial role in various production processes (e.g. Higgs production via gluon fusion, Higgs production in association with top-quarks, Z-boson associated Higgs production) and decay channels (e.g. decay to two photons or to two gluons). In order to derive precise constraints, the information from various channels has to be combined.

Similarly, large top-Yukawa couplings are expected for BSM Higgs bosons in many BSM models. Typical examples are the Two-Higgs-Doublet models (2HDM) where this work focuses on. In order too maximise the discovery potential for such BSM Higgs bosons, various channels sensitive to their top-Yukawa coupling should be combined.

In gluon fusion (ggH), in the decay of a Higgs boson into two photons ($H \to \gamma\gamma$) and the subdominant gluon induced ZH production, the top-Yukawa coupling appears at leading-order (LO). At the LHC, there are also production channels which are sensitive to the top-Yukawa coupling already at tree level. These channels are the production of a Higgs boson in association with two top quarks (ttH), with a W boson and a top quark (tWH) and with a single top quark (tqH). If the BSM Higgs bosons are heavy enough, a large top-Yukawa coupling can not only facilitate their production but also their decay into top quarks. This strongly motivates the search for multi-top final states.

Such a search for contributions of heavy BSM scalars to four top final states have been recently studied by CMS in [7]. Such a search for additional heavy scalars is not only sensitive to final states with four top quarks but also to the production of heavy scalars in association with a single (tqH, tWH) or two top quarks (ttH) with a subsequent decay of the scalar into two top quarks. The BSM interpretation in [7] includes upper limits on the cross-section times branching ratio $\sigma((t\bar{t}, tq, tW) + H) \cdot BR(H \to t\bar{t})$ as well as limits on the important quantity tanβ discussed already in Sect. 3. While the cross-section limits show no significant over- or under-fluctuation, they place a strong lower limit on tanβ. The analysis excludes tanβ of up to 1.65 for a 2HDM with a mass degenerated scalar and pseudoscalar Higgs bosons. This low tanβ region is especially interesting for Baryogenesis scenarios in 2HDMs (see e.g. [123]). For low tanβ the top-Yukawa couplings become strong and suppress other channels. This makes final states with multiple tops especially important.

The CMS search is restricted to cross-section limits on a pure scalar or pseudoscalar particle in a mass range of 350 GeV to 650 GeV and assumes that the BSM scalar has no coupling to massive vector bosons. To make this search sensitive to a more general set of models — i.e. accommodating scenarios with $\mathcal{CP}$-mixed scalars as well as scalars with non-zero couplings to massive vector bosons —, we perform a detailed recasting of the analysis and implement the results into `HiggsBounds` in the form of fit functions to ensure easy applicability without the need to run Monte-Carlo simulations.

We reinterpret this analysis by generating Monte-Carlo Events in the most important sub-channels that can contribute to the four top cross-section. These are ttH, tWH and tH production. This is done using `Madgraph5` for event generation and `Madanalysis` for recasting the event. We do this using a simplified model framework for an arbitrary scalar with $\mathcal{CP}$-odd and $\mathcal{CP}$-even couplings to top quarks and couplings to massive vector bosons. We implement this analysis in `HiggsBounds` which makes it easily accessible for a variety of models, including models with $\mathcal{CP}$-violation and models with deviations from the alignment limit. We also expand the original mass range of $350 - 650$ GeV up to 1 TeV. Using this analysis we study the impact on the low tanβ region in a number of models, including the 2HDM, the N2HDM and the complex 2HDM (C2HDM, see [8].)

6.1 Higgs-top quark interaction at hadron colliders for $m_H > 2m_{top}$

There are multiple processes where the top-Yukawa coupling of the Higgs boson appears. For this analysis we restrict ourselves to processes where the Higgs top-Yukawa coupling appears at leading-order (LO). The additional Higgs boson can be a scalar or pseudoscalar, denoted as H and A, respectively. For simplicity we will refer to the additional Higgs boson as H (if not stated otherwise). We start with discussing loop-induced processes which can be mediated by a top-quark loop (among others). Two examples are gluon fusion, which is the dominant production mode at the LHC for a SM like Higgs boson, and the decay into two photons. Both are mediated by a top-quark loop. The decay into two photons also has a dominant W-boson loop for a SM like Higgs boson. Both processes are shown in Fig. 19. There is another loop-induced process involving Higgs top-Yukawa couplings in the subdominant gluon induced ZH production process. The relevant Feynman diagrams for ZH production are shown in Fig. 20. In these loop-induced processes the top-Yukawa coupling enters via a virtual top quark loop (among other particles).

At the LHC there are production channels which are sensitive to the top-Yukawa coupling already at tree level. The channels are Higgs production modes in association with a single or two top qarks. The ttH production is proportional to the top-Yukawa coupling, while tWH and tH production involve contributions of the top-Yukawa couplings and the Higgs–W-boson couplings. The production rate of these particles with an additional single top quark is sizable at masses of $m_H > 2m_{top}$. In Fig. 21 we show exemplary Feynman diagrams for the $t\bar{t}H$, tqH and tWH production. We always assume a subsequent decay of the produced Higgs boson into two top quarks. These processes do not have significant interference with the SM $t\bar{t}t\bar{t}$ production [124]. Furthermore tWH and ttH production modes are difficult to distinguish experimentally. They interfere with each other at next-to-leading order in the five-flavor scheme or at leading-order in the four flavor scheme.

We use this analysis to constrain new on-shell scalar and pseudo-scalar particles with $m_{H,A} > 2m_{top}$. In addition to $t\bar{t}H$ followed by a decay of $H \to t\bar{t}$, we include the additional production channels tqH and tWH.

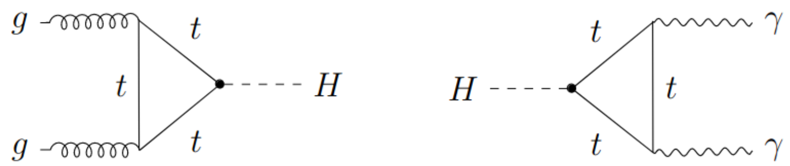

Figure 19: Exemplary Feynman diagrams for $gg \to H$ and $h \to \gamma\gamma$

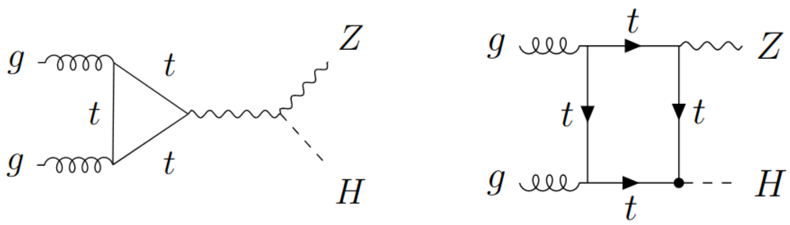

Figure 20: Exemplary Feynman diagrams for the loop-induced subdominant ZH production modes involving Higgs top-Yukawa couplings.

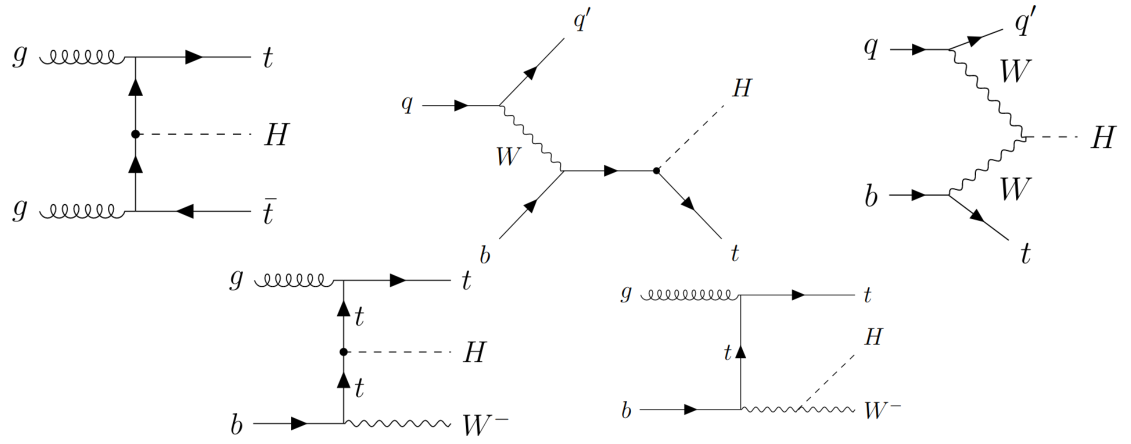

Figure 21: Exemplary Feynman diagrams of tH, $t\bar{t}H$, tWH production. At masses of $m_H > 2m_{top}$ the production of a Higgs boson with a single top quark becomes relevant.

6.1.1 Effective model description

The limits obtained by the analysis should be model independent. To achieve this we use an effective field theory (EFT) approach with a model similar to the Higgs-characterization model defined in [125]. The top-Yukawa part of the Lagrangian scaled with respect to the SM ist given by [126]

$$\mathcal{L}_{Yuk} = -\frac{y_t^{SM}}{\sqrt{2}}\bar{t}(c_t + i\gamma_5\tilde{c}_t)tX. \tag{6.1}$$

Here y_t^{SM} is the SM top-Yuakwa coupling, X denotes a generic Scalar and t denotes the top-quark field and $c_t, \tilde{c}_t, c_V$ are the $\mathcal{CP}$-even and $\mathcal{CP}$-odd coupling to top-quarks rescaled to the SM prediction with $c_t = 1$ and $\tilde{c}_t = 0$. For this study we look at heavy scalars with only top-Yukawa and gauge-boson couplings, which are given by

$$\mathcal{L}_V = c_V X \left(\frac{M_Z^2}{\nu} Z_\mu Z^\mu + 2\frac{M_W^2}{\nu} W_\mu^+ W^{-\mu}\right), \tag{6.2}$$

where W,Z denote the Vector-boson fields with the masses M_Z and M_W, and where c_V is the coupling to Vector-bosons (rescaled to the SM).

6.1.2 Cross section comparison of ttH, tWH and tH at the LHC

In Fig. 22 we compare the production cross sections of the discussed ttH, tWH and tH production modes for a heavy scalar as a function of the mass at the LHC. The blue lines show the production cross-section $\sigma((ttH + tWH), H \to tt)$ for a SM-like Higgs boson (solid line), a $\mathcal{CP}$-even BSM scalar (dashed line) with $c_t = 1$ and a $\mathcal{CP}$-odd BSM scalar (dotted line) with $c_{\tilde{t}} = 1$. If the Higgs boson is SM like, i.e. the gauge boson coupling $c_V = 1$, the cross section becomes significantly smaller for high masses of $m_H > 350$ GeV than the production of a $\mathcal{CP}$-even/odd scalar. This should be compared to tH production of the same particles (red lines). While for a SM-like Higgs boson (solid line) the cross-section is significantly smaller for the mass around the SM Higgs boson $m_h = 125.09$ GeV (due to a large negative interference between the contribution proportional to the top-Yukawa coupling and the contribution proportional to the Higgs–W-boson coupling), the production rate of tH processes for a $\mathcal{CP}$-even BSM scalar (dashed line) line is comparable to ttH production for masses of $m_H < 350$ GeV and is of similar size as tWH production (green dashed line) for $m_H > 350$ GeV. While the cross-section for the tWH channel is almost the same for a $\mathcal{CP}$-even/odd scalar, it would be possible to deduce $\mathcal{CP}$-properties of the produced scalar for ttH and tH production from the production rate, which shows a dependence of the $\mathcal{CP}$-character of the top-Yukawa coupling.

We assume that the Higgs boson produced in ttH, tWH and tH processes dominantly decays into two top quarks for $m_H > 350$. The responsible top-Yukawa coupling will also induce decays to two gluons and two photons. To investigate the size of these contributions, we show in Fig. 23 a comparison of the partical decay widths for a Higgs boson decaying into two top quarks ($H \to t\bar{t}$), two gluons ($H \to gg$) and two photons ($H \to \gamma\gamma$). For a $\mathcal{CP}$-odd scalar the decay into two top quarks (red solid line) is by a factor of ten larger than the decay into two gluons (blue solid line) for small masses around 350 GeV. However, for larger masses and a $\mathcal{CP}$-even scalar the decay into gluons is less than 1% of the decay width into two top quarks. The decay width into two photons (green lines) is two orders smaller than the decay into gluons. Additionally, we show the cross-section for a heavy scalar in ttH, tWH and tH production at a mass of 400 GeV as a function of the $\mathcal{CP}$-even and $\mathcal{CP}$-odd couplings c_t and $c_{\tilde{t}}$ in Fig. 24.

6.2 Recasting process

In the following we will discuss our model independent approach of fitting cross section formulas that depend on the mass and top Yukawa couplings. Further we will give more details about the Monte Carlo Event generation and recasting setup.

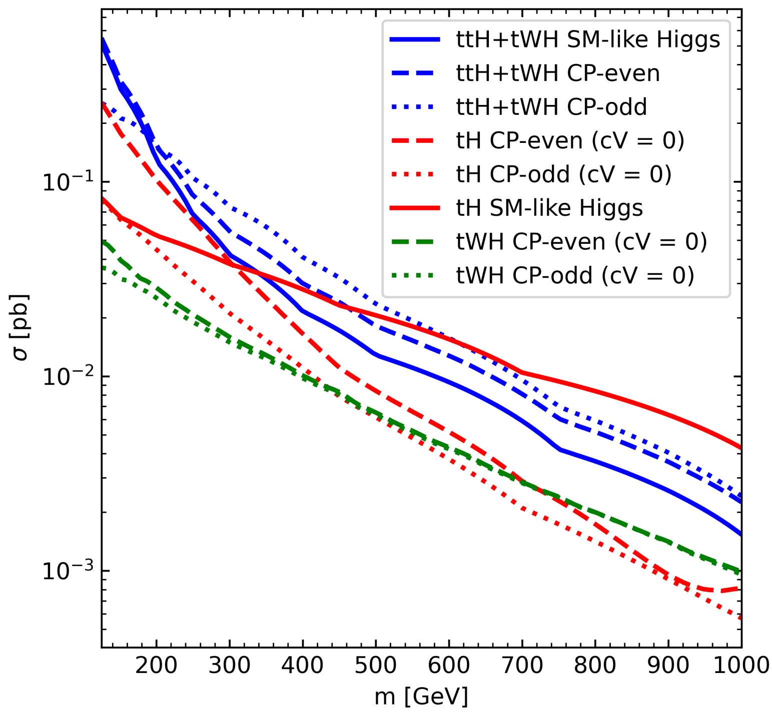

Figure 22: Comparison of the total cross section in tth, tWH and tqH production.

6.2.1 Cross-section fit formulas

We derive fit formulas for the total cross section and the cross section in each signal region in each of the tH, $t\bar{t}H$, tWH subchannels. We would also expect contributions from the ggH production mode. However, we found that the sensitivity of the analysis to the ggH channel is very small. The ggH channel is therefore neglected.

If the width is sufficiently small, it is not parameterized in terms of c_V, c_t, and $c_{\tilde{t}}$, and these cross-sections are proportional to

$$\sigma \propto (a_1 c_V^2 + a_2 c_V c_t + a_3 c_t^2 + a_4 \tilde{c}_t^2) \cdot (b_1 c_t^2 + b_2 \tilde{c}_t^2), \tag{6.3}$$

where the first bracket comes from the production and the second bracket from the decay. All other possible coefficients are zero as a result of the non-interference between $\mathcal{CP}$-even and $\mathcal{CP}$-odd contributions. If more than one scalar is present, we expect a positive interference between them. We make a conservative choice and neglect any expected interference terms. We can then write this as

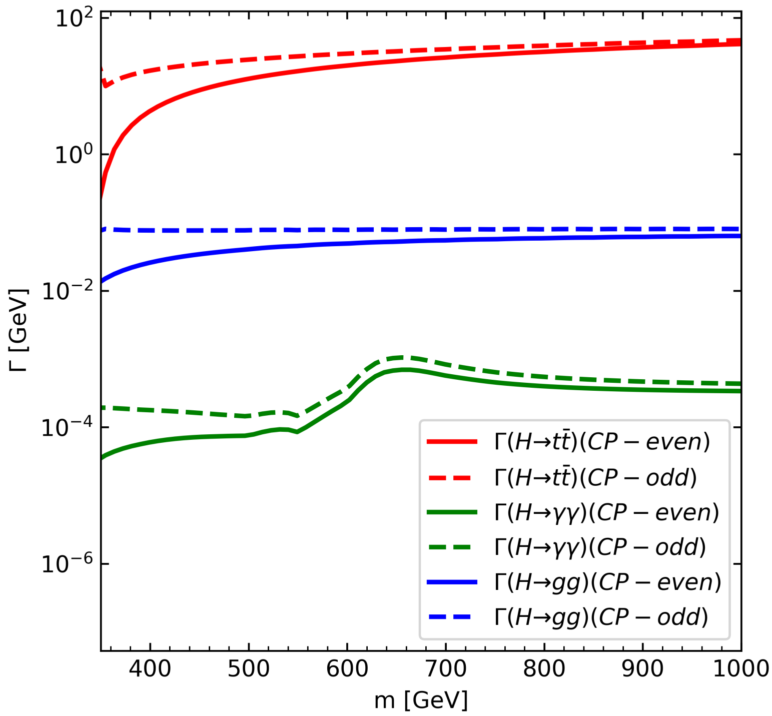

Figure 23: Partial decay width Γ of produced scalar H to two top-quarks, two photons and two gluons.

$$\sigma \propto c_1 c_v^2 c_t^2 + c_2 c_V^2 \tilde{c}_t^2 + c_3 c_V c_t^3 + c_4 c_V c_t \tilde{c}_t^2 + c_5 c_t^4 + c_6 c_t^2 \tilde{c}_t^2 + c_7 \tilde{c}_t^4. \tag{6.4}$$

The coefficients c_i, $i = 1, ..., 7$ of the total cross-section σ_{tot} can be extracted by calculating the cross-sections for 7 different coupling configurations with `MadGraph`. One possible choice is

$$\begin{aligned}
c_t = 1, \tilde{c}_t = 0, c_V = 0 &\longrightarrow \sigma_1 = c_5, \\
c_t = 0, \tilde{c}_t = 1, c_V = 0 &\longrightarrow \sigma_2 = c_7, \\
c_t = 1, \tilde{c}_t = 1, c_V = 0 &\longrightarrow \sigma_3 = c_5 + c_6 + c_7, \\
c_t = 1, \tilde{c}_t = 0, c_V = 1 &\longrightarrow \sigma_4 = c_1 + c_3 + c_5, \\
c_t = 1, \tilde{c}_t = 0, c_V = 2 &\longrightarrow \sigma_5 = 4c_1 + 2c_3 + c_5, \\
c_t = 1, \tilde{c}_t = 1, c_V = 1 &\longrightarrow \sigma_6 = c_1 + c_2 + c_3 + c_4 + c_5 + c_6 + c_7, \\
c_t = 1, \tilde{c}_t = 1, c_V = 2 &\longrightarrow \sigma_7 = 4c_1 + 4c_2 + 2c_3 + 2c_4 + c_5 + c_6 + c_7,
\end{aligned} \tag{6.5}$$

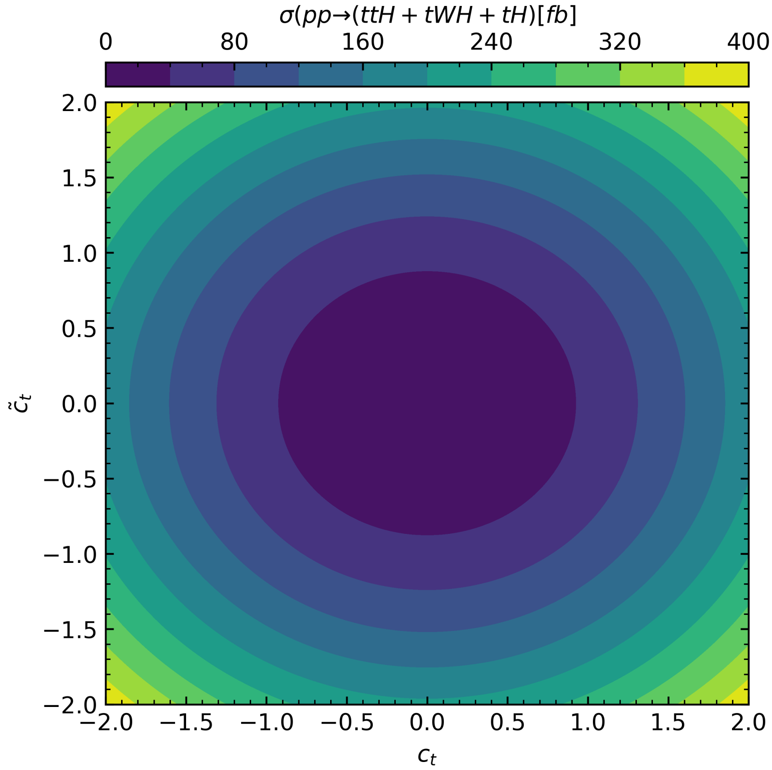

Figure 24: Total cross-section of ttH, tWH and tqH production as a function of c_t and $\tilde{c}_t$ coupling for $c_V = 0$

where σ_i is the cross section for the respective coupling configuration. Using this strategy for different mass values, we obtain the total cross section by running `MadGraph` (see Sect. B.1 for details on the prompts) and read out the total cross section.

To obtain the cross sections for the individual signal regions, we process the generated event samples using `MadAnalysis`. The analysis was implemented and used for studying top-philic scalars in [127]. `MadAnalysis` calculates the efficiency by dividing the number of MC events in the signal region by the initial number of events,

$$\epsilon = \frac{N}{N_{\text{tot}}} \tag{6.6}$$

where N_{tot} is the number of events in the MC sample (and not the number of actual events predicted for the signal region for the given parameter point, which would be $\epsilon\sigma_{\text{tot}}$). The cross section in each signal region is then given by

$$\sigma = \epsilon \cdot \sigma_{\text{tot}}. \tag{6.7}$$

After having derived polynomial fits for both σ and σ_{tot}, we can write down a fit formula for the efficiency ϵ,

$$\epsilon = \frac{\sigma}{\sigma_{\text{tot}}} = \frac{c_1^\sigma c_V^2 c_t^2 + c_2^\sigma c_V^2 \tilde{c}_t^2 + c_3^\sigma c_V c_t^3 + c_4^\sigma c_V c_t \tilde{c}_t^2 + c_5^\sigma c_t^4 + c_6^\sigma c_t^2 \tilde{c}_t^2 + c_7^\sigma \tilde{c}_t^4}{c_1^{\sigma_{\text{tot}}} c_V^2 c_t^2 + c_2^{\sigma_{\text{tot}}} c_V^2 \tilde{c}_t^2 + c_3^{\sigma_{\text{tot}}} c_V c_t^3 + c_4^{\sigma_{\text{tot}}} c_V c_t \tilde{c}_t^2 + c_5^{\sigma_{\text{tot}}} c_t^4 + c_6^{\sigma_{\text{tot}}} c_t^2 \tilde{c}_t^2 + c_7^{\sigma_{\text{tot}}} \tilde{c}_t^4}. \tag{6.8}$$

CMS reports an upper limit on $\sigma(t\bar{t}H + tH + tWH) \cdot \text{BR}(H \to t\bar{t})$. The coupling dependence of the production rate in general scales with c_t^4. If the Higgs boson only decays into top quarks and the decay width is sufficiently small to ignore off-shell effects, the rate scales with c_t^2. For the implementation into `HiggsBounds` we, however, want to keep the width as an independent quantity. For this, we computed the efficiencies for different width values of the decaying Higgs boson (1%, 5%, 10% and 15%), finding only negligible differences of a few percent, making the `HiggsBounds` limit effectively independent of the decay width.

Our implementation will put a limit on the number of event in the most sensitive signal region. For the comparison with the CMS results we can perform the following steps, to derive a limit on the production rate. Given the scaling with c_t^4 for a scalar with $\tilde{c}_t = c_V = 0$, we can then rewrite the production rate as

$$\sigma(t\bar{t}H + tH + tWH) \cdot \text{BR}(H \to t\bar{t}) = c_t^4 \left[\sigma(t\bar{t}H + tH + tWH) \cdot \text{BR}(H \to t\bar{t})\right]_{c_t=1}. \tag{6.9}$$

To obtain an exclusion limit, we can write an expression for the number of signal events as

$$N_{\text{signal}} = \mathcal{L} \cdot \left[\sigma(t\bar{t}H, H \to t\bar{t})\epsilon_{t\bar{t}H} + \sigma(tH, H \to t\bar{t})\epsilon_{tH} + \sigma(tWH, H \to t\bar{t})\epsilon_{tWH}\right], \tag{6.10}$$

which we again can write as

$$N_{\text{signal}} = c_t^4 \mathcal{L} \cdot \left[\sigma(t\bar{t}H, H \to t\bar{t})\epsilon_{t\bar{t}H} + \sigma(tH, H \to t\bar{t})\epsilon_{tH} + \sigma(tWH, H \to t\bar{t})\epsilon_{tWH}\right]_{c_t=1} \tag{6.11}$$

for $\tilde{c}_t = c_V = 0$. We obtain a limit on the number of signal events from the observed

N_l	N_b	N_j	SR	$t\bar{t}t\bar{t}$ (SM signal - CMS)	$t\bar{t}t\bar{t}$ (Background - CMS)
2	3	6	SR5	1.68 ± 0.95	6.7 ± 1.1
2	3	7	SR6	1.20 ± 0.67	3.48 ± 0.66
2	3	≥ 8	SR7	0.88 ± 0.48	1.59 ± 0.49
2	≥ 4	≥ 5	SR8	2.2 ± 1.3	5.5 ± 1.3

Table 10: The most sensitive signal regions (SR) after recasting. N_l is the number of leptons, N_b the number b jets and N_j the total number of jets. We show the numbers reported by CMS for the expected $t\bar{t}t\bar{t}$ number of events and SM background plus $t\bar{t}t\bar{t}$ events.

number of events in each signal region. This allows us to test the couplings and masses of a given model point against the limit on the number of signal events and derive a limit on the couplings and cross-section. Similarly, we find the number of signal events for all coupling configurations with $\tilde{c}_t \neq 0$ and $c_V \neq 0$.

CMS uses a BDT analysis (boosted decision trees), which is a machine learning algorithm (see [128]), to calculate upper limits on the cross-section and other model parameters. We are limited to using the cut-based analysis which divides the events in fourteen signal regions. We treat the total number of events, which is the SM background plus SM $t\bar{t}t\bar{t}$ events, as background for our implementation. Furthermore, we do not know the correlations between the signal regions and are have to derive our limits from the events in the most sensitive signal region. The most sensitive signal regions are shown in table Tab. 10. Signal region 8 was the most sensitive for all recasted MC samples.

In Fig. 25 we show two exemplary fit functions (orange dashed) and data obtained by Eqs. (6.5) (blue) with the error bars coming from the Monte-Carlo simulation. In panel (a) we show the fit function for the coefficient c_5 in ttH production which corresponds to a vertex proportional to c_t^4. The function, whose form is chosen heuristically, is given by

$$c_5(m_X) = 2523.55 \cdot \frac{1}{m_x^2} - 0.0000079 \cdot m_x + 0.0076. \tag{6.12}$$

In panel (b) we show an example of a coefficient which can be neglected because the fit function would be close to zero. All remaining fit functions can be found in Sect. B.

To show the contribution of each coefficient to the cross-section calculation, we compare them in Fig. 26 for (a) ttH and (b) tWH production. The ttH channel in panel (a) only has contributions from c_5 and c_7 while c_6 is zero (see Fig. 25) and c_{1-4} are zero because there is no vertex containing c_V in ttH production. For the tWH channel we have strong negative contributions from $c_{3,6} < 0$ and positive contributions from $c_{1,4,5,7} > 0$ while only c_2 is equal to zero. This shows relevant contributions from vertices which are proportional to c_V in the coefficients c_1, c_3 and c_4. Although some of the coefficients are negative, we checked, that the total efficiencies stay positive in all cases.

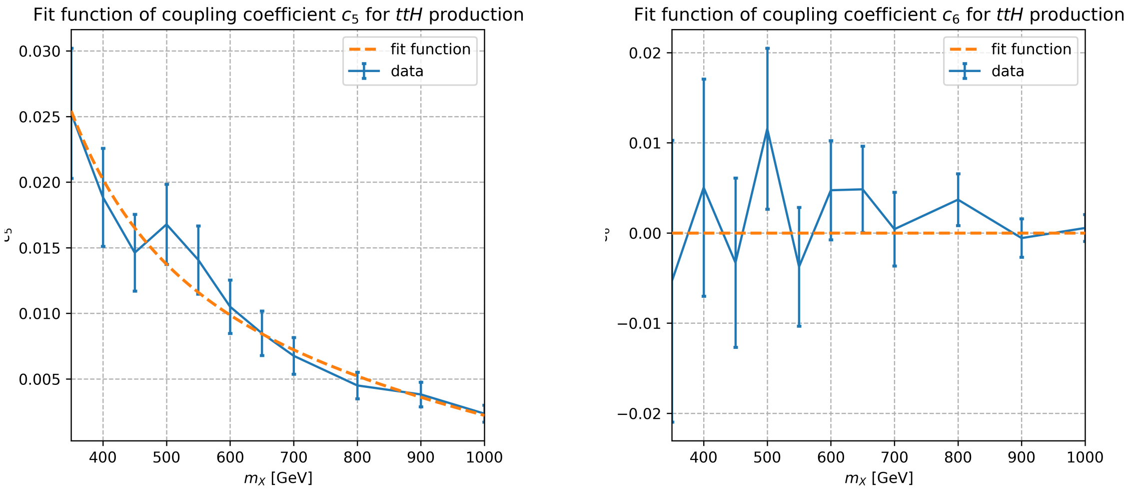

(a) **(b)**

Figure 25: Exemplary fit functions (orange dashed) of the coupling coefficients c_5 (a) and c_6 (b) plotted against the original data. The coefficient in (b) is fitted to 0 and won't contribute to the overall cross section.

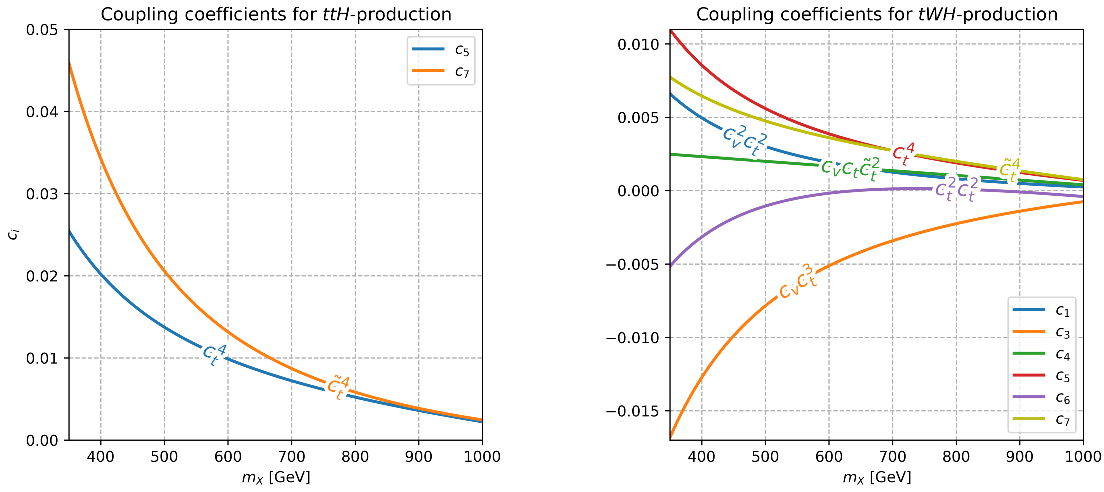

(a) **(b)**

Figure 26: Contributing fit functions for (a) ttH- and (b) tWH-production. While ttH-production does not have any c_V coupling we can see a strong negative contribution from the c_3 coefficient, corresponding to a $c_v c_t^3$ vertex, for tWH production.

6.2.2 Cross-section and tanβ limits

Before we use the obtained limits to study the impact on the 2HDM and its singlet extensions we validate our implementation against the existing results in the CMS analysis [7]. In Fig. 28 we show the cross-section limit for a pure scalar ($c_t = 1$, $c_{\tilde{t}} = 0$, $c_V = 0$) in panel (a), a pseudoscalar ($c_{\tilde{t}} = 1$, $c_t = 0$, $c_V = 0$) in panel (c) and mass degenerate scalar and pseudoscalar in panel (e), obtained from `HiggsBounds` with our implementation for the total production rate $\sigma(pp \to (tt, tW, t) + H) \cdot BR(H \to t\bar{t})$ (red) compared to the limit from CMS (green) and the limit from ttH production only (blue). As expected, because of our limitation to the most sensitive signal region, our limit is overall weaker compared to the CMS result for the total cross-section times branching ratio $\sigma(pp \to (tt, tW, t) + H) \cdot BR(H \to t\bar{t})$. However, in `HiggsBounds` the limits for each subchannel are implemented independently. This means that our implementation could end up with a stronger limit in specific cases, because the cross-section of each sub-channel is compared against the limit. This ensures sensitivity for parameter points with a large cross-section in one subchannel of ttH, tWH or tH but a small cross-section in the other channels. In panel (b), (d) and (f) we show the observed and expected ratio obtained with `HiggsBounds` for the case of a pure scalar, of a pure pseudoscalar and when both are present with the same mass. For a pure scalar masses above $m_H = 350$ GeV are allowed. For a pure pseudoscalar masses below $m_A = 450$ GeV are excluded already. The limit is strongest when both a scalar and a pseudoscalar of the same mass are present. Masses below $m_{H/A} = 650$ are excluded.

In Fig. 27 we compare the upper limits on tanβ obtained from our cross-section functions and `HiggsBounds`. The blue area indicates the excluded observed tanβ area, while the dotted orange line shows the expected limit. The dashed grey line shows the observed limit from the original CMS analysis. Overall, we are in good agreement with the case of a single scalar Higgs boson and two degenerate scalar and pseudo-scalar Higgs bosons. The upper limit for the pseudo-scalar deviates more from the original analysis but is still in good agreement. This is likely explained by the fact that we can only use the most sensitive signal region in our recasting setup while the original analysis uses the BDT (boosted decision tables) analysis and includes correlations between signal regions leading to an overall better sensitivity.

Overall, the implementation in `HiggsBounds` is able to reproduce the CMS results and sets a conservative, slightly weaker limit on the combined production rate $\sigma(pp \to (tt, tW, t) + H) \cdot BR(H \to t\bar{t})$ and on tanβ. This validates our implementation.

In Fig. 29 we show a naive scaling of the observed upper limit on tanβ for the luminosities expected after LHC Run-III ($300\,\mathrm{fb}^{-1}$) and after the completion of the high-luminosity phase (HL-LHC, $3000\,\mathrm{fb}^{-1}$). With the HL-LHC luminosity, we could exclude values of tanβ up to 8 for two degenerate scalar and pseudo-scalar particles with masses of 350 GeV.

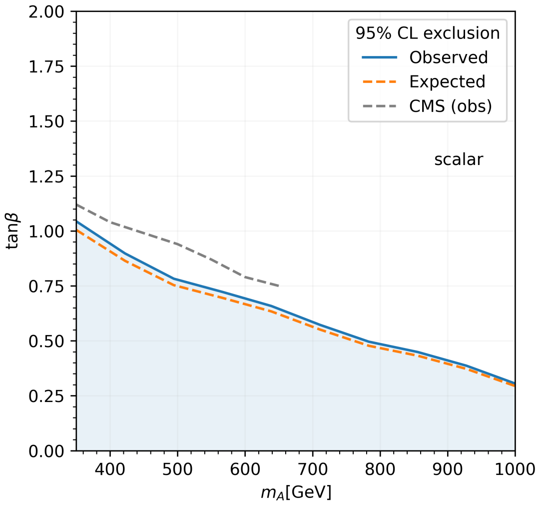

(a)

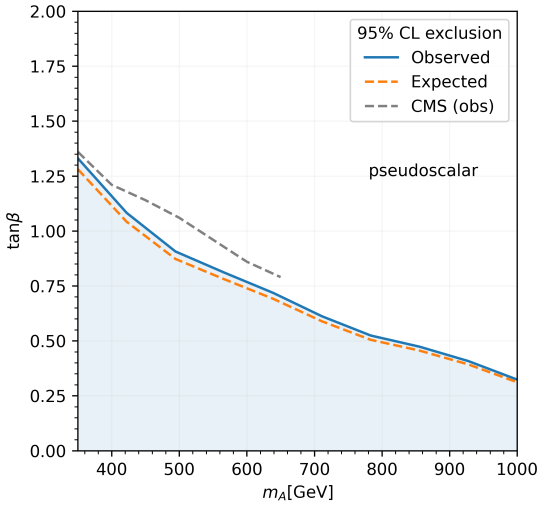

(b)

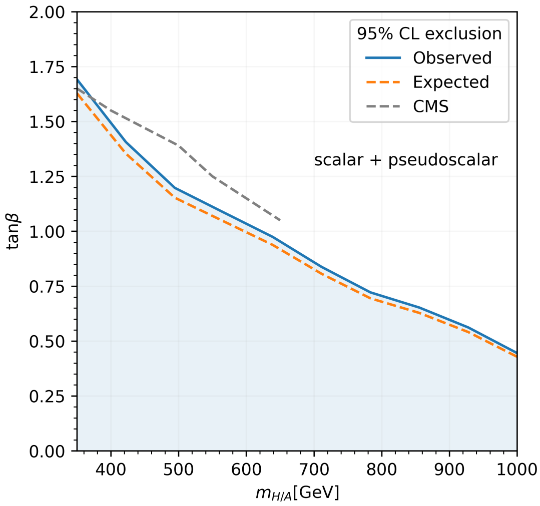

(c)

Figure 27: Observed (blue area) and expected (orange dashed line) upper limits on tanβ compared to the observed limit from the original CMS analysis (grey dashed line) for a scalar (a), pseudo-scalar (b) and scalar + pseudo-scalar of the same mass (c).

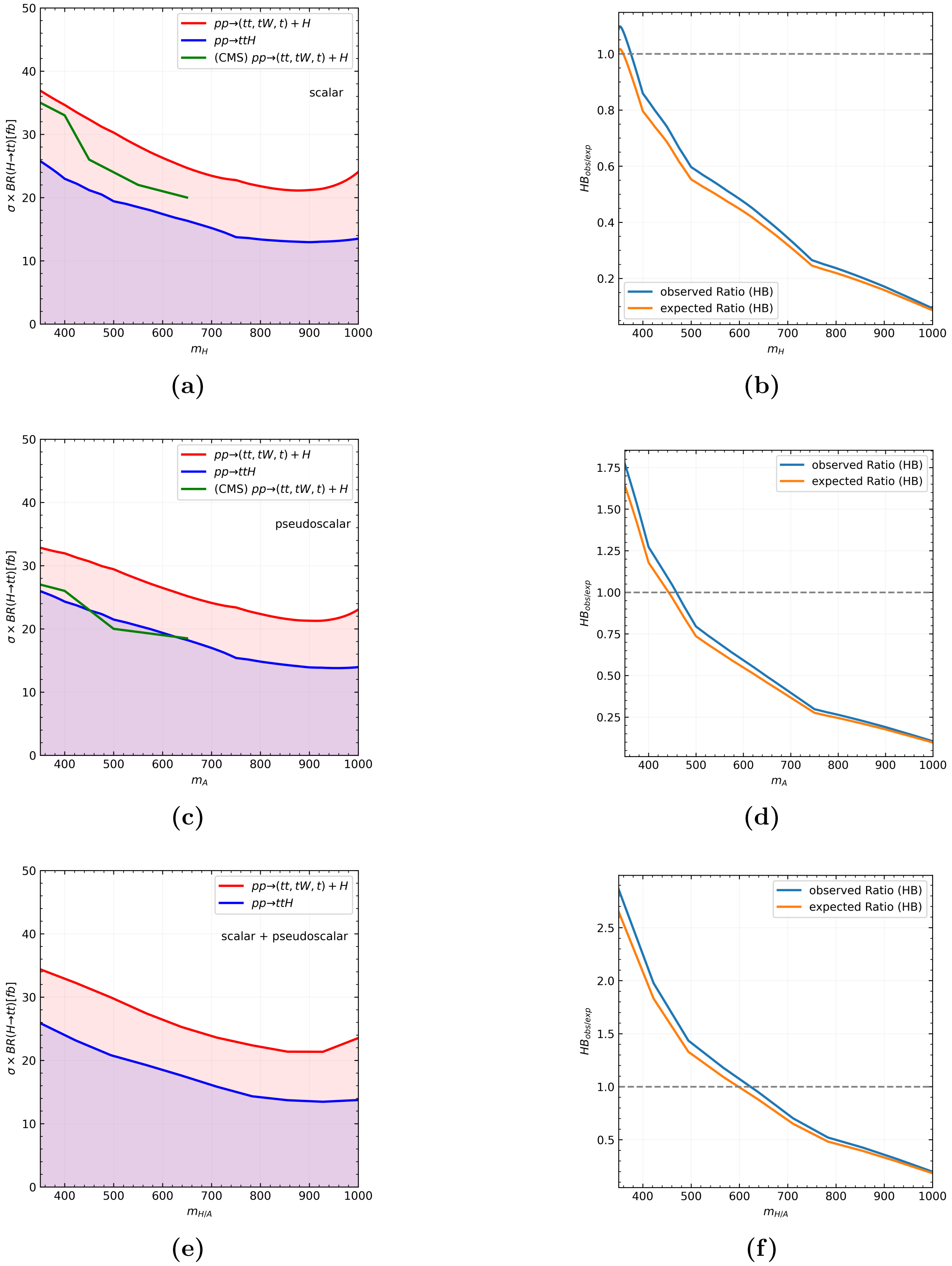

Figure 28: Cross-section limit for a pure scalar ($c_V = 0$, $c_{\tilde{t}} = 0$) (a), a pseudoscalar ($c_V = 0$, $c_t = 0$)(c) and both (e) obtained from `HiggsBounds` with our implementation for the total production rate $\sigma(pp \to (tt, tW, t) + H) * BR(H \to t\bar{t})$ (red) compared to the limit from CMS (green) and the limit obtained from ttH production only (blue). In (b), (d) and (e) we show the respective observed and expected ratio obtained from `HiggsBounds`.

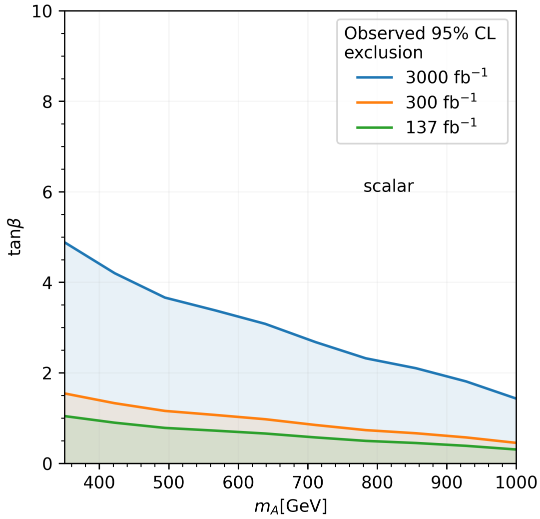

(a)

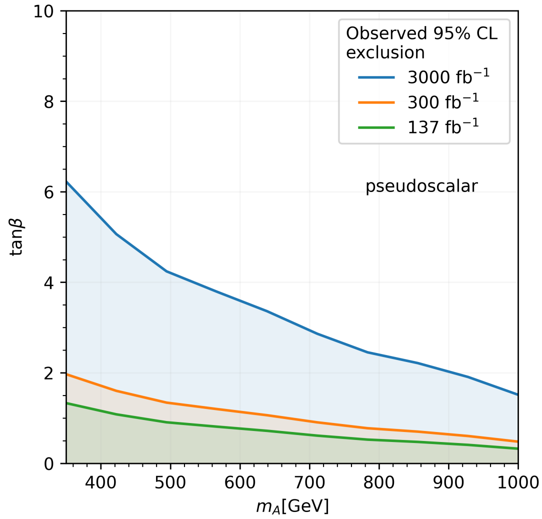

(b)

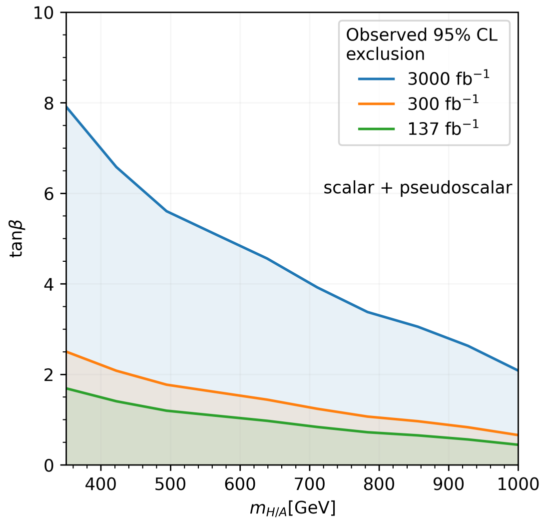

(c)

Figure 29: Naive scaling of the observed limit on $\tan\beta$ for LHC Run-III ($300\,\mathrm{fb}^{-1}$) and HL-LHC ($3000\,\mathrm{fb}^{-1}$)

.

6.3 Impact on the low tanβ region in the 2HDM and its singlet extensions

We validated the model independent cross section limits and tanβ limits in the 2HDM, and can now study the impact on the low tanβ parameter regions of extended 2HDMs. The focus will be on additional parameter space excluded by the four-top analysis and the comparison to existing limits from di-top analyses in [129].

In Fig. 30 we show the excluded parameter regions in the 2HDM Type II in the tanβ-$m_{H/A}$ plane for `Higgsbounds` with the four-top analysis implemented (a) and without it (b). The area for tan$\beta \in [0.2, 1.5]$ and $m_{H/A} \in [400, 750]$ GeV is dominantly excluded by di-top searches from [129] without the four-top analysis. The gap between the excluded plane from the di-top searches around tan$\beta = 0.3$ and tan$\beta = 0$ originates from the width dependence of the di-top limit. The triangular shaped excluded plane for $m_{H/A} \leq 400$ GeV and high tanβ is excluded by the recent $\tau\tau$ search from CMS in [130]. The newly implemented four-top analysis additionally excludes values of tan$\beta < 1.5$ for masses between 350 and 400 GeV. It also extends the excluded region for low tanβ for masses up to 1 TeV and lower tanβ values up to 0.5. In a small area between masses of 600 and 750 GeV it places a stronger limit than existing di-top search while the di-top limits are stronger between 400 and 600 GeV. The new analysis has a substantial impact on the excluded parameter regions for low tanβ.

We show the same tanβ-$m_{H/A}$ plane for the N2HDM in Fig. 30 with the four-top analysis implemented (see panel (a)) and without it (panel (b)). The relevant masses and mixing angles can be found in Tab. 11. As expected the excluded plane is very similar to the 2HDM Type II when both are in the alignment limit. However, without the four-top analysis, the the strongest limit for low $\tan\beta$ is set on the additional light scalar, whose mass is chosen to be 96 GeV, from searches for light Higgs bosons in the di-photon final state in [4]. Furthermore, we study the effects when the masses of the heavy scalar and pseudoscalar are not degenerate. When the pseudo-scalar mass m_A is fixed in Fig. 31 and the tanβ-m_H plane is scanned the di-top search is again the strongest in excluding parameter space for $m_H \in [400, 750]$ without the four-top analysis. If the four-top analysis is applied we excluded tanβ up to 1.2 for $m_H \in [350, 400]$. For $m_H > 660$ GeV the four-top search is selected over the di-top search. The excluded region is now constant with tan$\beta \sim 0.5$ because the limit on the pseudo-scalar with $m_A = 792$ becomes stronger. The small plateau around 800

m_{h_1} [GeV]	m_{h_2} [GeV]	m_{h_3} [GeV]	m_a [GeV]	$m_{H^\pm}$ [GeV]
96	125.09	[350; 1000]	[350; 1000]	800
α_1	α_2	α_3	tanβ	
$\beta - \frac{\pi}{2}$	1.2	0	[0; 3]	

Table 11: Masses and mixing angles of the N2HDM scan.

m_{h_1} [GeV]	m_{h_2} [GeV]	m_a [GeV]	$m_{H^\pm}$ [GeV]	α	tanβ
125.09	[350; 1000]	[350; 1000]	800	$\beta - \frac{\pi}{2}$	[0; 3]

Table 12: Masses and mixing angles of the 2HDM Type II scan.

GeV is explained by `HiggsBounds` clustering the two particles A and H together when they are closer in mass than the mass resolution of the analysis. We see again similar behaviour for the tanβ-m_A plane with fixed scalar mass m_H. The di-top search again gives the strongest exclusion criteria and the four-top analysis acts complementary in excluding parameter space for mass values which are not covered by the di-top searches. For masses of $m_A > 660$ the limit from the four- top analysis again is stronger than the di-top search.

Finally, we study the impact of the four-top analysis in the C2HDM. We choose the parameters as given in Tab. 13 for which the lightest scalar h_1 is SM- like and in the alignment limit. In this limit the couplings for the heavier h_2 and h_3 are CP-mixed. We scan again in the tanβ-m_A plane but for 2 different mixing angles of h_2 and h_3 with $\alpha_3 \in [\frac{\pi}{4}, \frac{\pi}{2}]$. In Fig. 32 without the four-top analysis (left) the only excluded region in the low tanβ region comes from $\gamma\gamma$ searches. The di-top search is only applicable to scalars which are either CP-even or CP-odd (but not for CP-mixed scalars). On the right, we see an excluded region similar to the prior models where the dashed and dotted lines indicate the excluded region for $\alpha_3 = \pi/2$. This highlights the impact of including CP-mixed scalars in our implementation.

m_{h_1} [GeV]	m_{h_2} [GeV]	m_{h_3} [GeV]	$m_{H^\pm}$ [GeV]
125.09	[350; 1000]	[350; 1000]	800
α_1	α_2	α_3	tanβ
β	0	$[\frac{\pi}{4}, \frac{\pi}{2}]$	[0; 3]

Table 13: Masses and mixing angles of the C2HDM scan.

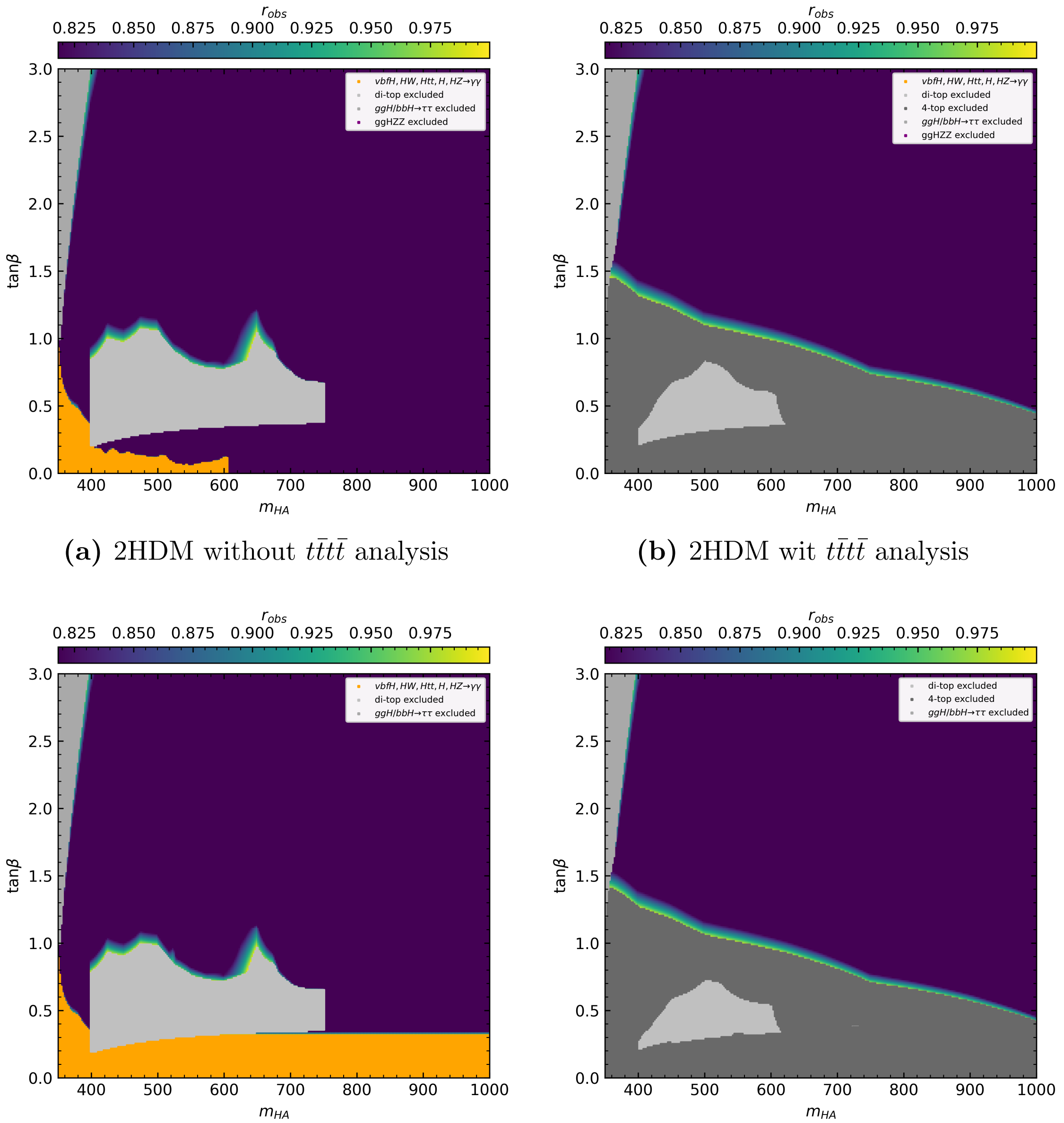

(a) 2HDM without $t\bar{t}t\bar{t}$ analysis

(b) 2HDM wit $t\bar{t}t\bar{t}$ analysis

(c) N2HDM without $t\bar{t}t\bar{t}$ analysis

(d) N2HDM with $t\bar{t}t\bar{t}$ analysis

Figure 30: `HiggsBounds` exclusion in the 2HDM Type II in the tanβ-$m_{H/A}$ plane with degenerate scalar and pseudo-scalar masses for BP1 with (a) and without (b) the four top analysis. The color spectrum shows the observed ratio $r_{obs} < 1$. The plain colors give the analysis leading to exclusion. Without the analysis in (a) the light grey are for $m_{H/A} \in [400, 750]$ gets excluded by di-top searches. With the four top analysis implemented we exclude substantially more parameter space of up to tan$\beta = 2$ for $m_{H/A} = 350$ GeV and tan$\beta = 0.5$ for $m_{H/A} = 1000$ GeV. Panels (c) and (d) show the same plane for the N2HDM Type II. Without the analysis in (a) the light grey are for $m_{H/A} \in [400, 750]$ gets excluded by di-top searches. With the four top analysis implemented we exclude substantially more parameter space of up to tan$\beta = 2$ for $m_{H/A} = 350$ GeV and tan$\beta = 0.5$ for $m_{H/A} = 1000$ GeV. The additional light Higgs boson extends the exclusion from $\gamma\gamma$ searches in [4] compared to the 2HDM.

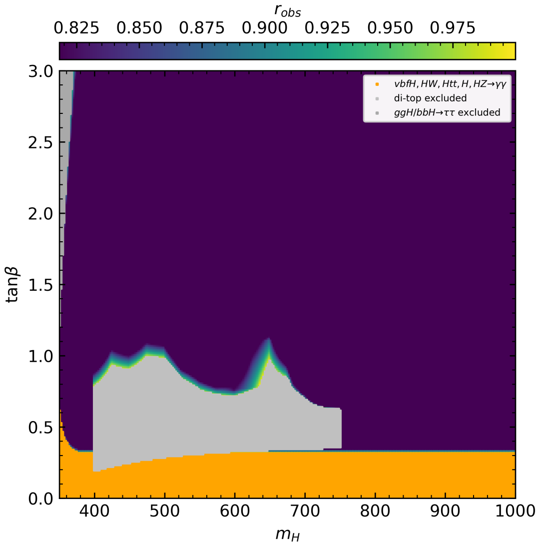

(a) N2HDM without $t\bar{t}t\bar{t}$ analysis and fixed m_H

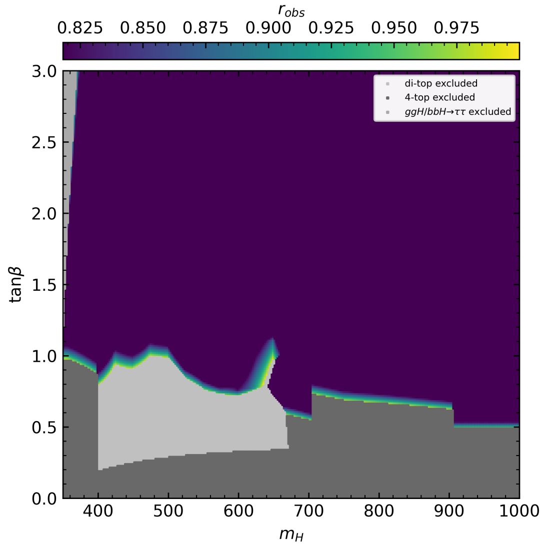

(b) N2HDM with $t\bar{t}t\bar{t}$ analysis and fixed m_H

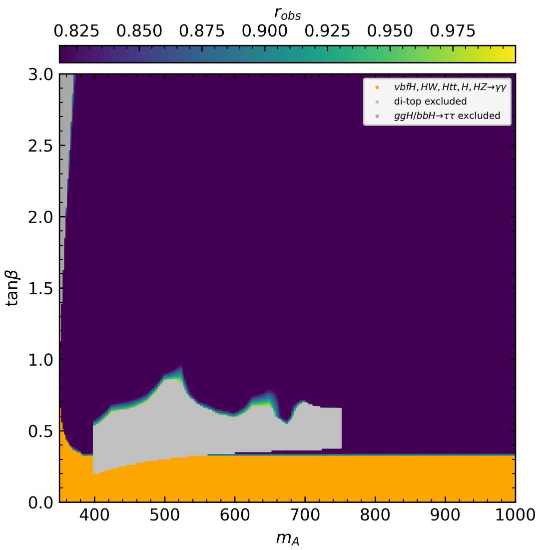

(c) N2HDM without $t\bar{t}t\bar{t}$ analysis and fixed m_A

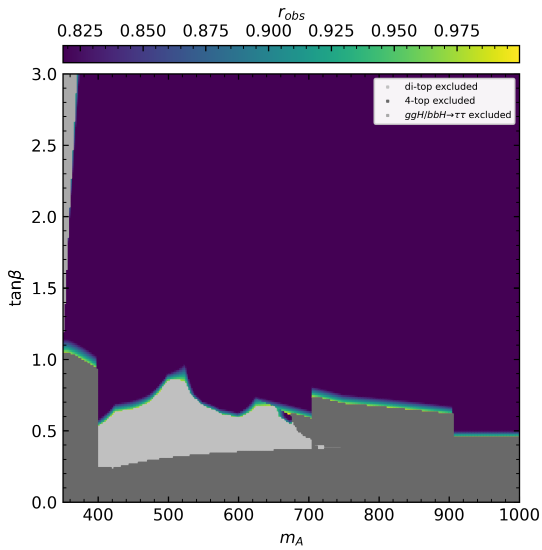

(d) N2HDM with $t\bar{t}t\bar{t}$ analysis and fixed m_A

Figure 31: `HiggsBounds` exclusion in the N2HDM in the tanβ-m_H plane with fixed pseudo-scalar and running scalar mass for BP1 with (a) and without (b) the four top analysis. The color spectrum shows the observed ratio $r_{obs} < 1$. The plain colors give the analysis leading to exclusion. Without the analysis in (a) the light grey are for $m_{H/A} \in [400, 750]$ gets excluded by di-top searches. With the four top analysis implemented we exclude substantially more parameter space of up to tan$\beta = 1.2$ for $m_{H/A} = 350$ GeV and tan$\beta = 0.5$ for $m_{H/A} = 1000$ GeV. In panels (c) and (d) we show the same plane for a fixed pseudoscalar mass. Without the analysis in (a) the light grey are for $m_{H/A} \in [400, 750]$ gets excluded by di-top searches. With the four top analysis implemented we exclude substantially more parameter space of up to tan$\beta = 1$ for $m_{H/A} = 350$ GeV and tan$\beta = 0.4$ for $m_{H/A} = 1000$ GeV.

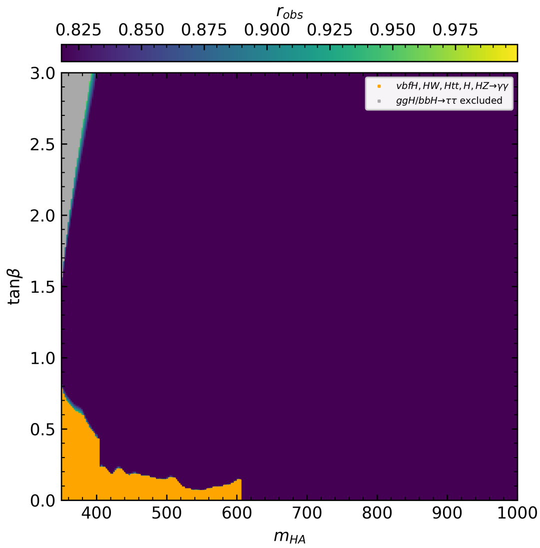

(a) C2HDM without $t\bar{t}t\bar{t}$ analysis and degenerate $m_{H_{2,3}}$

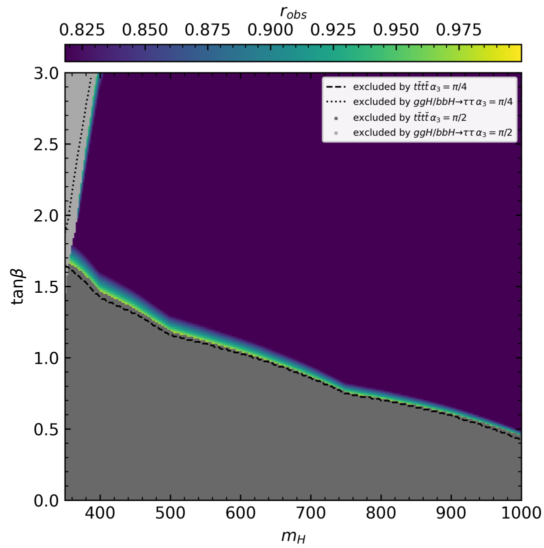

(b) C2HDM with $t\bar{t}t\bar{t}$ analysis and degenerate $m_{H_{2,3}}$

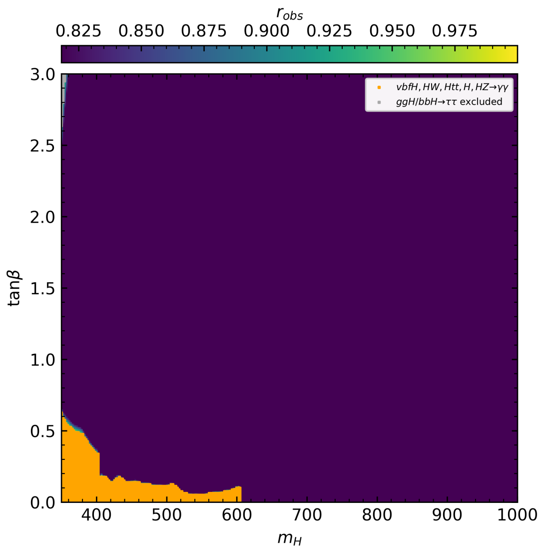

(c) C2HDM without $t\bar{t}t\bar{t}$ analysis and fixed m_{H_2}

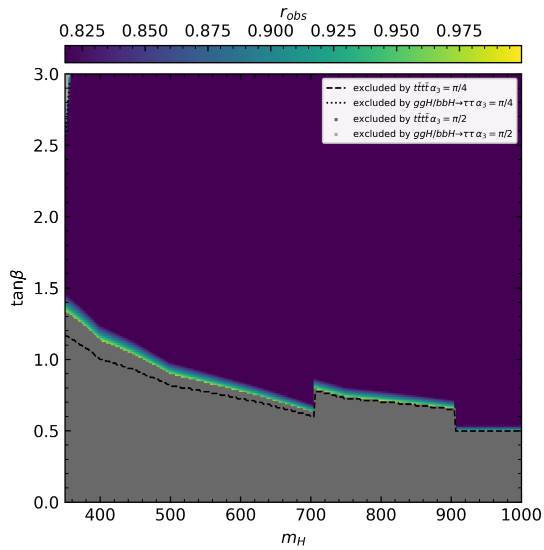

(d) C2HDM with $t\bar{t}t\bar{t}$ analysis and fixed m_{H_2}

Figure 32: `HiggsBounds` exclusion in the C2HDM in the $\tan\beta$-$m_{H/A}$ plane with degenerate heavy scalar masses with (a) and without (b) the four top analysis. The color spectrum shows the observed ratio $r_{obs} < 1$. The plain colors give the analysis leading to exclusion. Without the analysis in (a) only a $\gamma\gamma$-search in [4] is sensitive in the low mass and $\tan\beta$ region and the di-top search is not sensitive to the CP-violating C2HDM. With the four top analysis implemented we exclude substantially more parameter space of up to $\tan\beta = 2$ for $m_{H/A} = 350$ GeV and $\tan\beta = 0.5$ for $m_{H/A} = 1000$ GeV. The dashed lines indicate the exclusion limits for the mixing angle of h_2 and h_3 (α_3) chosen to be equal to $\pi/4$. In panels (c) and (d) we show the same plane for the C2HDM with only one of the heavy scalar masses fixed.

7 Summary and Conclusion

Describing experimental data in the context of BSM models requires a thorough study of the parameter space with respect to theoretical and experimental constraints. In this work we studied the 2HDMS, which was never studied before in an extensive phenomenological context. With the 2HDMS being very similar to the N2HDM in terms of the involved parameters, a comparison of both models was an obvious part of this study.

We introduced the 2HDMS with a $\mathbb{Z}_3$-symmetry and derived a number of theoretical constraints including tree-level perturbative unitarity, boundedness from below and vacuum stability constraints. Studying the bounds of the parameter space with respect to theoretical constraints is the foundation of studying a new model and directly constraints the parameters in the model potential. To describe applications of benchmark points at colliders it is useful to change the basis from the set of input parameters of the potential to physical parameters such as masses and mixing angles. These benchmark points have to be tested against constraints coming from experiments. These include searches for additional Higgs Bosons at experiments like CMS and ATLAS, as well as measurements of the properties of the observed Higgs boson. Constraints from flavor physics usually place a constrain on the mass of the charged Higgs boson and tanβ.

In Sect. 5 we interpreted a $\sim 3\sigma$ excess at CMS and a $\sim 2\sigma$ excess at LEP as a light Higgs boson and accomodated both excesses simultaneously in the 2HDMS and N2HDM. We found that both models are equally well able to describe the the observed signals for the low and high tanβ region. Our efforts then focused on possibilities to distinguish the very similar models experimentally. The first step was to study the precision of coupling measurements at a future linear collider. We found that precision for various channels, such as $b\bar{b}$, $t\bar{t}$ and gauge boson couplings are very similar in the 2HDMS and N2HDM. We give an outlook on further possibilities to distinguish the models. These focus on the properties of the $\mathcal{CP}$-odd Higgs bosons. The N2HDM only has one $\mathcal{CP}$-odd Higgs boson, whereas the 2HDMS has two and an additional $\mathcal{CP}$-odd mixing angle.

In the second part of this work we studied the impact of the search for additional heavy Higgs bosons in final states with up to four top quarks on the low tanβ region of 2HDMs. We used an analysis published by CMS as baseline and extended it via Monte-Carlo-Event generation and recasting to higher masses and the possibilities of

$\mathcal{CP}$-mixed Higgs bosons. The results were used for a first of this kind implementation into the public code `HiggsBounds`, which is a code that directly tests scenarios in BSM models against searches for additional Higgs bosons at collider experiments. Searches are usually implemented as an upper limit on the production rate (cross section times branching ratio). The results from our anaylsis were implemented as functions of the effficiency as a function of the mass, the involved $\mathcal{CP}$-odd and $\mathcal{CP}$-even couplings and the coupling to gauge bosons. We found good agreement with our implementation and the original anaylsis performed by CMS for a pure $\mathcal{CP}$-even $\mathcal{CP}$-odd Higgs boson. We studied the constraints, which the new limit places on the low tanβ region in the 2HDM and the N2HDM. Further, we studied the impact on the C2HDM which includes $\mathcal{CP}$-violating phases. We found that the analysis can complement existing di-top searches and can exclude up to tan$\beta = 1.5$ for masses of the additional Higgs bosons of 350 GeV if a mass degenerate $\mathcal{CP}$-even and $\mathcal{CP}$-odd Higgs boson are present. In the C2HDM we exclude a similar plane but the di-top searches are not $\mathcal{CP}$-sensitive and not present in this model. This allowes us to place much stronger limits on the low tanβ region in this model than previous searches.

The phenomenological studies in this thesis have been carried not only to show the capibities of 2HDMs and its extensions to describe hints of BSM physics observed at the experiment, but also to give a starting point for the experimental distinction of models that share a very similar parameter space and phenomenological properties. The discussed signals of a possible light Higgs boson with a mass of ~ 96 GeV will be topic of further studies, motivated by a recently described signal at ~ 95 by CMS in [131]. Our results from the recasting of the four-top analysis by CMS can be used to constrain low tan β scenarios, which are often important for the description of baryogenesis which requires sources of $\mathcal{CP}$-violation.

A Evaluation of experimental coupling uncertainties for a light Higgs boson

In this section we describe in detail how we estimate the experimental uncertainties of the coupling measurements of a Higgs boson below 125 GeV based on ILC250 measurements. This section was taken from [6]. [1] We would like to stress that this constitutes the first analysis of this type: to which precision the couplings of a BSM Higgs boson can be measured at a future e^+e^- collider. This facilitates future phenomenological analysis that may allow to obtain information about the underlying model and its preferred parameter space.

A.1 SM Higgs-boson results

In this subsection we denote the SM Higgs boson as h and assume a mass of 125 GeV. The cross section at the ILC250 is given as

$$\sigma(e^+e^- \to Zh) = 206\,\mathrm{fb}. \tag{A.1}$$

The BRs are taken from Ref. [132] and summarized in Tab. 14.

Final state	$b\bar{b}$	$c\bar{c}$	gg	$\tau^+\tau^-$	WW^*
Branching ratios	0.582	0.029	0.082	0.063	0.214

Table 14: BRs of the SM Higgs boson [132].

The SH Higgs coupling uncertainties have been obtained in Ref. [133] (Tab. 2), assuming $\mathcal{L}_{\rm int} = 2\mathrm{ab}^{-1}$ at $\sqrt{s} = 250$ GeV (i.e. the ILC250). The results are given in Tab. 15.

Coupling	$b\bar{b}$	$c\bar{c}$	gg	$\tau^+\tau^-$	WW	ZZ
Relative uncertainties [%]	1.04	1.79	1.60	1.16	0.65	0.66

Table 15: Relative uncertainties in the SM Higgs couplings, $\Delta g_x/g_x$, at the ILC250 [133].

The numbers for the ratio of signal-over-background events, $S/B(=: f_h)$ of a SM Higgs boson at 125 GeV at the ILC250 are given in Tab. 16 [134]. The hZZ coupling is determined directly from the cross section, where the $q\bar{q}h$ mode can be neglected.

[1] We thank M. Cepeda for invaluable help in this section. We also thank J. Tian for providing ILC numbers.

The other couplings should be taken in the $q\bar{q}h$ mode, corresponding effectively to $e^+e^- \to Z^* \to Zh \to q\bar{q}h$ (with the subsequent Higgs decay).

Measurement	Efficiency	S/B
σ_{Zh} in $\mu^+\mu^-h$	88%	1/1.3
σ_{Zh} in e^+e^-h	68%	1/2.0
BR($h \to b\bar{b}$) in $q\bar{q}h$	33%	1/0.89
BR($h \to c\bar{c}$) in $q\bar{q}h$	26%	1/4.7
BR($h \to gg$) in $q\bar{q}h$	26%	1/13
BR($h \to \tau^+\tau^-$) in $q\bar{q}h$	37%	1/0.44
BR($h \to WW$) in $q\bar{q}h$	2.6%	1/0.96

Table 16: Numbers for S/B at the ILC250 [134].

A.2 Basic signal-background statistics

In this section we use the following notation: $N_S(\equiv S)$: number of signal events; $N_B(\equiv B)$: number of background events; N_T: total number of events with. Then one finds

$$N_S = N_T - N_B, \tag{A.2}$$

$$f = N_S/N_B. \tag{A.3}$$

The background is taken after cuts, i.e. "irreducible background", likely to be small at an e^+e^- collider. For the uncertainties we have

$$\Delta N_S^2 = \Delta N_T^2 + \Delta N_B^2. \tag{A.4}$$

The uncertainty of the total number of events scales like

$$\Delta N_T = \sqrt{N_T}. \tag{A.5}$$

The uncertainty of the background goes like

$$\Delta N_B = \epsilon_{\text{syst},B} \cdot N_B, \tag{A.6}$$

where $\epsilon_{\text{syst},B}$ denotes the relative uncertainty for background estimation (which cancels out later). Therefore,

$$\Delta N_S^2 = \left(\sqrt{N_T}\right)^2 + \left(\epsilon_{\text{syst},B} \cdot N_B\right)^2, \tag{A.7}$$

$$\Delta N_S = \sqrt{(N_S + N_B) + \epsilon^2_{\text{syst},B} N_B^2}. \tag{A.8}$$

If the background is known perfectly, one has an overall uncertainty fully dominated by the purely statistical uncertainty,

$$\epsilon_{\text{syst},B} = 0, \tag{A.9}$$

$$\begin{aligned}\Delta N_S &= \sqrt{N_S + N_B}\\ &= \sqrt{N_S + N_S/f}\\ &= \sqrt{N_S\,(1 + 1/f)}\\ &= \sqrt{N_S} \cdot \sqrt{1 + 1/f},\end{aligned} \tag{A.10}$$

$$\Delta N_S/N_S = \frac{1}{\sqrt{N_S}} \cdot \sqrt{1 + 1/f}. \tag{A.11}$$

Consequently, the uncertainty improves with $\sqrt{N_S}$ if $f = N_S/N_B \gg 1$. On the other hand, if f is small, one wins less from the gain in statistics.

A.3 Evaluation of uncertainties in the Higgs couplings

A.3.1 Cross section evaluation

The production cross section for a Higgs ϕ at an e^+e^- collider is evaluated as

$$\sigma(e^+e^- \to \phi Z) = \sigma_{\text{SM}}(e^+e^- \to H^\phi_{\text{SM}} Z) \times |c_{\phi VV}|^2. \tag{A.12}$$

Here H^ϕ_{SM} is the SM Higgs boson with a hypothetical mass equal to m_ϕ. $c_{\phi VV}$ is the coupling strength of the ϕ to two gauge bosons ($V = W^\pm, Z$) relative to the SM value. In Fig. 33 we show the evaluation of $\sigma_{\text{SM}}(e^+e^- \to H^\phi_{\text{SM}} Z)$ (where H^ϕ_{SM} is labeled H) at the tree-level ("tree") and the full one-loop level ("full") [135], including soft and hard QED radiation.[2] One can see that the loop corrections are important for the reliable evaluation of this cross section. Explicit numbers are given in Tab. 17. Multiplying the loop corrected cross section with $|c_{\phi VV}|^2$ is an approximation that works well for $m_\phi \gtrsim 75$ GeV and requires more scrutiny for the lowest Higgs-boson

[2]We thank C. Schappacher for providing the calculation.

masses.

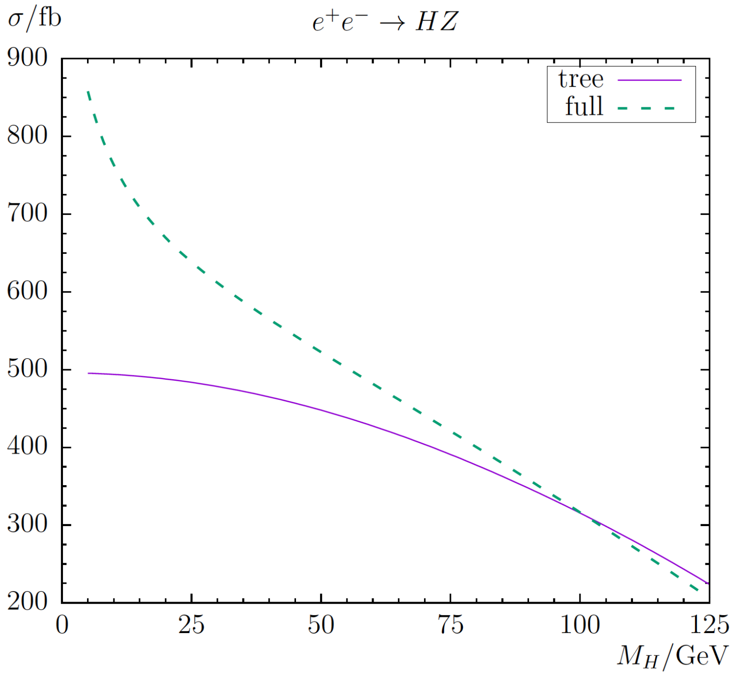

Figure 33: Production cross section for “SM Higgs bosons” with $m_H \leq 125$ GeV [135].

m_ϕ [GeV]	5	10	20	30	40	50	60	70	80	90	96	100	110	120
σ_{HZ} [fb]	858	763	670	611	565	523	482	441	400	359	333	316	273	228

Table 17: Production cross section for “SM Higgs bosons” with $m_\phi \equiv m_H \leq$ 125 GeV [135].

A.3.2 Signal over background for the new Higgs boson

An important element for the evaluation of the Higgs-boson coupling uncertainties is the number of signal over background events for ϕ,

$$\left(\frac{N_S}{N_B}\right)_\phi =: f_\phi \tag{A.13}$$

relative to the SM value(s) as given in Tab. 16,

$$\left(\frac{N_S}{N_B}\right)_h =: f_h \tag{A.14}$$

with

$$\left(\frac{N_S}{N_B}\right)_h \Big/ \left(\frac{N_S}{N_B}\right)_\phi = f_h/f_\phi =: D. \tag{A.15}$$

Unfortunately, there is no (neither general nor model specific) evaluation of f_ϕ or D available. However, for the ILC500 "SM-like" Higgs bosons with masses above and below 125 GeV have been simulated [117]. One finds that in this case very roughly $D \approx 2$ can be assumed. For our evaluation we use $D = 3$ as a conservative value.

A.3.3 Relating signal events to Higgs couplings

In this subsection we derive the evaluation of the uncertainties in the (light) Higgs-boson couplings. We denote the generic coupling of a Higgs ϕ to another particle x as g_x. There are two cases:

(i) The coupling is determined via the decay $\phi \to xx$. The number of signal events is given by

$$N_S = \mathcal{L}_{\text{int}} \times \sigma(e^+e^- \to \phi Z) \times \text{BR}(\phi \to xx) \times \epsilon_{\text{sel}} \times \text{BR}(Z \to q\bar{q}), \tag{A.16}$$

$$\text{BR}(\phi \to xx) = \frac{\Gamma(\phi \to xx)}{\Gamma_{\text{tot}}}, \tag{A.17}$$

where ϵ_{sel} is the selection efficiency. In the formulas below ϵ_{sel} and $\text{BR}(Z \to q\bar{q})$ cancel out, but they enter in the N_S/N_B evaluation, i.e. in the numbers of S/B given in Tab. 16, as well as in the coupling precisions given in Tab. 15. The decay channel $\phi \to xx$ gives not only $\Gamma(\phi \to xx)$, but also contributes to Γ_{tot}. For simplicity we assume

$$\text{BR}(\phi \to xx) = \frac{g_x^2}{g_x^2 + g^2}, \tag{A.18}$$

where g^2 (modulo canceled prefactors) summarizes the other contributions. The relative strength between g_x and g is given by

$$(p-1)g_x^2 = g^2, \tag{A.19}$$

$$\Rightarrow \quad \text{BR}(\phi \to xx) = \frac{1}{p}. \tag{A.20}$$

Then one finds

$$N_S + \Delta N_S \propto \text{BR} + \Delta\text{BR}$$

$$= \frac{g_x^2(1+\Delta g_x/g_x)^2}{g_x^2(1+\Delta g_x/g_x)^2+(p-1)g_x^2}$$

$$= \frac{1}{p}\left(1+2\frac{\Delta g_x}{g_x}-2\frac{\Delta g_x}{g_x\, p}\right) \tag{A.21}$$

$$\Rightarrow \quad \Delta\mathrm{BR} = \frac{1}{p}\left(2\frac{\Delta g_x}{g_x}-2\frac{\Delta g_x}{g_x\, p}\right), \tag{A.22}$$

$$\Rightarrow \quad \frac{\Delta N_S}{N_S} = \frac{\Delta\mathrm{BR}}{\mathrm{BR}} = 2\frac{\Delta g_x}{g_x} - 2\,\frac{\Delta g_x}{g_x\, p}$$

$$= 2\frac{\Delta g_x}{g_x}\left(1-\frac{1}{p}\right). \tag{A.23}$$

(ii) The coupling is determined via the production cross section. This is the case for g_Z.

Then one can assume [where as above the $\mathrm{BR}(Z \to \ell^+\ell^-)$ cancels out]

$$N_S \propto \sigma(e^+e^- \to \phi Z) \times \mathrm{BR}(Z \to e^+e^-, \mu^+\mu^-) \propto g_Z^2, \tag{A.24}$$

$$N_S + \Delta N_S \propto (g_Z + \Delta g_Z)^2 . \tag{A.25}$$

$$\Delta N_S/N_S \propto 2\frac{\Delta g_Z}{g_Z}. \tag{A.26}$$

A.3.4 Uncertainty in the Higgs couplings

In the following we denote the SM Higgs boson as h, and the new Higgs boson at 96 GeV as ϕ. For the SM Higgs boson we have

- $\sigma(e^+e^- \to Zh)$ from Eq. (A.1) and $\mathrm{BR}(h \to xx)$ from Tab. 14, which gives us $N_{S,h}$.
- $\left(\frac{N_S}{N_B}\right)_h$ from Tab. 16.
  This allows us to evaluate $\left(\frac{\Delta N_S}{N_S}\right)_h$ via Eq. (A.11).
- $\left(\frac{\Delta g_x}{g_x}\right)_h$ from Tab. 15.

For the new Higgs boson ϕ we have

- $N_{S,\phi}$ from Eq. (A.16).
- For $\left(\frac{N_S}{N_B}\right)_\phi$ we assume $f_h/f_\phi = D$ with $D = 2$ as starting/central point.
  This allows us to evaluate $\left(\frac{\Delta N_S}{N_S}\right)_\phi$ via Eq. (A.11). Here it should be kept in

mind that D is a priori unknown. We use, as discussed above, $D = 3$ as a conservative value.

Using the proportionality relations one can evaluate the coupling precision in the two cases:

(i) The coupling determined via the decay $\phi \to xx$. Here one finds

$$\frac{\left(\frac{\Delta g_x}{g_x}\right)_\phi}{\left(\frac{\Delta g_x}{g_x}\right)_h} = \frac{\left(\frac{\Delta N_S}{N_S}\right)_\phi}{\left(\frac{\Delta N_S}{N_S}\right)_h} \times \frac{\left(1 - \frac{1}{p_h}\right)}{\left(1 - \frac{1}{p_\phi}\right)}, \tag{A.27}$$

and can thus evaluate $\left(\frac{\Delta g_x}{g_x}\right)_\phi$ using

$$\frac{\left(\frac{\Delta N_S}{N_S}\right)_\phi}{\left(\frac{\Delta N_S}{N_S}\right)_h} \times \frac{\left(1 - \frac{1}{p_h}\right)}{\left(1 - \frac{1}{p_\phi}\right)} = \frac{\left(\frac{\sqrt{1+1/f_\phi}}{\sqrt{N_{S,\phi}}}\right)}{\left(\frac{\sqrt{1+1/f_h}}{\sqrt{N_{S,h}}}\right)} \times \frac{\left(1 - \frac{1}{p_h}\right)}{\left(1 - \frac{1}{p_\phi}\right)} \tag{A.28}$$

$$= \frac{\sqrt{1 + D/f_h}}{\sqrt{1 + 1/f_h}} \times \frac{\sqrt{N_{S,h}}}{\sqrt{N_{S,\phi}}} \times \frac{(1 - \mathrm{BR}(h \to xx))}{(1 - \mathrm{BR}(\phi \to xx))} \tag{A.29}$$

$$= \sqrt{\frac{D + f_h}{1 + f_h}} \times \sqrt{\frac{\sigma(e^+e^- \to Zh)}{\sigma(e^+e^- \to Z\phi)}} \times \sqrt{\frac{\mathrm{BR}(h \to xx)}{\mathrm{BR}(\phi \to xx)}} \tag{A.30}$$

$$\times \frac{(1 - \mathrm{BR}(h \to xx))}{(1 - \mathrm{BR}(\phi \to xx))}. \tag{A.31}$$

(ii) The coupling is determined via the production cross section, i.e. g_Z. Here we find

$$\frac{\left(\frac{\Delta g_Z}{g_Z}\right)_\phi}{\left(\frac{\Delta g_Z}{g_Z}\right)_h} = \frac{\left(\frac{\Delta N_S}{N_S}\right)_\phi}{\left(\frac{\Delta N_S}{N_S}\right)_h}, \tag{A.32}$$

and can thus evaluate $\left(\frac{\Delta g_Z}{g_Z}\right)_\phi$ using

$$\frac{\left(\frac{\Delta N_S}{N_S}\right)_\phi}{\left(\frac{\Delta N_S}{N_S}\right)_h} = \frac{\sqrt{N_{S,h}}}{\sqrt{N_{S,\phi}}} \tag{A.33}$$

$$= \sqrt{\frac{\sigma(e^+e^- \to Zh)}{\sigma(e^+e^- \to Z\phi)}}. \tag{A.34}$$

B Four-top analysis: details on implementation into HiggsBounds

B.1 Monte-Carlo and detector-simulation

The events for ttH, tWH and tH production at the LHC at NLO accuracy can be generated using MadGraph5 by issuing the following commands.

For ttH production:

```
import model HC_NLO_X0-no_b_mass

define p = g d d~ u u~ s s~ c c~ b b~
define j = g d d~ u u~ s s~ c c~ b b~

generate p p > x0 t t~

output
```

For tWH production:

```
import model HC_NLO_X0-no_b_mass

define p = g d d~ u u~ s s~ c c~ b b~
define j = g d d~ u u~ s s~ c c~ b b~

generate p p > t w- x0
add process p p > t~ w+ x0

output
```

For tH production:

```
import model HC_NLO_X0-no_b_mass

define p = g d d~ u u~ s s~ c c~ b b~
define j = g d d~ u u~ s s~ c c~ b b~

generate p p > t j x0 $$ w+ w-
add process p p > t~ j x0 $$ w+ w-

output
```

The relevant parameters can then be given via the following commands:

```
launch
shower=PYTHIA8
madspin=on
set nevents 50000
set cosa 0.707106
set kSM 0
set kHtt 1
set kAtt 0
set MX0 350
set WX0 auto
set pdflabel lhapdf
set lhaid 303600
```

where `kHtt`, `kAtt` and `kSM` are the $\mathcal{CP}$-even, $\mathcal{CP}$-odd and coupling to vector bosons of the Higgs boson. `MX0` is the mass of the additional Higgs boson and `WX0 auto` ensures that the width of the particle is calculated via `MadWidth`. As discussed in Sect. 6 the impact of the width can be neglected.

B.2 Cross-section coefficient fit functions

In the following we show all fit functions $c_i(m_X)$, where $i \in \{1, 7\}$, used to calculate the cross-section depending on the mass m_X and the couplings $c_t, \tilde{c}_t$ and c_V as described in Sect. 6.

B.2.1 ttH-production

The fit functions for the coefficients in $\sigma_{\epsilon,ttH}$ are given in the form $c_{i,\epsilon,ttH}$ by

$$\begin{aligned} c_{5,\epsilon,ttH}(m_X) &= 2523.55 \cdot \frac{1}{m_X^2} - 0.0000079 \cdot m_X + 0.0076, \\ c_{6,\epsilon,ttH}(m_X) &= 0, \\ c_{7,\epsilon,ttH}(m_X) &= 6087.51 \cdot \frac{1}{m_X^2} + 0.00000027 \cdot m_X - 0.0039. \end{aligned} \tag{B.1}$$

This gives the function for $\sigma_{\epsilon,ttH}$ as

$$\sigma_{\epsilon,ttH}(c_t, c_{\tilde{t}}, c_V, m_X) = c_{5,\epsilon,ttH}(m_X) \cdot c_t^4 + c_{7,\epsilon,ttH}(m_X) \cdot \tilde{c}_t^4. \tag{B.2}$$

The fit functions for the total cross section $\sigma_{tot,ttH}$ are given by

$$\begin{aligned} c_{5,\text{tot},ttH}(m_X) &= 2703921.1 \cdot \frac{1}{m_X^2} + 0.0019 \cdot m_X - 3.71, \\ c_{6,\text{tot},ttH}(m_X) &= 0, \\ c_{7,\text{tot},ttH}(m_X) &= 4300877.59 \cdot \frac{1}{m_X^2} + 0.0048 \cdot m_X - 8.14. \end{aligned} \tag{B.3}$$

Which gives the function for $\sigma_{tot,ttH}$

$$\sigma_{\text{tot},ttH}(c_t, c_{\tilde{t}}, c_V, m_X) = c_{5,\text{tot},ttH}(m_X) \cdot c_t^4 + c_{7,\text{tot},ttH}(m_X) \cdot \tilde{c}_t^4. \tag{B.4}$$

In Fig. 34 the coefficients are shown as function of the mass. The dashed orange lines show the fit functions and the blue points show the data points.

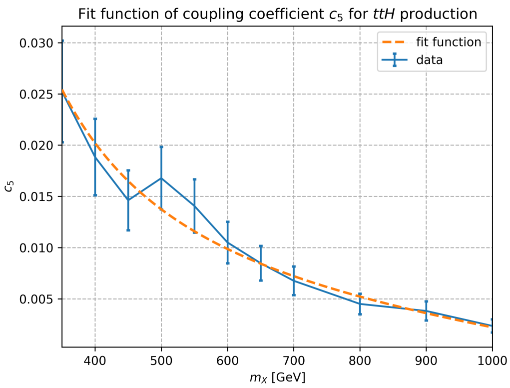

(a)

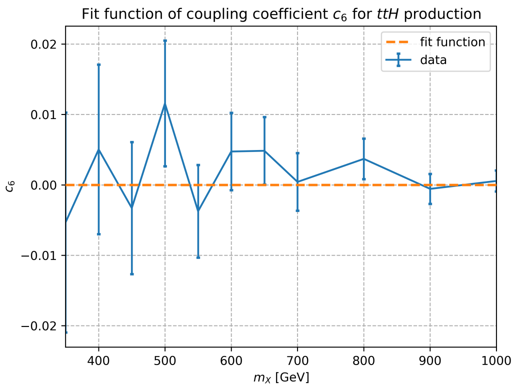

(b)

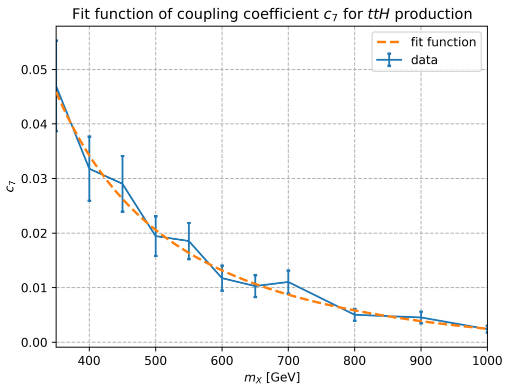

(c)

Figure 34: Coupling coefficients and fit functions for for the ttH production process as a function of the mass.

B.2.2 tWH-production

The fit functions for the coefficients in $\sigma_{\epsilon,tWH}$ are given by

$$\begin{aligned}
c_{1,\epsilon,tWH}(m_X) &= 850 \cdot \frac{1}{m_X^2} - 0.00000042 \cdot m_X - 0.00018, \\
c_{2,\epsilon,tWH}(m_X) &= 0, \\
c_{3,\epsilon,tWH}(m_X) &= -2100 \cdot \frac{1}{m_X^2} + 0.0000016 \cdot m_X - 0.00025, \\
c_{4,\epsilon,tWH}(m_X) &= -0.0000032 \cdot m_X + 0.0036, \\
c_{5,\epsilon,tWH}(m_X) &= 1200 \cdot \frac{1}{m_X^2} - 0.0000026 \cdot m_X + 0.0021, \\
c_{6,\epsilon,tWH}(m_X) &= -1200 \cdot \frac{1}{m_X^2} - 0.0000059 \cdot m_X + 0.0067, \\
c_{7,\epsilon,tWH}(m_X) &= 5500 \cdot \frac{1}{m_X^2} - 0.0000047 \cdot m_X - 0.0049.
\end{aligned} \tag{B.5}$$

This gives the function for $\sigma_{\epsilon,ttH}$ as

$$\begin{aligned}
\sigma_{\epsilon,tWH}(c_t, c_{\tilde{t}}, c_V, m_X) =& c_{1,\epsilon,tWH}(m_X) \cdot c_V^2 ct^2 + c_{3,\epsilon,tWH}(m_X) \cdot c_V c_t^3 + \\
& c_{4,\epsilon,tWH}(m_X) \cdot c_V c_t \tilde{c}_t^2 + c_{5,\epsilon,tWH}(m_X) \cdot c_t^4 + \\
& c_{6,\epsilon,tWH}(m_X) \cdot c_t^2 \tilde{c}_t^2 + c_{7,\epsilon,tWH}(m_X) \cdot \tilde{c}_t^4
\end{aligned} \tag{B.6}$$

The fit functions for the total cross section $\sigma_{tot,tWH}$ are given by

$$\begin{aligned}
c_{1,\text{tot},tWH}(m_X) &= 940000 \cdot \frac{1}{m_X^2} + 0.0011 \cdot m_X - 1.8, \\
c_{2,\text{tot},tWH}(m_X) &= 0, \\
c_{3,\text{tot},tWH}(m_X) &= -2100000 \cdot \frac{1}{m_X^2} - 0.0015 \cdot m_X - 3, \\
c_{4,\text{tot},tWH}(m_X) &= 12000 \cdot \frac{1}{m_X^2} + 0.000055 \cdot m_X - 0.069, \\
c_{5,\text{tot},tWH}(m_X) &= 1300000 \cdot \frac{1}{m_X^2} + 0.000093 \cdot m_X - 0.84, \\
c_{6,\text{tot},tWH}(m_X) &= -8600 \cdot \frac{1}{m_X^2} - 0.000035 \cdot m_X + 0.044, \\
c_{7,\text{tot},tWH}(m_X) &= 1300000 \cdot \frac{1}{m_X^2} - 0.0000043 \cdot m_X - 0.69.
\end{aligned} \tag{B.7}$$

Which gives the function for $\sigma_{tot,tWH}$

$$\begin{aligned}\sigma_{\mathrm{tot},tWH}(c_t, c_{\tilde{t}}, c_V, m_X) =& c_{1,\mathrm{tot},tWH}(m_X) \cdot c_V^2 ct^2 + c_{3,\mathrm{tot},tWH}(m_X) \cdot c_V ct^3 + \\ & c_{4,\mathrm{tot},tWH}(m_X) \cdot c_V ct \tilde{c}_t^2 + c_{5,\mathrm{tot},tWH}(m_X) \cdot c_t^4 + \\ & c_{6,\mathrm{tot},tWH}(m_X) \cdot c_t^2 \tilde{c}_t^2 + c_{7,\mathrm{tot},tWH}(m_X) \cdot \tilde{c}_t^4.\end{aligned} \tag{B.8}$$

In Fig. 35 and Fig. 36 the coefficients are shown as function of the mass. The dashed orange lines show the fit functions and the blue points show the data points.

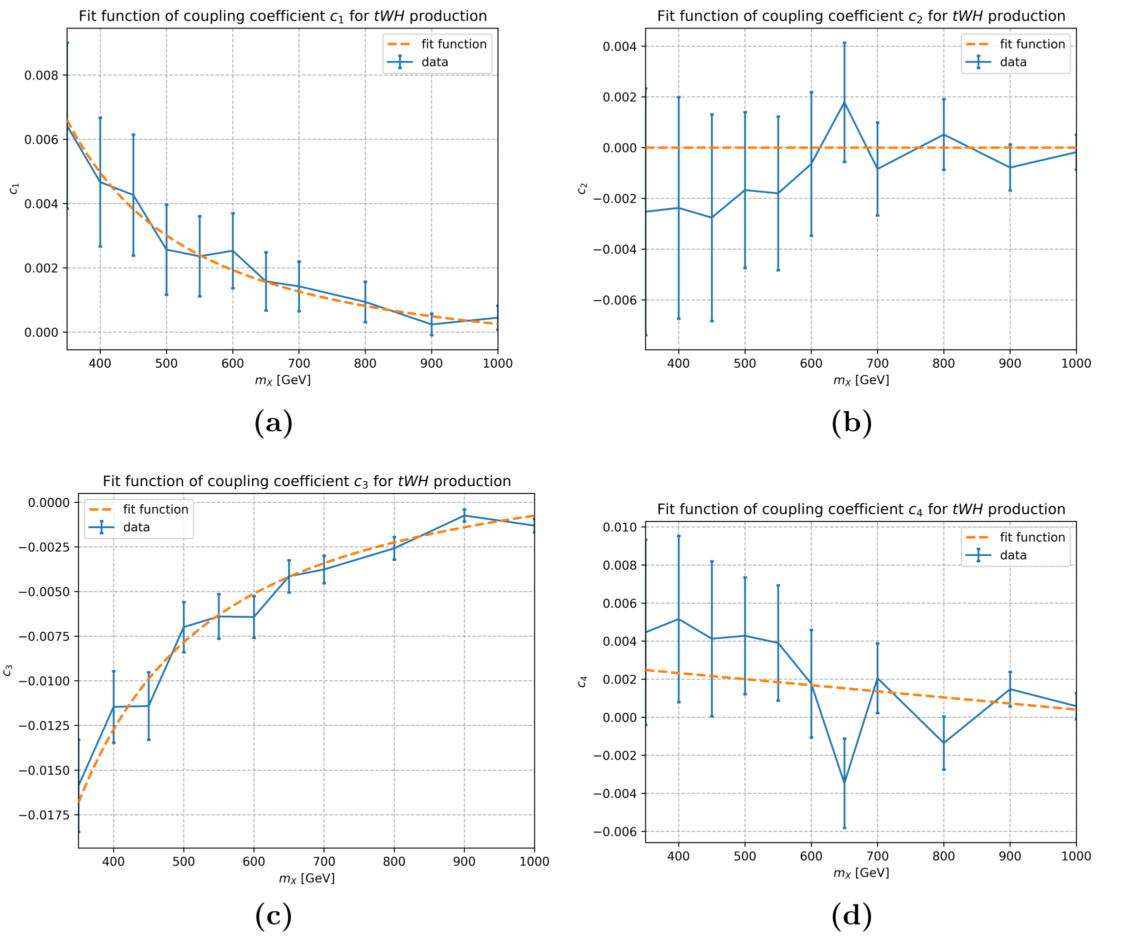

Figure 35: Coupling coefficients and fit functions c_{1-4} for for the tWH production process as a function of the mass.

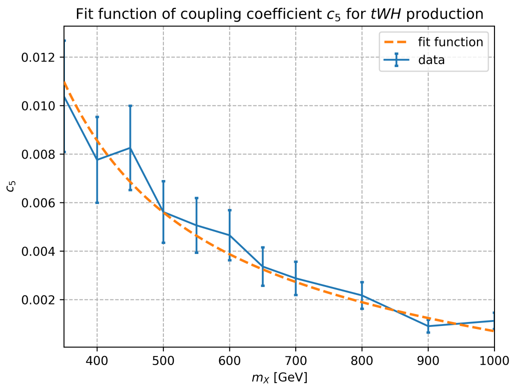

(a)

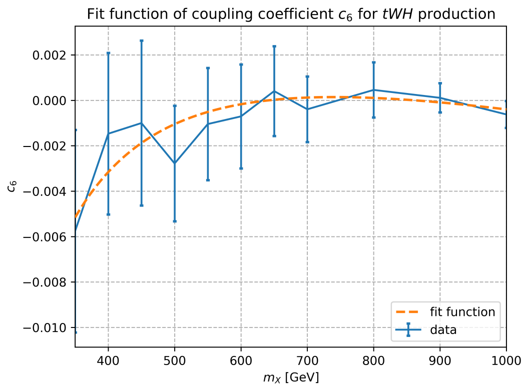

(b)

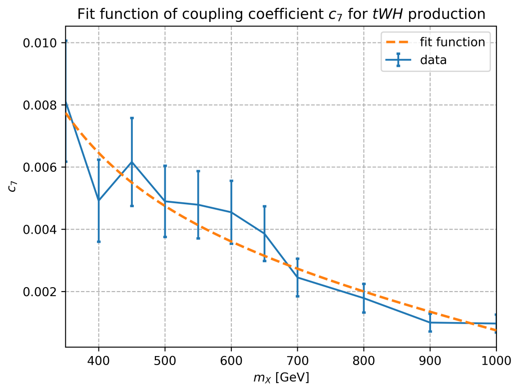

(c)

Figure 36: Coupling coefficients and fit functions c_{5-7} for for the tWH production process as a function of the mass.

B.2.3 tH-production

The fit functions for the coefficients in $\sigma_{\epsilon,tH}$ are given in the form $c_{i,\epsilon,tH}$ by

$$\begin{aligned} c_{5,\epsilon,tH}(m_X) &= 604.51 \cdot \frac{1}{m_X^2} - 0.00000053 \cdot m_X + 0.00032, \\ c_{7,\epsilon,tH}(m_X) &= 150.39 \cdot \frac{1}{m_X^2} + 0.0000017 \cdot m_X - 0.0017. \end{aligned} \tag{B.9}$$

All other coefficents c_i are zero. This gives the function for $\sigma_{\epsilon,ttH}$ as

$$\sigma_{\epsilon,tH}(c_t, c_{\tilde{t}}, m_X) = c_{5,\epsilon,tH}(m_X) \cdot c_t^4 + c_{7,\epsilon,tH}(m_X) \cdot \tilde{c}_t^4. \tag{B.10}$$

The fit functions for the total cross section $\sigma_{tot,ttH}$ are given by

$$\begin{aligned} c_{5,\text{tot},tH}(m_X) &= 2948263.1 \cdot \frac{1}{m_X^2} + 0.0041 \cdot m_X - 6.35, \\ c_{7,\text{tot},tH}(m_X) &= 1741654.4 \cdot \frac{1}{m_X^2} + 0.0014 \cdot m_X - 2.57. \end{aligned} \tag{B.11}$$

Which gives the function for $\sigma_{tot,ttH}$

$$\sigma_{\text{tot},tH}(c_t, c_{\tilde{t}}, m_X) = c_{5,\text{tot},ttH}(m_X) \cdot c_t^4 + c_{7,\text{tot},ttH}(m_X) \cdot \tilde{c}_t^4. \tag{B.12}$$

In Fig. 34 the coefficients are shown as function of the mass. The dashed orange lines show the fit functions and the blue points show the data points.

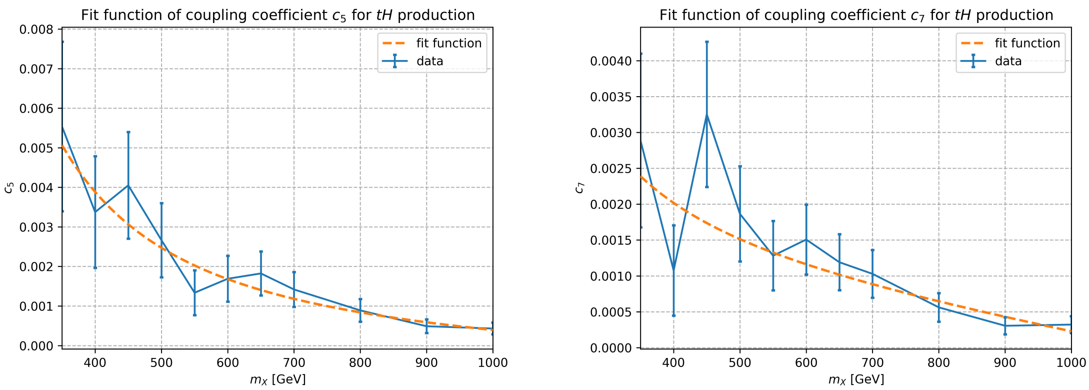

(a) **(b)**

Figure 37: Coupling coefficients and fit functions for for the tH production process as a function of the mass.

B.3 Implementation in HiggsBounds

In this section, we will document the implementation of your analysis in the code HiggsBounds. In HiggsBounds, we are able to implement a limit that is derived from coupling dependent acceptances. The four-top analysis present in Sect. 6 is the first analysis which is implemented in this way. Therefore, we here document the necessary code. For simplicity we will only show an example for the implementation of the ttH process. The limits for tWH and tH production are implement in the same way.

We start by importing some dependencies. These include some well-known Python packages for data handling (e.g. pandas) and HiggsPredictions, as well as Higgsbounds. We also need to import some functions from ImplementationUtils, which is part of the HiggsTools installation.

```
import pandas as pd
import numpy as np
from Higgs.tools.ImplementationUtils import (
    implementChannelLimit,
    implementChannelWidthLimit,
    fromHB5Table1,
    readHEPDataCsv,
)
from Higgs import Predictions
from Higgs import predictions as HP
from Higgs import bounds as HB
from Higgs.tools.LimitValidation import validateChannelLimit,
validateChannelWidthLimit
import os, sys
import matplotlib.pyplot as plt
import pwlf
from scipy.interpolate import interp1d

sys.path.insert(0, os.path.dirname(os.path.dirname(os.getcwd())))
import MassResolutions as resolution
```

We can calculate the upper limit on the signal events n_s with MadAnalysis. For this we need the observed and expected number of events in our most sensitive signal region. We then implement the expected and observed limit on n_s in our mass range of $[350, 1000]$ GeV. We also have to define the fit functions for the individual coefficients of the total cross-section σ_{tot} and cross-section times efficiency $\sigma \cdot \epsilon$. The number of signal events is defined as

$$n_s = \epsilon_s \cdot \mathcal{L} \cdot \sigma. \tag{B.13}$$

For Signal Region 8 of the CMS analysis the upper limit on the expected and observed number of signal are given by $n_{s,exp} = 6.94$ and $n_{s,obs} = 6.43$. We use this to implement the observed and expected limit on

$$\sigma \cdot \epsilon = \frac{n_s}{\mathcal{L}}. \tag{B.14}$$

One also has to specifically define the production mode as `["Htt"]` in `Higgsbounds`.

```
df = pd.DataFrame(
    columns={
        "m",
        "obs",
        "exp",
    }
)

# fit functions for efficiency eff = sigma_s/sigma_tot

xtot_c5 = lambda m: 2703921.1 * 1/m**2 + 0.0019 * m - 3.71
xtot_c7 = lambda m: 4300877.59 * 1/m**2 + 0.0048 * m - 8.14

xeff_c5 = lambda m: 2523.55 * 1/m**2 + -0.0000079 * m + 0.0076
xeff_c7 = lambda m: 6087.51 * 1/m**2 + 0.00000027 * m - 0.0039

prods = ["Htt"]
```

```
masses = np.linspace(350, 1000, 100)

df.m = masses
df.obs = [6.43/(1000*137)] * len(masses)
df["exp"] = [6.94/(1000*137)] * len(masses)
```

Now we can start with the actual limit implementation of the coupling dependent acceptances. For this, we define the dependence of the acceptances on the individual couplings by our fit functions for the coefficients of $\sigma \cdot \epsilon$. This is done in the code block `acceptances=[...]`. Here we assign the fit functions to the individual couplings defined by `effCPeTopYuk` for the $\mathcal{CP}$-even and `effCPoTopYuk` for the $\mathcal{CP}$-odd top-Yukawa coupling. The number (in our case four) depicts to which power the coupling contributes.

```
df1 = pd.DataFrame(
    columns={
        "m",
        "AccCPe",
        "AccCPo"
    }
)

df1.m = masses
df1.AccCPe = xeff_c5(df1.m)
df1.AccCPo = xeff_c7(df1.m)

limitFile = implementChannelLimit(
    "1908.06463",
    {"channels": [[p, "tt"] for p in prods]},
    "https://arxiv.org/pdf/1908.06463.pdf",
    df,
    massResolution=resolution.tt["tttt"],
    acceptances=[
        {
            "couplingDepAcceptance": [
```

```
            [
                {"effCPeTopYuk": 4},
                {
                    "massDepAcceptance": df1.AccCPe.to_list(),
                    "massGrid": df1.m.to_list()
                }
            ],
           [
               {"effCPoTopYuk": 4},
               {
                   "massDepAcceptance": df1.AccCPo.to_list(),
                   "massGrid": df1.m.to_list()
               }
           ]
        ],
        "denominator": [
            [
                {"effCPeTopYuk": 4},
                {
                    "massDepAcceptance": df1.AccCPetot.to_list(),
                    "massGrid": df1.m.to_list()
                }
            ],
           [
               {"effCPoTopYuk": 4},
               {
                   "massDepAcceptance": df1.AccCPotot.to_list(),
                   "massGrid": df1.m.to_list()
               }
           ]
        ]
        }
        for p in prods
    ],
)
```

```
lim = HB.Limit(limitFile)

validateChannelLimit(
    lim
)
```

Running this code will give a variety of validation plots. In our case, this validation plot is just given by the constant upper limit on the n_S as shown in figure Fig. 38(left). This is not very useful to judge the success of an analysis. One can also validate the cross-section limit, which is shown in Fig. 38(right). This is what is usually done by `HiggsBounds` when implementing a new limit.

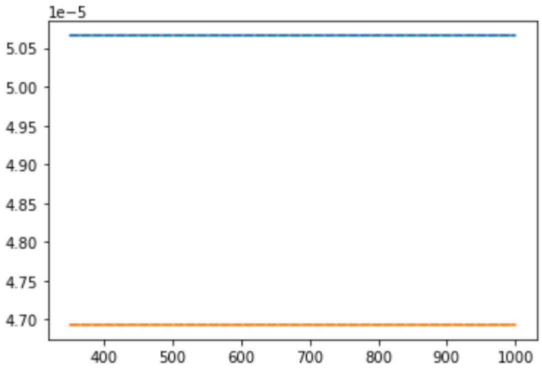

(a)

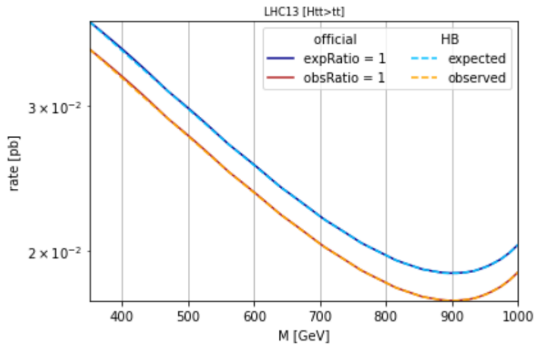

(b)

Figure 38: Validation plots generated with `HiggsBounds`. The left plot shows the number of signal events n_s as a function of the mass. The right plot shows the expected and observed upper limit on the cross-section times branching ratio for ttH production as a function of the mass. These plots are automatically generated when implementing a new limit in `Higgsbounds`.

References

[1] Margarete Mühlleitner, Marco O. P. Sampaio, Rui Santos, and Jonas Wittbrodt. The n2hdm under theoretical and experimental scrutiny. Journal of High Energy Physics, 2017(3), mar 2017.

[2] Sebastian Baum and Nausheen R. Shah. Two higgs doublets and a complex singlet: disentangling the decay topologies and associated phenomenology. Journal of High Energy Physics, 2018(12), dec 2018.

[3] Ulrich Ellwanger, Cyril Hugonie, and Ana M. Teixeira. The next-to-minimal supersymmetric standard model. Physics Reports, 496(1-2):1–77, nov 2010.

[4] Albert M Sirunyan et al. Search for a standard model-like Higgs boson in the mass range between 70 and 110 GeV in the diphoton final state in proton-proton collisions at $\sqrt{s} = 8$ and 13 TeV. Phys. Lett. B, 793:320–347, 2019.

[5] R. Barate et al. Search for the standard model Higgs boson at LEP. Phys. Lett. B, 565:61–75, 2003.

[6] S. Heinemeyer, C. Li, F. Lika, G. Moortgat-Pick, and S. Paasch. A 96 gev higgs boson in the 2hdm plus singlet, 2021.

[7] A. Tumasyan A. M. Sirunyan et al. Search for production of four top quarks in final states with same-sign or multiple leptons in proton-proton collisions at $\sqrt{s} = 13$ tev. The European Physical Journal C, 80(2), jan 2020.

[8] Duarte Fontes, Margarete Mühlleitner, Jorge C. Romão, Rui Santos, João P. Silva, and Jonas Wittbrodt. The c2hdm revisited. Journal of High Energy Physics, 2018(2), feb 2018.

[9] Abdus Salam. Weak and Electromagnetic Interactions. Conf. Proc. C, 680519:367–377, 1968.

[10] Sheldon L. Glashow. The renormalizability of vector meson interactions. Nuclear Physics, 10:107–117, 1959.

[11] Sheldon L. Glashow. Partial-symmetries of weak interactions. Nuclear Physics, 22(4):579–588, 1961.

[12] Steven Weinberg. A Model of Leptons. Phys. Rev. Lett., 19:1264–1266, 1967.

[13] S. L. Glashow, J. Iliopoulos, and L. Maiani. Weak Interactions with Lepton-Hadron Symmetry. Phys. Rev. D, 2:1285–1292, 1970.

[14] Yuval Ne'eman. Derivation of strong interactions from a gauge invariance. Nucl. Phys., 26:222–229, 1961.

[15] Murray Gell-Mann. Symmetries of baryons and mesons. Phys. Rev., 125:1067–1084, Feb 1962.

[16] Murray Gell-Mann. A Schematic Model of Baryons and Mesons. Phys. Lett., 8:214–215, 1964.

[17] G. Zweig. An SU(3) model for strong interaction symmetry and its breaking. Version 2, pages 22–101. 2 1964.

[18] H. Fritzsch, M. Gell-Mann, and H. Leutwyler. Advantages of the color octet gluon picture. Physics Letters B, 47(4):365–368, 1973.

[19] Michael Edward Peskin and Daniel V. Schroeder. An Introduction to Quantum Field Theory. Westview Press, 1995. Reading, USA: Addison-Wesley (1995) 842 p.

[20] Heather E. Logan. Tasi 2013 lectures on higgs physics within and beyond the standard model, 2014.

[21] R. L. Workman and Others. Review of Particle Physics. PTEP, 2022:083C01, 2022.

[22] Particle Data Group. Review of particle physics. Phys. Rev. D, 98:030001, Aug 2018.

[23] Constraining the Higgs boson self-coupling from single- and double-Higgs production with the ATLAS detector using pp collisions at $\sqrt{s} = 13$ TeV. 2022.

[24] F. Zwicky. Die Rotverschiebung von extragalaktischen Nebeln. Helvetica Physica Acta, 6:110–127, 1933.

[25] F. Zwicky. On the Masses of Nebulae and of Clusters of Nebulae. Astrophys. J., 86:217, 1937.

[26] Vera C. Rubin and Jr. Ford, W. Kent. Rotation of the Andromeda Nebula from a Spectroscopic Survey of Emission Regions. Astrophys. J., 159:379, February 1970.

[27] V. C. Rubin, Jr. Ford, W. K., and N. Thonnard. Rotational properties of 21 SC galaxies with a large range of luminosities and radii, from NGC 4605 (R=4kpc) to UGC 2885 (R=122kpc). Astrophys. J., 238:471–487, June 1980.

[28] Alexandre Refregier. Weak gravitational lensing by large-scale structure. Annual Review of Astronomy and Astrophysics, 41(1):645–668, sep 2003.

[29] J. Anthony Tyson, Greg P. Kochanski, and Ian P. Dell'Antonio. Detailed mass map of cl0024+1654 from strong lensing. The Astrophysical Journal, 498(2):L107–L110, may 1998.

[30] E. Komatsu, K. M. Smith, J. Dunkley, C. L. Bennett, B. Gold, G. Hinshaw, N. Jarosik, D. Larson, M. R. Nolta, L. Page, D. N. Spergel, M. Halpern, R. S. Hill, A. Kogut, M. Limon, S. S. Meyer, N. Odegard, G. S. Tucker, J. L. Weiland, E. Wollack, and E. L. Wright. Seven-year wilkinson microwave anisotropy probe (wmap) observations: Cosmological interpretation. The Astrophysical Journal Supplement Series, 192(2):18, jan 2011.

[31] E. Aprile et al. Dark matter search results from a one ton-year exposure of XENON1t. Physical Review Letters, 121(11), sep 2018.

[32] N. Aghanim et al. Planck 2018 results. vi. cosmological parameters. Astronomy & Astrophysics, 641:A6, sep 2020.

[33] M. Fukugita and T. Yanagida. Barygenesis without grand unification. Physics Letters B, 174(1):45–47, 1986.

[34] W. Buchmüller, P. Di Bari, and M. Plümacher. Leptogenesis for pedestrians. Annals of Physics, 315(2):305–351, feb 2005.

[35] P. Basler, M. Krause, M. Mühlleitner, J. Wittbrodt, and A. Wlotzka. Strong first order electroweak phase transition in the CP-conserving 2hdm revisited. Journal of High Energy Physics, 2017(2), feb 2017.

[36] Lars Fromme and Stephan J Huber. Top transport in electroweak baryogenesis. Journal of High Energy Physics, 2007(03):049–049, mar 2007.

[37] T Konstandin. Quantum transport and electroweak baryogenesis. Physics-Uspekhi, 56(8):747–771, aug 2013.

[38] G.C. Branco, P.M. Ferreira, L. Lavoura, M.N. Rebelo, Marc Sher, and João P. Silva. Theory and phenomenology of two-higgs-doublet models. Physics Reports, 516(1-2):1–102, jul 2012.

[39] Andrzej J. Buras, Maria Valentina Carlucci, Stefania Gori, and Gino Isidori. Higgs-mediated FCNCs: natural flavour conservation vs. minimal flavour violation. Journal of High Energy Physics, 2010(10), oct 2010.

[40] CSABA CSÁKI. THE MINIMAL SUPERSYMMETRIC STANDARD MODEL. Modern Physics Letters A, 11(08):599–613, mar 1996.

[41] T. Biekötter, M. Chakraborti, and S. Heinemeyer. A 96 GeV Higgs boson in the N2HDM. Eur. Phys. J. C, 80(1):2, 2020.

[42] Thomas Biekötter, M. Chakraborti, and Sven Heinemeyer. An N2HDM Solution for the possible 96 GeV Excess. PoS, CORFU2018:015, 2019.

[43] T. Biekötter, M. Chakraborti, and S. Heinemeyer. The "96 GeV excess" in the N2HDM. In 31st Rencontres de Blois on Particle Physics and Cosmology, 10 2019.

[44] T. Biekötter, M. Chakraborti, and S. Heinemeyer. The "96 GeV excess" at the ILC. In International Workshop on Future Linear Colliders, 2 2020.

[45] T. Biekötter, M. Chakraborti, and S. Heinemeyer. The "96 GeV excess" at the LHC. Int. J. Mod. Phys. A, 36(22):2142018, 2021.

[46] Margarete Muhlleitner, Marco O. P. Sampaio, Rui Santos, and Jonas Wittbrodt. The N2HDM under Theoretical and Experimental Scrutiny. JHEP, 03:094, 2017.

[47] Tilman Plehn. Lectures on LHC Physics. Springer Berlin Heidelberg, 2012.

[48] J. Horejsi and M. Kladiva. Tree-unitarity bounds for THDM Higgs masses revisited. Eur. Phys. J. C, 46:81–91, 2006.

[49] Margarete Mühlleitner, Marco O. P. Sampaio, Rui Santos, and Jonas Wittbrodt. ScannerS: parameter scans in extended scalar sectors. Eur. Phys. J. C, 82(3):198, 2022.

[50] K. G. Klimenko. On Necessary and Sufficient Conditions for Some Higgs Potentials to Be Bounded From Below. Theor. Math. Phys., 62:58–65, 1985.

[51] Wolfgang G. Hollik, Georg Weiglein, and Jonas Wittbrodt. Impact of vacuum stability constraints on the phenomenology of supersymmetric models. Journal of High Energy Physics, 2019(3), mar 2019.

[52] Sidney Coleman. Fate of the false vacuum: Semiclassical theory. Phys. Rev. D, 15:2929–2936, May 1977.

[53] Curtis G. Callan and Sidney Coleman. Fate of the false vacuum. ii. first quantum corrections. Phys. Rev. D, 16:1762–1768, Sep 1977.

[54] P. M. Ferreira, Rui Santos, Margarete Mühlleitner, Georg Weiglein, and Jonas Wittbrodt. Vacuum instabilities in the n2hdm. Journal of High Energy Physics, 2019(9), Sep 2019.

[55] Wolfgang G. Hollik, Georg Weiglein, and Jonas Wittbrodt. Impact of vacuum stability constraints on the phenomenology of supersymmetric models. Journal of High Energy Physics, 2019(3), Mar 2019.

[56] J. Wittbrodt. `https://gitlab.com/jonaswittbrodt/EVADE`.

[57] Tsung-Lin Lee, Tien-Yien Li, and Chih-Hsiung Tsai. Hom4ps-2.0: a software package for solving polynomial systems by the polyhedral homotopy continuation method. Computing, 83(2):109–133, 2008.

[58] Victor Guada, Miha Nemevšek, and Matevž Pintar. Findbounce: Package for multi-field bounce actions. Computer Physics Communications, 256:107480, Nov 2020.

[59] J. E. Camargo-Molina, B. O'Leary, W. Porod, and F. Staub. Vevacious: a tool for finding the global minima of one-loop effective potentials with many scalars. The European Physical Journal C, 73(10), Oct 2013.

[60] Carroll L. Wainwright. CosmoTransitions: Computing cosmological phase transition temperatures and bubble profiles with multiple fields. Computer Physics Communications, 183(9):2006–2013, sep 2012.

[61] Philip Bechtle, Sven Heinemeyer, Oscar Stål, Tim Stefaniak, and Georg Weiglein. *HiggsSignals*: Confronting arbitrary Higgs sectors with measurements at the Tevatron and the LHC. Eur. Phys. J. C, 74(2):2711, 2014.

[62] Philip Bechtle, Sven Heinemeyer, Oscar Stål, Tim Stefaniak, and Georg Weiglein. Probing the Standard Model with Higgs signal rates from the Tevatron, the LHC and a future ILC. JHEP, 11:039, 2014.

[63] Philip Bechtle, Oliver Brein, Sven Heinemeyer, Georg Weiglein, and Karina E. Williams. HiggsBounds: Confronting Arbitrary Higgs Sectors with Exclusion Bounds from LEP and the Tevatron. Comput. Phys. Commun., 181:138–167, 2010.

[64] Philip Bechtle, Oliver Brein, Sven Heinemeyer, Georg Weiglein, and Karina E. Williams. HiggsBounds 2.0.0: Confronting Neutral and Charged Higgs Sector Predictions with Exclusion Bounds from LEP and the Tevatron. Comput. Phys. Commun., 182:2605–2631, 2011.

[65] Philip Bechtle, Oliver Brein, Sven Heinemeyer, Oscar Stål, Tim Stefaniak, Georg Weiglein, and Karina E. Williams. HiggsBounds $-$ 4: Improved Tests of Extended Higgs Sectors against Exclusion Bounds from LEP, the Tevatron and the LHC. Eur. Phys. J. C, 74(3):2693, 2014.

[66] Philip Bechtle, Sven Heinemeyer, Oscar Stal, Tim Stefaniak, and Georg Weiglein. Applying Exclusion Likelihoods from LHC Searches to Extended Higgs Sectors. Eur. Phys. J. C, 75(9):421, 2015.

[67] Henning Bahl, Thomas Biekötter, Sven Heinemeyer, Cheng Li, Steven Paasch, Georg Weiglein, and Jonas Wittbrodt. Higgstools: Bsm scalar phenomenology with new versions of higgsbounds and higgssignals, 2022.

[68] ATLAS and CMS collaboration. Combined measurement of the higgs boson mass in pp collisions at $\sqrt{s} = 7$ and 8 tev with the atlas and cms experiments. Physical Review Letters, 114(19), may 2015.

[69] ATLAS and CMS collaboration. Measurements of the higgs boson production and decay rates and constraints on its couplings from a combined atlas and cms analysis of the lhc pp collision data at $\sqrt{s} = 7$ and 8 tev. Journal of High Energy Physics, 2016(8), aug 2016.

[70] CERN. Cern yellow reports: Monographs, vol 2 (2017): Handbook of lhc higgs cross sections: 4. deciphering the nature of the higgs sector, 2017.

[71] CMS collaboration. Analysis of the cp structure of the yukawa coupling between the higgs boson and τ leptons in proton-proton collisions at $\sqrt{s} = 13$ tev. Journal of High Energy Physics, 2022(6), jun 2022.

[72] M. Aaboud, G. Aad, B. Abbott, O. Abdinov, B. Abeloos, D. K. Abhayasinghe, S. H. Abidi, O. S. AbouZeid, N. L. Abraham, and et al. Search for charged higgs bosons decaying into top and bottom quarks at $\sqrt{s} = 13$ tev with the atlas detector. Journal of High Energy Physics, 2018(11), Nov 2018.

[73] ATLAS collaboration. Search for scalar resonances decaying into $\mu^+ + \mu^-$- in events with and without b-tagged jets produced in proton-proton collisions at $\sqrt{s} = 13$ tev with the atlas detector. Journal of High Energy Physics, 2019(7), jul 2019.

[74] Mikołaj Misiak and Matthias Steinhauser. Weak radiative decays of the b meson and bounds on $m_{H^\pm}$ in the two-higgs-doublet model. The European Physical Journal C, 77(3), mar 2017.

[75] A. Arbey, F. Mahmoudi, O. Stal, and T. Stefaniak. Status of the Charged Higgs Boson in Two Higgs Doublet Models. Eur. Phys. J. C, 78(3):182, 2018.

[76] M. Ciuchini, G. Degrassi, P. Gambino, and G.F. Giudice. Next-to-leading qcd corrections to b $\rightarrow$ xsγ: Standard model and two-higgs doublet model. Nuclear Physics B, 527(1-2):21–43, Aug 1998.

[77] Thomas Hermann, Mikolaj Misiak, and Matthias Steinhauser. $\overline{B} \rightarrow X_s\gamma$ in the two higgs doublet model up to next-to-next-to-leading order in qcd. Journal of High Energy Physics, 2012(11), Nov 2012.

[78] M. Misiak, H. Asatrian, R. Boughezal, M. Czakon, T. Ewerth, A. Ferroglia, P. Fiedler, P. Gambino, C. Greub, U. Haisch, and et al. Updated next-to-next-to-leading-order qcd predictions for the weak radiative b -meson decays. Physical Review Letters, 114(22), Jun 2015.

[79] Qin Chang, Pei-Fu Li, and Xin-Qiang Li. $B_s^0 - \bar{B}_s^0$ mixing within minimal flavor-violating two-higgs-doublet models. The European Physical Journal C, 75(12), Dec 2015.

[80] T. Barakat. The rare decay $k \to \pi\nu\nu$ in two higgs doublet modelin two higgs doublet model. Il Nuovo Cimento A, 112(7):697–704, Jul 1999.

[81] Michael E. Peskin and Tatsu Takeuchi. Estimation of oblique electroweak corrections. Phys. Rev. D, 46:381–409, Jul 1992.

[82] J. Haller, A. Hoecker, R. Kogler, K. Mönig, T. Peiffer, and J. Stelzer. Update of the global electroweak fit and constraints on two-Higgs-doublet models. The European physical journal / C, 78(8):675, 2018.

[83] W Grimus, L Lavoura, O M Ogreid, and P Osland. A precision constraint on multi-higgs-doublet models. Journal of Physics G: Nuclear and Particle Physics, 35(7):075001, may 2008.

[84] W. Grimus, L. Lavoura, O.M. Ogreid, and P. Osland. The oblique parameters in multi-higgs-doublet models. Nuclear Physics B, 801(1-2):81–96, sep 2008.

[85] W. Grimus, L. Lavoura, O. M. Ogreid, and P. Osland. The Oblique parameters in multi-Higgs-doublet models. Nucl. Phys. B, 801:81–96, 2008.

[86] Search for new resonances in the diphoton final state in the mass range between 80 and 110 GeV in pp collisions at $\sqrt{s} = 8$ TeV. Technical report, CERN, Geneva, 2015.

[87] G. Abbiendi et al. Decay mode independent searches for new scalar bosons with the OPAL detector at LEP. Eur. Phys. J. C, 27:311–329, 2003.

[88] S. Schael et al. Search for neutral MSSM Higgs bosons at LEP. Eur. Phys. J. C, 47:547–587, 2006.

[89] Updated Combination of CDF and D0 Searches for Standard Model Higgs Boson Production with up to 10.0 fb^{-1} of Data. 7 2012.

[90] Search for new resonances in the diphoton final state in the mass range between 70 and 110 GeV in pp collisions at $\sqrt{s} = 8$ and 13 TeV. 2017.

[91] Albert M Sirunyan et al. Search for additional neutral MSSM Higgs bosons in the $\tau\tau$ final state in proton-proton collisions at $\sqrt{s} = 13$ TeV. JHEP, 09:007, 2018.

[92] Search for resonances in the 65 to 110 GeV diphoton invariant mass range using 80 fb^{-1} of pp collisions collected at $\sqrt{s} = 13$

TeV with the ATLAS detector. Technical report, CERN, Geneva, Jul 2018. All figures including auxiliary figures are available at https://atlas.web.cern.ch/Atlas/GROUPS/PHYSICS/CONFNOTES/ATLAS-CONF-2018-025.

[93] Sven Heinemeyer and T. Stefaniak. A Higgs Boson at 96 GeV?! PoS, CHARGED2018:016, 2019.

[94] Thomas Biekötter, Alexander Grohsjean, Sven Heinemeyer, Christian Schwanenberger, and Georg Weiglein. Possible indications for new Higgs bosons in the reach of the LHC: N2HDM and NMSSM interpretations. Eur. Phys. J. C, 82(2):178, 2022.

[95] Florian Domingo, Sven Heinemeyer, Sebastian Paßehr, and Georg Weiglein. Decays of the neutral Higgs bosons into SM fermions and gauge bosons in the $\mathcal{CP}$-violating NMSSM. Eur. Phys. J. C, 78(11):942, 2018.

[96] Kiwoon Choi, Sang Hui Im, Kwang Sik Jeong, and Chan Beom Park. Light Higgs bosons in the general NMSSM. Eur. Phys. J. C, 79(11):956, 2019.

[97] T. Biekötter, S. Heinemeyer, and C. Muñoz. Precise prediction for the Higgs-boson masses in the $\mu\nu$ SSM. Eur. Phys. J. C, 78(6):504, 2018.

[98] T. Biekötter, S. Heinemeyer, and C. Muñoz. Precise prediction for the Higgs-Boson masses in the $\mu\nu$ SSM with three right-handed neutrino superfields. Eur. Phys. J. C, 79(8):667, 2019.

[99] Wolfgang Gregor Hollik, Stefan Liebler, Gudrid Moortgat-Pick, Sebastian Paßehr, and Georg Weiglein. Phenomenology of the inflation-inspired NMSSM at the electroweak scale. Eur. Phys. J. C, 79(1):75, 2019.

[100] Junjie Cao, Xinglong Jia, Yuanfang Yue, Haijing Zhou, and Pengxuan Zhu. 96 GeV diphoton excess in seesaw extensions of the natural NMSSM. Phys. Rev. D, 101(5):055008, 2020.

[101] Patrick J. Fox and Neal Weiner. Light Signals from a Lighter Higgs. JHEP, 08:025, 2018.

[102] Ulrich Haisch and Augustinas Malinauskas. Let there be light from a second light Higgs doublet. JHEP, 03:135, 2018.

[103] Francois Richard. Search for a light radion at HL-LHC and ILC250. 12 2017.

[104] Da Liu, Jia Liu, Carlos E. M. Wagner, and Xiao-Ping Wang. A Light Higgs at the LHC and the B-Anomalies. JHEP, 06:150, 2018.

[105] Lijia Liu, Haoxue Qiao, Kun Wang, and Jingya Zhu. A Light Scalar in the Minimal Dilaton Model in Light of LHC Constraints. Chin. Phys. C, 43(2):023104, 2019.

[106] François Richard. Indications for extra scalars at LHC? – BSM physics at future e^+e^- colliders. 1 2020.

[107] James M. Cline and Takashi Toma. Pseudo-Goldstone dark matter confronts cosmic ray and collider anomalies. Phys. Rev. D, 100(3):035023, 2019.

[108] Juan Antonio Aguilar-Saavedra and Filipe Rafael Joaquim. Multiphoton signals of a (96 GeV?) stealth boson. Eur. Phys. J. C, 80(5):403, 2020.

[109] Junjie Cao, Xiaofei Guo, Yangle He, Peiwen Wu, and Yang Zhang. Diphoton signal of the light Higgs boson in natural NMSSM. Phys. Rev. D, 95(11):116001, 2017.

[110] S. Gascon-Shotkin. Update on Higgs searches below 125 GeV. Higgs Days at Sandander, 2017. `https://indico.cern.ch/event/666384/contributions/2723427/`.

[111] Werner Porod. SPheno, a program for calculating supersymmetric spectra, SUSY particle decays and SUSY particle production at e+ e- colliders. Comput. Phys. Commun., 153:275–315, 2003.

[112] W. Porod and F. Staub. SPheno 3.1: Extensions including flavour, CP-phases and models beyond the MSSM. Comput. Phys. Commun., 183:2458–2469, 2012.

[113] Florian Staub. SARAH 4 : A tool for (not only SUSY) model builders. Comput. Phys. Commun., 185:1773–1790, 2014.

[114] Emanuele Bagnaschi et al. MSSM Higgs Boson Searches at the LHC: Benchmark Scenarios for Run 2 and Beyond. Eur. Phys. J. C, 79(7):617, 2019.

[115] P. Drechsel, G. Moortgat-Pick, and G. Weiglein. Prospects for direct searches for light Higgs bosons at the ILC with 250 GeV. Eur. Phys. J. C, 80(10):922, 2020.

[116] Yan Wang, Jenny List, and Mikael Berggren. Search for Light Scalars Produced in Association with Muon Pairs for $\sqrt{s} = 250$ GeV at the ILC. In International Workshop on Future Linear Collider, 1 2018.

[117] Yan Wang, Mikael Berggren, and Jenny List. ILD Benchmark: Search for Extra Scalars Produced in Association with a Z boson at $\sqrt{s} = 500$ GeV. 5 2020.

[118] G. Abbiendi et al. Decay mode independent searches for new scalar bosons with the OPAL detector at LEP. Eur. Phys. J. C, 27:311–329, 2003.

[119] Combined measurements of higgs boson production and decay using up to 80 fb^{-1} of proton–proton collision data at $\sqrt{s} = 13$ tev collected with the atlas experiment. Technical report, CERN, Geneva, Jul 2018.

[120] Albert M Sirunyan et al. Combined measurements of Higgs boson couplings in proton–proton collisions at $\sqrt{s} = 13\,\mathrm{TeV}$. Eur. Phys. J. C, 79(5):421, 2019.

[121] M. Cepeda et al. Report from Working Group 2: Higgs Physics at the HL-LHC and HE-LHC. CERN Yellow Rep. Monogr., 7:221–584, 2019.

[122] Philip Bambade et al. The International Linear Collider: A Global Project. 3 2019.

[123] G. C. Dorsch, S. J. Huber, and J. M. No. A strong electroweak phase transition in the 2hdm after LHC8. Journal of High Energy Physics, 2013(10), oct 2013.

[124] Nathaniel Craig, Jan Hajer, Ying-Ying Li, Tao Liu, and Hao Zhang. Heavy higgs bosons at low tanβ: from the lhc to 100 tev. Journal of High Energy Physics, 2017(1), jan 2017.

[125] P. Artoisenet, P. de Aquino, F. Demartin, R. Frederix, S. Frixione, F. Maltoni, M. K. Mandal, P. Mathews, K. Mawatari, V. Ravindran, S. Seth, P. Torrielli, and M. Zaro. A framework for higgs characterisation. Journal of High Energy Physics, 2013(11), nov 2013.

[126] Henning Bahl, Philip Bechtle, Sven Heinemeyer, Judith Katzy, Tobias Klingl, Krisztian Peters, Matthias Saimpert, Tim Stefaniak, and Georg Weiglein. Indirect $$ \mathcal{CP} $$ probes of the higgs-top-quark interaction: current LHC constraints and future opportunities. Journal of High Energy Physics, 2020(11), nov 2020.

[127] Luc Darmé, Benjamin Fuks, and Fabio Maltoni. Top-philic heavy resonances in four-top final states and their EFT interpretation. Journal of High Energy Physics, 2021(9), sep 2021.

[128] Alan S. Cornell, Wesley Doorsamy, Benjamin Fuks, Gerhard Harmsen, and Lara Mason. Boosted decision trees in the era of new physics: a smuon analysis case study. Journal of High Energy Physics, 2022(4), apr 2022.

[129] A. M. Sirunyan et al. Search for heavy higgs bosons decaying to a top quark pair in proton-proton collisions at $\sqrt{s} = 13$ tev. Journal of High Energy Physics, 2020(4), apr 2020.

[130] CMS Collaboration. Searches for additional higgs bosons and for vector leptoquarks in $\tau\tau$ final states in proton-proton collisions at $\sqrt{s} = 13$ tev, 2022.

[131] Search for a standard model-like Higgs boson in the mass range between 70 and 110 GeV in the diphoton final state in proton-proton collisions at $\sqrt{s} = 13$ TeV. 2023.

[132] D. de Florian et al. Handbook of LHC Higgs Cross Sections: 4. Deciphering the Nature of the Higgs Sector. 2/2017, 10 2016.

[133] Tim Barklow, Keisuke Fujii, Sunghoon Jung, Robert Karl, Jenny List, Tomohisa Ogawa, Michael E. Peskin, and Junping Tian. Improved Formalism for Precision Higgs Coupling Fits. Phys. Rev. D, 97(5):053003, 2018.

[134] Sally Dawson et al. Higgs Working Group Report of the Snowmass 2013 Community Planning Study. Oct 2013. Preliminary entry.

[135] S. Heinemeyer and C. Schappacher. Neutral Higgs boson production at e^+e^- colliders in the complex MSSM: a full one-loop analysis. Eur. Phys. J. C, 76(4):220, 2016.

Eidesstattliche Versicherung

Hiermit versichere ich an Eides statt, die vorliegende Dissertationsschrift selbst verfasst und keine anderen als die angegebenen Hilfsmittel und Quellen benutzt zu haben. Die eingereichte schriftliche Fassung entspricht der auf dem elektronischen Speichermedium. Die Dissertation wurde in der vorgelegten oder einer ähnlichen Form nicht schon einmal in einem früheren Promotionsverfahren angenommen oder als ungenügend beurteilt.

Hamburg, den 12.5.2023 Unterschrift: